Master of Science Thesis

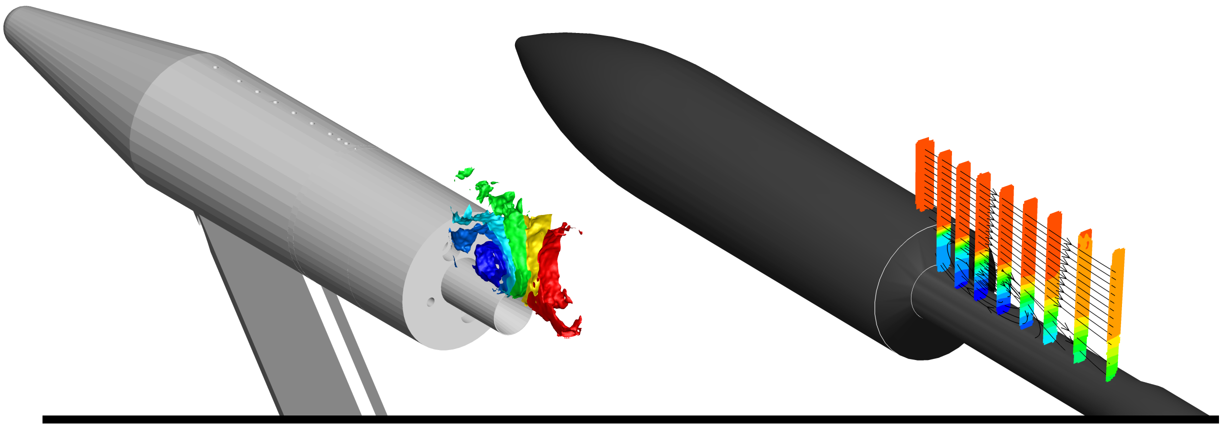

The Effects of Nozzle Length and Exhaust Plume Interaction on High-Speed Base Flows

An experimental investigation using Tomographic PIV

S.G. Brust

March 8, 2017

Faculty of Aerospace Engineering

Delft University of Technology

The Effects of Nozzle Length and Exhaust Plume Interaction on High-Speed Base Flows

An experimental investigation using Tomographic PIV

Master of Science Thesis

For obtaining the degree of Master of Science in Aerospace Engineering
at Delft University of Technology

S.G. Brust

March 8, 2017

Faculty of Aerospace Engineering · Delft University of Technology

Delft University of Technology

Copyright © Aerospace Engineering, Delft University of Technology
All rights reserved.

DELFT UNIVERSITY OF TECHNOLOGY
DEPARTMENT OF AERODYNAMICS

The undersigned hereby certify that they have read and recommend to the Faculty of Aerospace Engineering for acceptance the thesis entitled **"The Effects of Nozzle Length and Exhaust Plume Interaction on High-Speed Base Flows"** by **S.G. Brust** in fulfillment of the requirements for the degree of **Master of Science**.

Dated: March 8, 2017

Supervisors:

Dr. ir. B.W. van Oudheusden

Dr. ir. F.F.J. Schrijer

Ir. P.L. van Gent

Dr. D. Ragni

Acknowledgments

This thesis marks the completion of my studies in Delft. I would like to thank, in no particular order, those who have made this experience both educational and enjoyable. My enthusiasm for the subject has only grown over the course of this work and that is due in no small part to my supervisors. They spent many hours teaching me the ways of the experimentalist; from PIV arrangements and wind tunnel time to insightful discussions of results and derivations. I also owe my gratitude to the technical staff of the high speed laboratory whose assistance and willingness to help made the work possible.

Outside of the lab, and those that I got to know in the lab, were friends that truly hallmarked my time as a student. I thank them for the years of lighthearted banter and tomfoolery and the positive effect that they have had on me. I would also like to thank my girlfriend for her ever-present positivity and good humor, which helped me through the times of experimental gremlins and disheartenment. In closing, I would like to express gratitude to my family who has always supported me in my endeavors, for that I am sincerely thankful.

Onward and upward.
-Steve

Abstract

This thesis has experimentally investigated the effect of an exhaust plume and variations in nozzle length on the wake of an axisymmetric backward facing step model. All cases were tested at Mach 0.7 with a Reynolds number, $Re_D = 1.0 \cdot 10^6$. The primary measurement technique was tomographic PIV with additional analysis being performed with schlieren imaging and pressure transducers. Three nozzle length configurations were tested both with and without the presence of an exhaust plume; each nozzle length corresponded to a different shear layer reattachment case. For fluidic reattachment in which the shear layer impinged upon the exhaust plume, a length of $L/D = 0.6$ was used. Solid reattachment used a length of $L/D = 1.8$. A hybrid case was also tested with a length of $L/D = 1.2$, which displayed reattachment near the nozzle exit.

Volumetric velocity data is captured in the region aft of the model from the point of flow separation to reattachment. A mean flow field analysis nicely resolves the main steady features such as the separated shear layer, the reattachment location, and the recirculation region. A mean flow field pressure reconstruction based on the momentum equation is applied. Results capture a 'jet-suction' effect for the fluidic reattachment case which is consistent with literature. For the two longer nozzle lengths there is no noticeable change in the coefficient of pressure caused by the presence of the exhaust plume.

To validate the aforementioned pressure reconstruction approach, a preliminary experimental campaign at Mach 0.7 and $Re_D = 1.3 \cdot 10^6$ was conducted prior to the main investigation. The PIV based pressure reconstruction shows excellent agreement with the pressure transducer measurements and good agreement with results from 3D BFS literature. This result is promising for the technique and produces good agreement with transducer results across a sizable Mach range.

The unsteady topological flow features are resolved using instantaneous PIV snapshots and high-frequency pressure transducers measurements. Turbulent structures are statistically investigated by the RMS of the velocity fluctuations. By that approach it is found that the presence of the exhaust plume has a stabilizing effect on the near-wake of the flow. With respect to nozzle length, it is found that the $L/D = 1.2$ case is the most turbulent due to the shear layer impinging near the nozzle exit. Unsteady pressure transducer measurements from the validation experimental campaign are used to show the decay of the first unsteady mode and the growth of the second upon moving downstream.

The conclusions from this thesis help to improve the understanding of the effect of reattachment location and exhaust plume presence on axisymmetric BFS flows. In doing so, designers of future launch vehicles can more adequately avoid the effects associated with poor nozzle length choices. It is foreseen that the hybrid case during transonic flight could cause problems due to the increased velocity fluctuations. Additionally, the present thesis has applied and validated the momentum based pressure reconstruction to a transonic flow using tomographic PIV.

Table of Contents

List of Figures

List of Tables

Nomenclature

Latin symbols

Symbol	Units	Description
C	[-]	Coefficient
D	mm	Main body diameter
L	mm	Afterbody length
M	[-]	Mach number
M	[-]	Magnification factor
N	[-]	Number of samples
Q	[-]	Tomographic reconstruction quality factor
R	J/(kg·K)	Specific gas constant
T	K	Temperature
U	m/s	Velocity
WS	pix.	Window size
a	m/s^2	Particle acceleration
d	mm	Focal distance
f	Hz	Frequency
f	mm	Focal length
$f_{\#}$	[-]	f-stop
h	mm	BFS step height
p	Pa	Pressure
r	m	Vortex radius
t	sec.	Time
u	m/s	Streamwise velocity component
v	m/s	Radial velocity component
w	m/s	Out-of-plane velocity component
x	mm	Streamwise distance
y	mm	Radial distance
z	mm	Out-of-plane distance

Greek symbols

Symbol	Units	Description

β	deg.	System aperture angle
γ	[-]	Ratio of specific heats
δ	mm	Boundary layer thickness
ϵ	[-]	Uncertainty
κ	pix/mm	Spatial PIV resolution
λ	m	Wavelength
ρ	kg/m^3	Density
μ	deg.	Mach angle
μ	kg/(m·s)	dynamic viscosity
μ	[-]	mean value
σ	[-]	Standard deviation
τ	μs	Particle response time

Superscripts

Symbol	Description
$'$	Fluctuating component
$\bar{}$	Mean component

Subscripts

Symbol	Description
∞	Freestream
0	Total
p	Particle
f	Fluid
cc	Cross-correlation
SR	Spatial resolution
max	Maximum
min	Minimum
r	Reattachment length
D	Main body diameter
p	Pressure
jet	Jet related
exit	Nozzle exit related

Acronyms

2D2C	Two-dimension, two-component
3D3C	Three-dimension, three-component
BFS	Backward facing step
CCD	Charge-coupled device
CFD	Computational fluid dynamics

CMOS	Complementary metaloxidesemiconductor
DEHS	Di-Ethyl-Hexyl-Sebacat
DEMO	Dienst Elektronische en Mechanische Ontwikkeling
ESA	European space agency
ECA	Évolution Cryotechnique type A
FCB	FESTIP control box
FESTIP	Future European Space Transportation Investigation Program
FFT	Fast Fourier transform
FOV	Field of view
MART	Multiplicative algebraic reconstruction technique
NASA	National Aeronautics and Space Administration
Nd:YAG	Neodymium-doped yttrium aluminium garnet
Nd:YLF	Neodymium-doped yttrium lithium fluoride
NPR	Nozzle pressure ratio
PIV	Particle image velocimetry
PME	Prandtl-Meyer expansion fan
POD	Proper orthogonal decomposition
ppv	Particles per voxel
PSP	Pressure sensitive paint
RMS	Root mean square
RMSD	Root mean square deviation
RS	Reynolds stress
SRB	Solid rocket booster
TI	Turbulence intensity
TLA	Three letter acronym
TST	Transonic supersonic tunnel
ZDES	Zonal detached eddy simulation

Chapter 1

Introduction

On the night of December, 11th, 2002, flight 157 of the Ariane 5 ECA was scheduled to lift-off into orbit carrying two French communications satellite, Stentor and Hot Bird 7. Due to break-up of the launch vehicle at T+456 seconds, these payloads never reached orbit. Several weeks later, on January, 7th, 2003 an inquiry board from the launch provider, Arianespace presented its findings for the cause of the failure (Arianespace, 2003). It was found that a leak in the cooling circuit of the Vulcain 2 nozzle led to critical overheating and a loss of structural integrity of the engine. In combination with the sideways forcing of the reattaching transonic flow emanating from the propellant tank, the Vulcain 2 was severely deteriorated, which caused a thrust imbalance and eventual loss of the vehicle.

In its closing remarks, the Arianespace investigation board made several recommendations. First, that the failure of Ariane 5 ECA flight 157 shall not affect future launches of the baseline (non-ECA) Ariane 5. Second, that engineers shall analyze, understand, and correct the design of the base region of the launch vehicle to ensure a high reliability of future launches. In the years since the failure of flight 157, engineers at Arianespace have worked to make the Ariane 5 one of the most reliable launch vehicles on the market. So reliable, in fact, that NASA has selected the Ariane 5 as the launch vehicle for the James Webb Space Telescope, a flagship NASA project of the last decades costing upwards of $8.8B. That stands as testament to the importance of understanding aerodynamic phenomena to overcome the associated engineering challenges.

Even if a rocket launch is successful, the region toward

Figure 1.1: Ariane 5 ECA flight 157 on the launch pad in Kourou, French Guiana, courtesy of ESA

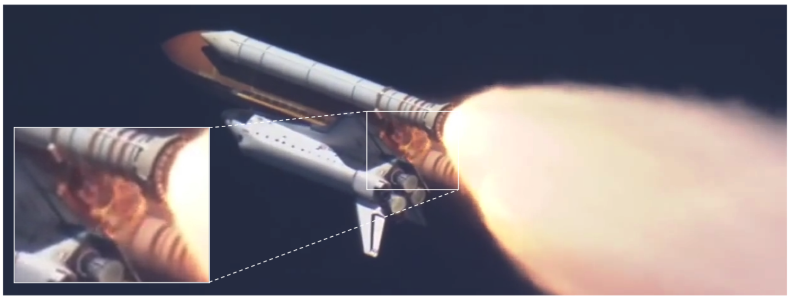

Figure 1.2: Visible recirculation region caused by SRB exhaust entrainment on the space shuttle orbiter, courtesy of NASA

the aft end of the vehicle presents challenges to the aerospace engineer. Figure 1.2 shows the space shuttle during ascent phase showing a peculiar 'fire ball' in the wake of the external propellant tank. This was a somewhat normal occurrence for the space shuttle and happened as a result of volatile exhaust gases caught in its wake being ignited by the underexpanded exhaust from the Solid Rocket Boosters (SRBs). Fortunately, engineers who worked on the space shuttle understood such phenomena and designed this portion of the vehicle to be able to withstand the resultant thermal loads.

The wake of a launch vehicle is one in which rhythmic, unsteady dynamics give rise to potentially stressful interactions, particularly during the transonic flight regime (Saile et al., 2015). One design constraint which could have an effect on these interactions is the length of the protruding nozzle and the presence of an exhaust plume. Many simplified axisymmetric Backward Facing Step (BFS) models exist to study such flows both experimentally and numerically. Recent advancements at the TU Delft in Tomographic Particle Image Velocimetry (PIV) allow for the experimental measurement of a volume of velocity in the wake region of such a rocket model (Elsinga et al., 2006); using such data, it is possible to resolve an associated pressure in said volume.

The present thesis will aim to combine these elements in an effort to investigate the effect of both nozzle length and the presence of an exhaust plume on the flow topology aft of a transonic launch vehicle. Particular interest will be paid to the effect that these changes have on the mean pressure and its agreement with measurements made by Deprés et al. (2004). These measurements will be made using tomographic PIV in combination with schlieren imaging and pressure transducers. This will allow for the unique combination of three-dimensional velocimetric data being used to make mean pressure reconstructions of the transonic flow field aft of an axisymmetric BFS model. With this new application of the measurement technique, the effect of nozzle length and exhaust plume presence will be concluded.

1.1 Research Objectives

The research goals of this thesis work is to better understand the effect of nozzle length and exhaust plume presence on the topological flow features aft of an axisymmetric BFS model.

Tomographic PIV will be employed to study this flow. To accomplish this goal, the research can be subdivided into several smaller objectives as follows.

- To visualize the mean flow field of a transonic BFS wake and to identify key topological features using tomographic PIV.
- To perform a mean pressure reconstruction using tomographic PIV data and to asses its performance for transonic BFS flows.
- To ascertain the effects of solid, hybrid, or fluidic reattachment on the aforementioned topological flow features, specifically the mean pressure in accordance with Deprés et al. (2004).

To meet these research objectives, the present thesis will be laid out as follows. Chapter 1 will serve as an introduction to the subject and to place the current work within that context. Chapter 2 will provide an introduction to the most relevant aspects of the backward facing step flows which are to be studied. The measurement and processing techniques which will be used to study the flow is outlined in Chapter 3. Practical matters in regards to the setup of the experimental investigations are presented in Chapter 4. Chapter 5 contains the results of the first experimental campaign which served to familiarize the researcher and validate the measurement techniques which are to be used. Results of the second experimental campaign studying the effect of exhaust plume and nozzle length are described in Chapter 6. Lastly, the major conclusions of the thesis and recommendations for future work are outlined in the concluding Chapter 7.

Chapter 2

Backward Facing Step Flows

Figure 2.1(a) shows an Ariane 5 beginning the ascent phase of its mission. A complex interaction occurs between the air flow over the propellant tank and the nozzle protruding from its base, which is an example of a flow geometry that resembles a Backward Facing Step (BFS). During the ascent to orbit, this important interaction can have serious consequences for the mission if not addressed properly and adequately understood.

(a) Ariane 5 propellant tank and engine interaction courtesy of ESA

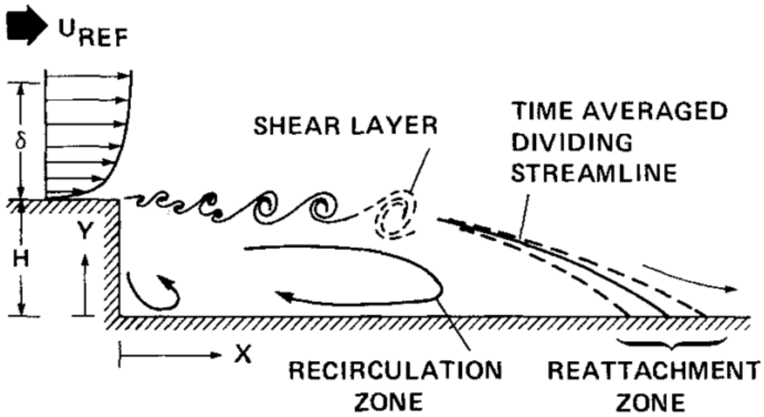

(b) BFS flow topology (Driver et al., 1987)

Figure 2.1: A 'real world' and simplified BFS flow field

To better understand such flows over actual rockets, like the Ariane 5, research is typically conducted on a simplified, step-wise, geometrical shape as illustrated in Figure 2.1(b). Comparing the simplified model in Figure 2.1(b) to the very real world Ariane 5 in Figure 2.1(a), the fore step of the BFS represents a propellant tank and the region below the step represents the nozzle. In this sense, the topological flow features depicted in Figure 2.1(b), also occur, to some degree, between the propellant tank and the nozzle on the Ariane 5.

A large amount of literature has been devoted to two-dimensional BFS models. The models which are to be studied in the present thesis are three-dimensional, axisymmetric BFS models; that is to say, they feature radial symmetry about an axis that is parallel to the x axis in Figure 2.1(b). This is done to more closely resemble the actual Ariane 5 launch vehicle seen in Figure 2.1(a) and gives rise to several differences when compared to a two-dimensional BFS. The following chapter aims to familiarize the reader with the aerodynamic phenomena of the BFS.

2.1 Topological Flow Features of the BFS

All of the topological features which are to be described in the present section are connected by their mutual influence upon one another. As such, the flow field displays both dynamic and steady features which will be discussed herein. The flow in the wake of the BFS is one of large scale dynamics and low-frequency, undulating motions caused by the interaction between the following topological features (Hudy et al., 2007).

2.1.1 Separated shear layer

The separated shear layer forms the first of these features, emanating from the edge of the BFS and flowing downstream to reattach to the lower step. As the flow detaches, a strong velocity gradient, bounded by the freestream and the recirculation region below causes a shearing force in the flow. This results in Kelvin-Helmholtz instabilities, which cause a breakdown of the shear layer as it 'rolls up' into spanwise oriented eddies (Robinson (1991), Scharnowski et al. (2016a)). These eddies that emanate from the edge of the BFS constitute a large amount of in-plane vorticity. Counter-rotating eddies grow in size and pair together due to viscous shearing while convecting downstream (Browand (1966), Winant and Browand (1974)); According to Troutt et al. (1984) and Hudy et al. (2007), eddies grow to a maximum size equal to the step height, h and result in a widening of the shear layer as shown in the time-averaged BFS flow field in Figure 2.1(b).

This complex interaction, depicted step-by-step in Figure 2.2, is rooted in a momentum imbalance caused by the unsteady breakdown of shear layer eddies, which in turn, leads to an unsteady ingestion of fluid into the recirculation region (Eaton and Johnston, 1981). Therefore, instabilities in the shear layer affect, and are affected by, the other main BFS flow features. Figure 2.1(b) shows a reattachment 'region' because the interaction between these features gives rise to a low-frequency, 'flapping' type motion of the BFS wake (Driver et al., 1987). This 'flapping' motion is identified by Schrijer et al. (2014) as the first unsteady mode of the BFS wake and is shown in Figure 2.4(a).

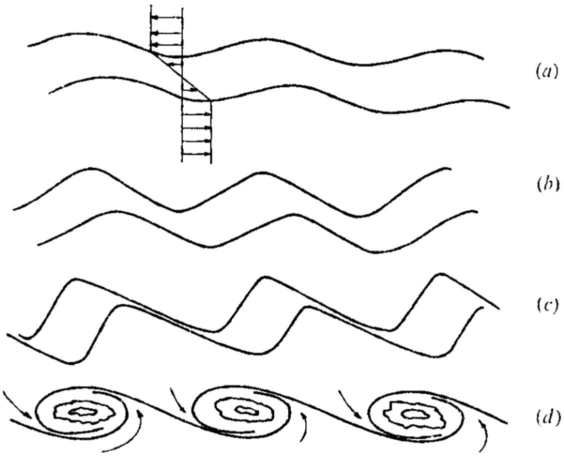

Figure 2.2: Vortex formation and pairing in the separated shear layer according to Winant and Broward (1974)

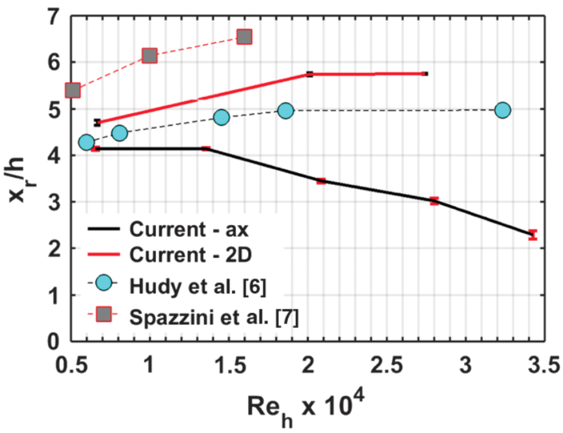

Figure 2.3: Reattachment length scaling with respect to Re_h (Gentile et al., 2016)

The Kelvin-Helmholtz instabilities which give rise to the vortex pairing in the shear layer are exacerbated when three-dimensional models are considered (Robinson (1991), Kostas et al. (2002)). This increase has an effect on the distance which the shear layer covers before reattaching as evidenced by Figure 2.3. Generally, the axisymmetric model may give rise to unstable helical fluid motion about the afterbody as discussed by Deck and Thorigny (2007) and Weiss et al. (2009).

2.1.2 Reattachment location

The separated shear layer that emanates from the base of the BFS flows downstream to reattach upon the lower step. In the time-averaged wake of an axisymmetric step this location is expected to be at approximately $x/D = 1.0$ (Schrijer et al., 2014). If the shear layer reattaches to a solid surface, it is said to be an instance of 'solid' reattachment; in the case of no 'reattachment' to a solid surface but rather into an exhaust plume or other fluid, it is said to be an instance of 'fluidic' reattachment. These instances, as outlined by Deprés et al. (2004), will form the basis for the chosen cases for this thesis with an additional 'hybrid' case featuring intermittent solid and fluidic reattachment.

As stated previously and seen in associated figures, the reattachment length is often non-dimensionalized by the step height, h in a two-dimensional BFS and by the main body diameter, D in an axisymmetric BFS. Figure 2.3 shows the scaling of the reattachment length, x_r with respect to Reynolds number. Therein, it can also be seen that three-dimensional, axisymmetric models feature a consistently decreased mean reattachment length according to Gentile et al. (2016). Additionally, it can be seen that the distance to the time-averaged reattachment location is expected to vary little over a range of subsonic Mach numbers which is in accordance with findings reported by Scharnowski et al. (2016b).

Variation in the point of reattachment is caused by the unsteadiness of the other two flow features discussed herein. The cause of this variability is both the 'flapping' of the shear layer and the momentum transfer into- and out of the recirculation region. A time-averaged mean reattachment location is approximately $x_r = 5h$ for a broad range of subsonic flows according to Scharnowski et al. (2016b). Additionally, the mean reattachment length can be affected by the state of the incoming boundary layer (Isomoto and Honami (1989), Adams and Johnston (1988)) and the Reynolds number (Eaton and Johnston, 1981). All authors state that a higher Reynolds number, fully turbulent boundary layer prior to flow separation at the BFS edge, provides a more consistent reattachment length when compared to a laminar, low Reynolds number case, which shows greater unsteadiness in x_r. For this reason, both models used in the experiments feature a 'trip strip' on the nose cone to ensure a fully developed turbulent boundary layer at the point of separation.

2.1.3 Recirculation region

The recirculation region is bounded by the walls of the BFS and the separated shear layer above, extending to approximately the point of reattachment (Eaton and Johnston, 1981); in turn, it also forms a part of the velocity gradient which creates said shear layer. At the point of reattachment, some fluid is directed upstream which feeds the recirculation region. Inside the clockwise rotation of the recirculation region, there is a region of strong 'backflow', the strength of which affects the velocity gradient that forms the shear layer (Bradshaw and Wong, 1972). The vortical motion of the recirculation region transfers mass inward from the outer edges causing a build-up at the vortex core; as the fluid reaches the vortex core it is expelled 'out-of-plane' giving rise to some three-dimensional motion (Hall et al., 2003).

Seen in the lower left corner of Figure 2.1(b) is the secondary counter-rotating, recirculation region, a feature belonging to low-speed BFS flows. The secondary vortex is fed by fluid from the primary vortex according to Hudy et al. (2007). This vortex is found to decrease in size with increasing Reynolds number according to Spazzini et al. (2001) and Hudy et al. (2007). Other researchers, namely Bitter et al. (2011) and Schrijer et al. (2014), noted an absence or insignificance of the secondary recirculation region when measuring at Mach 0.7. As these experiments have commonality with the present work, it can be expected that the secondary recirculation region will be insignificant due to the high Reynolds number.

Due to the variability in the amount of fluid ingested from the impinging shear layer, the recirculation region also displays unsteady motion. This motion is linked to the momentum injection and ejection as seen in Figure 2.4(b) (Schrijer et al., 2014). As fluid enters the region, the angle with which the separated shear layer impinges upon the lower step increases and allows more fluid to enter the region. The entrained fluid reaches a limit and bursts, ejecting momentum and beginning the cycle anew (Driver et al., 1987). During this process of varied fluid entrainement, the backflow and strength of the recirculation region will also vary.

Final comment on combined instability Fuchs et al. (1979) first identified that the

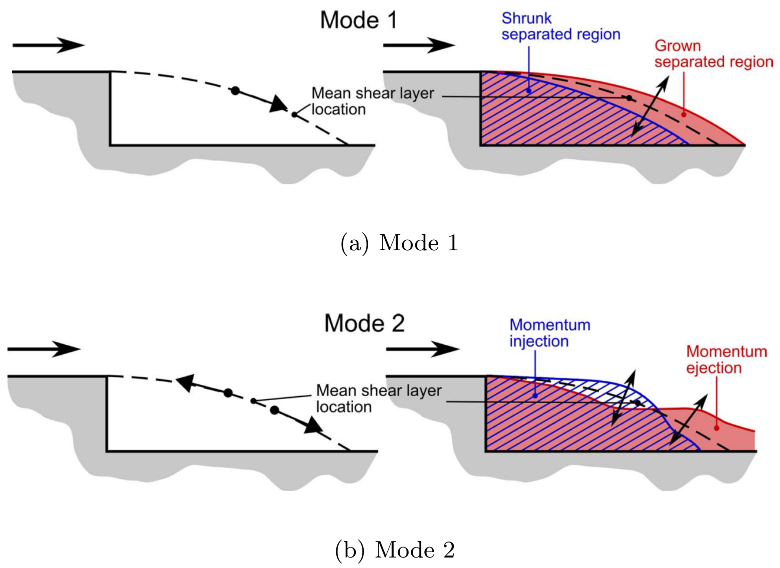

Figure 2.4: POD modes of the BFS as identified by Schrijer et al. (2014)

unsteady flow in the wake of the axisymmetric BFS forms coherent, antisymmetric flow structures. Work by Deprés et al. (2004) confirmed the existence of this unsteady mode experimentally for transonic flows. Deck and Thorigny (2007) investigated the unsteadiness numerically and also identified the existence of such an antisymmetric unsteady mode at the same frequency as other features; thus, it was concluded that there is an ordered structure to the large scale coherent motion in the wake of the axisymmetric BFS. Rigas et al. (2014) and Gentile et al. (2016) defined the unsteady mode as an antisymmetric vortex shedding that slowly precesses about the longitudinal axis.

2.2 Geometrical Impact on the Flow Field

In an effort to investigate the effects of geometrical variations or enhanced realism, research is directed toward moving from the simplified BFS in Figure 2.1(b) to a more realistic model. There are many controlled variations that can be of interest, most notably the presence of an exhaust plume and/or changes to the geometry of the BFS.

2.2.1 Previous work involving simulated exhaust plumes

One of the more important pieces of literature pertinent to this thesis is that by Deprés et al. (2004). In the article, it is concluded that the length of the nozzle is a determining parameter for the mean and unsteady flow features in the wake of an axisymmetric BFS at transonic Mach numbers. Additionally, it is found that the exhaust jet only significantly alters the flow field when the nozzle is sufficiently short to allow for fluidic reattachment.

Scharnowski et al. (2016b) also states that the topological features discussed in section 2.1 remain largely unaffected by the presence of an exhaust plume when the shear layer features solid reattachment.

In the near wake of the nozzle, the presence of an exhaust plume can have a stabilizing effect as concluded by Wolf et al. (2012). Figures 2.5 and 2.6 from Deck and Thorigny (2007) and Weiss and Deck (2011), respectively show these two cases for a nozzle length of $L/D = 1.2$. Without the exhaust plume, the formation of a recirculation region at the nozzle exit is visible and also observed by Schoones and Bannink (1998). In much the same way as the unsteadiness of the topological flow features discussed in section 2.1, the new shear layer and recirculation region possess their own unsteadiness. Deck and Thorigny (2007) and Wolf et al. (2012) state that the presence of the exhaust plume largely removes these features but causes a more turbulent mixing layer further downstream along the jet-wake interface.

2.2.2 Previous work involving nozzle size variations

As noted by both Deprés et al. (2004) and Scharnowski et al. (2016b), the change in nozzle length will have a greater effect on the flow field than the presence of the exhaust plume. That is not to say that the jet will have little impact. Beyond the topological features discussed in section 2.1, Wolf et al. (2012) states that the near wake of the BFS is greatly affected by the presence of an exhaust plume. In this region, the accelerating effect of the exhaust on the mixing layer causes an elongation of the recirculation region. For the present experiment, this change will be downstream of the field of view (FOV) but should not be omitted from the discussion.

The size and presence of an afterbody is of importance for the presence of the antisymmetric mode that slowly meanders about the wake. It is noted by Rigas et al. (2014), for a model without afterbody at approximately $Re_D = 2 \cdot 10^5$, that the unsteady, 'symmetry-breaking' vortex shedding does not manifest itself as a difference in mean pressure. Gentile et al. (2016) also noted the antisymmetric vortex shedding for a model without afterbody, as previously noted, and concluded that the meandering region is largely disrupted by the presence of an afterbody; by testing varying afterbody diameters ($d/D = 0 - 0.8$), it is found to further diminish when the diameter of the afterbody grows, relative to that of the main body. Both authors (and Grandemange et al. (2014) for a sphere at $Re_D = 1.9 \cdot 10^4$) state that due to the low frequency of rotation, that statistical axisymmetry is found in the time-averaged flow field. As such, the present research cannot expect to find evidence of this unsteady mode when viewing the time-averaged wake of the BFS; rather, instances may be seen in the individual PIV snapshots.

Wolf et al. (2012) additionally characterizes the effect of the afterbody for a subsonic flow at $M = 0.2$ by testing a model with ($L/D = 1.2$) and without afterbody. Therein it is stated that the presence of a solidly attaching afterbody has a stabilizing effect on the flow field. Generally, the same topographic features are present when comparing a bluff body to an axisymmetric BFS, but macro-scale instabilities of $St = 0.2$ are largely diminished. Statistical turbulence levels are greatly decreased due to the suppression of large-scale dynamic modes.

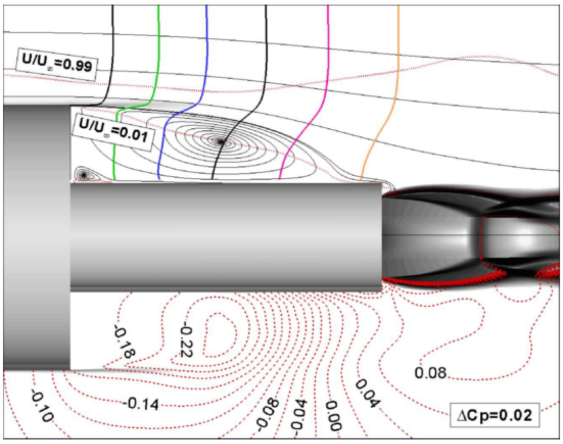

Figure 2.5: BFS with exhaust plume showing time-averaged velocity (top) and coefficient of pressure (bottom) (Deck and Thorigny, 2007)

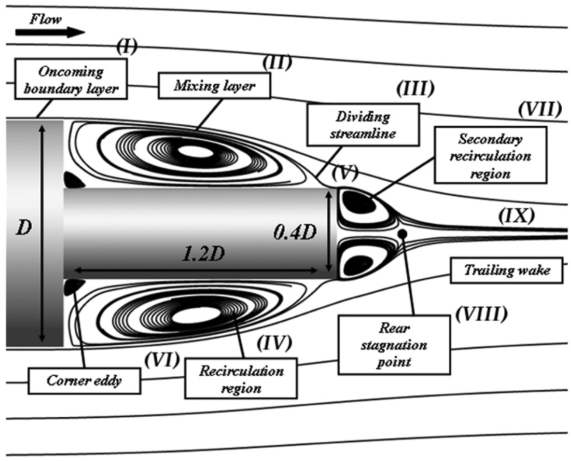

Figure 2.6: Model with afterbody of $L/D = 1.2$ without exhaust plume (Weiss and Deck, 2011)

2.3 Relevant Non-dimensional Numbers

The following non-dimensional numbers are paramount to the discussion of the flow field as previously noted in the description of topological features.

2.3.1 Reynolds number

The Reynolds number is a non-dimensional ratio between the inertial and viscous forces in a moving fluid. Equation 2.1 defines the Reynolds number where the terms in the numerator represent the inertial forces and those in the denominator represent the viscous forces. A characteristic length, L defines the Reynolds number; in regards to BFS flows, the Reynolds number is often based on the step height, h or the main body diameter, D.

$$\text{Re} = \frac{\rho U_\infty L}{\mu} \tag{2.1}$$

An important benefit of the Reynolds number is that it allows for the comparison of different flow cases in which viscosity is relevant; two flows may be of differing parameters but an equal Reynolds number will be required for similarity. For this reason, experimentalists use it to define the flow being studied such that other researchers can compare results. Certain topological features, such as the secondary recirculation zone, can also be tied to certain Reynolds numbers or ranges thereof; Spazzini et al. (2001) and Hudy et al. (2007) both note the lack of such a feature for high Reynolds number flows.

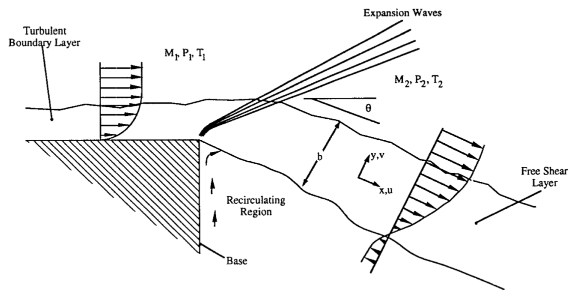

Figure 2.7: Topological features of a supersonic BFS flow

2.3.2 Mach number

The Mach number is a non-dimensional ratio between the local flow velocity, u and the speed of sound, a. In an ideal gas, the speed of sound is purely a function of the temperature, T, the ideal gas constant, R, and the ratio of specific heats, γ. At Mach 1, the flow speed is equal to that of the speed of sound and the vehicle is traveling at sonic speeds.

$$M = \frac{u}{a} = \frac{u}{\sqrt{\gamma R T_\infty}} \tag{2.2}$$

For the axisymmetric BFS flow this has significant consequences and brings about great differences between the subsonic ($M < 1$) and supersonic ($M > 1$) cases. Up to this point, the figures and discussion has centered around subsonic BFS flows; Figure 2.7 shows a supersonic BFS. As the flow travels over the edge of the BFS the perceived area increases and dependent upon the Mach number, the flow will behave differently. By the *area-velocity relation* the flow will either decelerate or accelerate depending on whether the flow is sub- or supersonic, respectively (Anderson, 2011).

Supersonic BFS

Supersonic flow and the appearance of a Prandtl-Meyer Expansion fan (PME) cause a strong downturn in the flow, leading to a drastically reduced reattachment length as seen in Figure 2.7. (Scharnowski et al., 2016b) tested a two-dimensional BFS flow over a broad Mach number range and found a reattachment length of $5h$ for subsonic and flows and approximately $3h$ for supersonic flows; slight variation is noted over sub- or supersonic ranges. Chen et al. (2012) also notes a shortened reattachment length of 3-4h for a supersonic BFS.

2.3.3 Coefficient of pressure

The coefficient of pressure, C_p is a non-dimensional representation of the relative pressure at a point in the flow field. Equation 2.3 shows the coefficient of pressure, C_p where p is the static pressure at a point and p_∞ is the freestream pressure; the denominator of the left statement is the dynamic pressure for incompressible flows, which can also be recast for compressible flows by the ideal gas law and the speed of sound, a.

$$C_p = \frac{p - p_\infty}{\frac{1}{2}\rho_\infty U_\infty^2} = \frac{p - p_\infty}{\frac{1}{2}\gamma M^2} \tag{2.3}$$

Many bodies of research used pressure transducers mounted in the model to give insight into the wall pressure distribution. Figure 2.5 shows what such a pressure distribution will look like with a minimum wall C_p value measured on the nozzle at $x/D = 0.5$ (Deprés et al. (2004), Deck and Thorigny (2007), Gentile et al. (2016)). One of the benefits of PIV will be the simultaneous measurement of pressure on the model and in the flow.

2.3.4 Strouhal number

The Strouhal number, seen in equation 2.4 is a non-dimensionalized frequency used to represent oscillating flows. Frequencies, f are non-dimensionalized by the characteristic length, in this case diameter, D, of the body and the freestream velocity, U_∞. By doing so, comparison between the unsteady flow features of one body can be compared to those of another. For BFS type flows specifically, the Strouhal number is used to describe the low-frequency, ($St \leq 0.2$) unsteady modes in the wake.

$$St = \frac{f \cdot D}{U_\infty} \tag{2.4}$$

Chapter 3

Particle Image Velocimetry and Pressure Reconstruction

Flow visualization occurs intrinsically on a regular basis. One does not have to look far to observe fluid motion by the simple relationship between a flow and a particle nested within. Figure 3.1 shows two such occurrences. The first, in Figure 3.1(a), shows snowflakes being illuminated by a flood light and the second, in Figure 3.1(b), shows dust particles in a ray of sunshine cast through a window. When viewing such situations, one can make the simple connection from the apparent motion of the particles to the overall motion of the fluid in which they are suspended. With this concept in mind, an extrapolation can be made to particle image velocimetry.

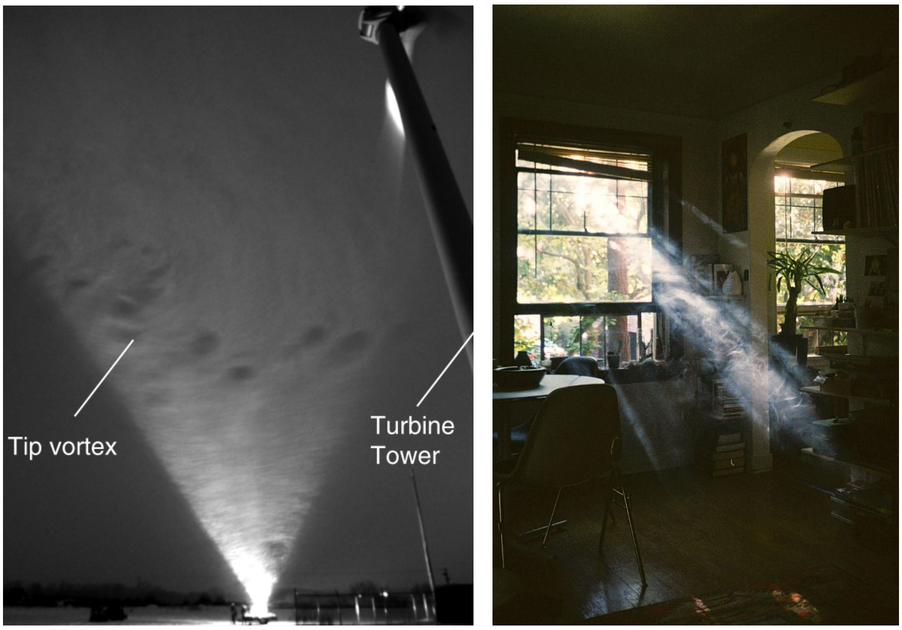

(a) A wind turbine in a snow storm (Hong et al., 2014)

(b) A dusty room

Figure 3.1: Flow visualization analogies

3.1 Particle Image Velocimetry

Particle Image Velocimety (PIV) follows a working principle similar to the innate visualization techniques seen in Figure 3.1. Namely, the fluid that is to be observed, whether the snowstorm about the wind turbine or the still air in the room, is seeded with particles, in this case snowflakes or dust, and those particles are illuminated and imaged. Practically, for PIV experiments, these details are not left to nature or circumstance and are instead, carefully chosen details of the experimental arrangement.

In its most basic sense, PIV involves adding reflective particles to a flow whose influence is small enough not to change its nature, but can rapidly and faithfully follow the flow. The field of view (FOV) which is to be recorded is starkly illuminated against the dark; this ensures that only those particles traveling through the FOV will scatter light. As these particles travel through the FOV and are illuminated, digital cameras quickly capture a succession of images showing small, detailed displacements of a particle field. The result is two images separated by a known time step, Δt.

Each of the images which form a pair are identically subdivided into small interrogation windows. The change which occurs within one interrogation window over a time step, Δt is quantified by means of a cross-correlation function. Displacement of the average particle within a window is quantified by the distance from the center of the window to the resultant

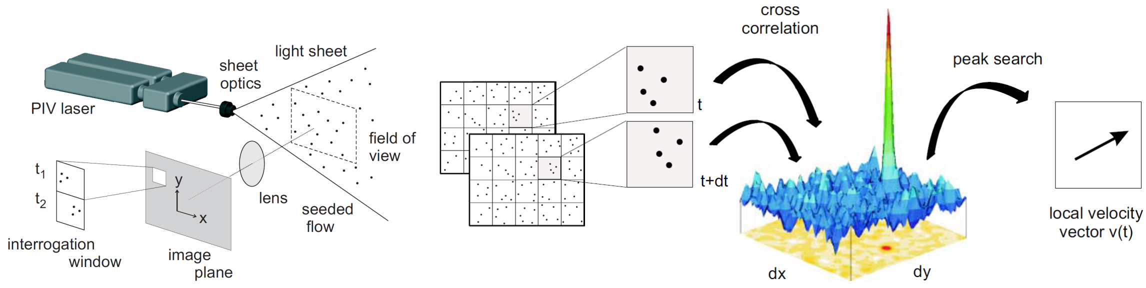

(a) A two-dimensional PIV arrangement

(b) The cross-correlation process of two PIV images

Figure 3.2: PIV processing courtesy of LaVision GmbH (2015)

cross-correlation peak; such a plot is visible in Figure 3.2(b). Now both the displacement and time step are known, which results in an average velocity vector for the particles within an interrogation window.

3.1.1 Seeding

Snowflakes or dust may lend some insight, but to better understand the flow, PIV makes use of more carefully chosen particles. Particles which are seeded into the flow are expected to accurately follow the flow and scatter enough light such that they can be properly imaged; it is, after all, their motion that will be recorded and it is expected that this motion faithfully represents that of the flow. As such, these aforementioned properties are of importance when selecting a seeding particle for an experiment.

For high-speed PIV common particle choices are titanium dioxide (TiO_2) and Di-Ethyl-Hexyl-Sebacat (DEHS). These particles are known to accurately follow the flow in which they are immersed and their performance is quantified by the particle response time, τ_p. The response time is based on the time taken for the particle to match 63% of the new fluid velocity after a step change according to Scarano (2013b); this value should be below the smallest time scale of the flow to be studied. The difference in particle and fluid flow velocity is defined as the slip velocity, $u_s = u_p - u_f$. For the aforementioned DEHS and TiO_2 particles, the particle response time, τ_p is approximately 2 μs. The performance of such particles, and several others, are investigated by Ragni et al. (2011) over a shockwave because this affords the researcher a step-like decrease in velocity.

Particle Stokes number The Stokes number is the ratio between characteristic flow time and particle response time and is calculated to ensure that particles faithfully follow the flow. Equation 3.1 shows the equation for the Stokes number, S_k where τ_p is the particle response time and D is the characteristic length, which for the present experiment is the diameter of the main body (Brennen, 2005). A turbulent, high Reynolds number presents the most

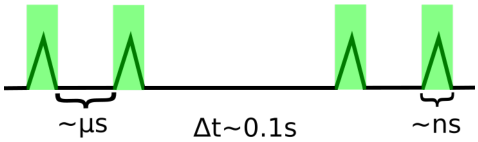

Figure 3.3: Pulse separation time and laser illumination for transonic PIV

challenging case for the particles due to the varying length scales that are present (Tropea et al., 2008). According to Tropea et al. (2008), a particle faithfully follows the streamlines of a flow when the particle Stokes number, $S_k \ll 1$.

$$S_k = \frac{\tau_p U_\infty}{D} \tag{3.1}$$

For the present experiments, a freestream velocity of 245 m/s is estimated for the subsonic cases and 450 m/s for the supersonic case, this results in a Stokes number, $S_k = 0.0098$ and $S_k = 0.018$, respectively. Though the supersonic case is larger, the subsonic value is less than 0.1 and so it can be assumed that the DEHS particles will follow the flow accurately with an error less than 1% (Tropea et al., 2008).

3.1.2 Illumination

A flood light or a ray of sunshine does not ideally provide the properly defined illuminated regions that are required for PIV. Lasers are the light source of choice for many PIV experiments currently being performed, though there is potential for LED based systems. The two most common laser types are the Nd:YAG and Nd:YLF. The benefits of such laser systems are their high pulse frequencies, high energy per pulse, and a nicely collimated beam that allows for strict control of the illuminated region. Each laser type is best suited to a particular experiment based on its pulse energy in milli-Joules and its frequency in Hertz. Whereas the Nd:YAG system can provide pulse energy values upwards of 400 mJ, its repetition rate is relatively low at 30 Hz or less (Raffel et al., 2007). For applications requiring significantly higher recording rates, the Nd:YLF system is able to achieve frequencies up to 10,000 Hz; this comes at a cost of reduced pulse energy up to 30 mJ.

The illumination source thus plays a significant role in the type of measurements that can be made of a given flow regime. If the measurement frequency is high enough such that a sequence of resultant vector fields is correlated in time, then the results are said to be time-resolved. At the cost of such a high measurement frequency comes a reduced amount of energy per laser pulse. Thus the experimentalist faces a choice between measurement volume that is to be resolved and the frequency of the measurement. This relationship between the spatial size of the measurement FOV and the laser energy required quickly forms a limiting factor for the PIV technique.

Figure 3.3 shows the timeframe for a typical high-speed PIV recording. The pulse separation time is typically on the order of microseconds and is the fixed amount of time between an image pair. The pulse duration is on the order of nanoseconds and should be fast enough so as not to blur the particle tracks. Lastly, the time step, Δt is what separates one resultant vector field from those preceding and following it.

3.1.3 Imaging

Instead of relying on the qualitative analysis of the human eye to assess the flow, PIV setups use digital cameras to make quantitative measurements. From the digital image, an average displacement in an interrogation window is known in pixels but these value needs to be related to a physical distance in the field of view; this relation is calculated by the optical properties of the imaging system. The image distance, d_i is calculated using the focal length, f and the object distance, d_o in equation 3.2 (Scarano, 2013b).

$$\frac{1}{f} = \frac{1}{d_i} + \frac{1}{d_i} \tag{3.2}$$

The ratio of the image distance, d_i and the object distance, d_o defines the magnification factor, M as seen in equation 3.3

$$\mathrm{M} = \frac{d_i}{d_o} \qquad \mathrm{M} = \frac{\text{pixel size} \cdot \text{number of pixels}}{\text{field of view}} \tag{3.3}$$

By knowing the size and number of pixels on the sensor of the digital camera, the imaged field of view can be defined in standard units of length. The resolution of the system is then defined as the ratio of the length of the field of view versus the amount of pixels in that same direction. By knowing the f-stop, $f_{\#}$ of the lens, the wavelength of the laser light, λ, and the magnification factor, M, the focal depth of the system can be calculated by equation 3.4 (Scarano, 2013b).

$$\delta_z = 4.88 \cdot \lambda \cdot f_{\#}^2 \left(\frac{\mathrm{M}+1}{\mathrm{M}} \right)^2 \tag{3.4}$$

Focal depth, δ_z of the system defines the depth in which imaged particles are in focus. The experimentalist can easily control this depth by adjustment of the f-stop of the lens but this comes with a caveat. As the f-stop increases, the focal depth increases but the amount of light intensity captured by the camera is decreased, thus requiring more laser energy. As will be discussed later, this problem quickly devolves into a limitation of tomographic PIV in which the measurement volume is restricted by inadequate laser power.

Lastly, based on an estimation of the freestream velocity, one can make a prediction for the freestream particle displacement. When performing the aforementioned cross-correlation function, it is desirable to have the particles traverse approximately one fourth of the interrogation window. This is done so that a majority of particles are imaged within the same interrogation window and can thus be used to calculate a proper correlation peak. Knowing the final size of the interrogation window allows for the proper setting of the time step, Δt between images.

Peak locking

The images are well resolved when the particle image size is several times larger than the pixel size. Peak locking occurs when particle images are smaller than one pixel, in which case the cross-correlation approach can no longer measure sub-pixel displacements due to the inability to perform a Gaussian correlation peak fit. This error is essentially a discretization effect caused by small motions of the seeding particles being registered as the minimum resolvable displacement. To avoid peak locking, the imaging system should be arranged such that individual particles in the flow are captured over several pixels of a resulting image.

Camera types Digital cameras which are typically used for PIV are of the CCD or CMOS variety and are paired with a lens suitable to the measurements. A comparative assessment between the two camera types is made by Hain et al. (2007). As with the laser type, the choice of camera is largely driven by the type of measurements that are to be made. Though CCD cameras are most often used in PIV according to Raffel et al. (2007), CMOS cameras are 'catching-up'. CMOS performs best in low light intensity cases and can help to account for the run-away tomographic volume problem previously mentioned; additionally, CMOS cameras without an image intensifier are the best option for time-resolved measurements due to their high measurement frequency. Lastly, the CCD type systems are best suited to experiments requiring high-quality, high-resolution measurements (Hain et al., 2007).

3.2 Tomographic PIV

Following a foundational article by Elsinga et al. (2006), tomographic PIV has seen much development at the TU Delft. Whereas the previously discussed PIV technique resolves two velocity components on a single plane, the tomographic PIV technique is able to resolve three velocity components in a three-dimensional volume. This is done by having a minimum of four cameras viewing an illuminated volume from varying angles. All cameras are defined within a single spatial coordinate system and a polynomial fit allows for tomographic reconstruction of the imaged volume.

3.2.1 Self-calibration

The calibration process for a tomographic PIV system begins with a geometric calibration using a plate of predefined size. Thereafter, the calibration is further refined by means of an iterative self-calibration process carried out during a preliminary 'run'; in this manner it is possible to correct for potential camera movement or light sheet misalignment. PIV images are made with a reduced seeding density, each camera identifies particles, and based on an allowed disparity, the location of individual particles within the volume is ascertained. This procedure makes incremental corrections to the polynomial mapping function until it achieves sub-pixel accuracy (Wieneke, 2008). During each step of the process, the disparity within the system is quantified as a residual triangulation error.

3.2.2 Ghost particles

As a result of viewing the same particles from different angles, an inherent velocity bias can occur as a result of tomographic reconstruction. When two separate cameras view the same grouping of particles from different angles, perceived spatial depth may cause the tomographic PIV system to 'capture' more particles than are actually present; these extra particles are known as ghost particles and will cause a velocity error in the eventual reconstruction of the volume (Elsinga et al., 2011). According to Elsinga et al. (2011), the velocity error due to ghost particles can be mitigated by increasing the depthwise particle displacement beyond the value of a single particle image diameter; this imposes a constraint on the maximum allowable particle density for a tomographic PIV experiment.

3.3 Pressure Reconstruction

Up to this point, the discussion has revolved around the use of PIV to measure velocity in a fixed field of view. The resultant velocity fields can lend many insights into the flow topology; one such insight is the pressure as a function of velocity. Gurka et al. (1999) first demonstrated the ability to make such pressure 'reconstructions' using velocity fields derived from PIV. By the momentum equation, the pressure gradient is defined as a function of the velocity gradient and its spatial gradients, which is known from PIV measurements; the resultant Poisson equation is solved for p/p_0.

When compared to computational fluid dynamics (CFD) approaches to resolve pressure in a BFS flow, the PIV derived approach has a distinct advantage. The turbulence model for the pressure reconstruction directly follows from the flow being measured and avoids the use of a closure model as is necessary with a RANS based CFD approach. Whereas the present method requires only a relation by the momentum equation, a CFD approach would need to satisfy the equations of continuity, momentum, and energy. Commonality between the computational and experimental approaches is found in their governing equations being Reynolds averaged in the situation that only time-averaged pressure is required and/or when no time-resolved velocity data is available. This involves separating each component of velocity into a mean and fluctuating term; additionally, it gives rise to the Reynolds stress terms.

3.3.1 Compressibility

However, as the present work is to investigate transonic flows, the approach outlined by Gurka et al. (1999), which applies to incompressible flow, will need to be adapted to account for the effects of compressibility. Such an extension to compressible flows has been outlined by van Oudheusden et al. (2007); important assumptions to the approach will be outlined in the following section.

The flow is assumed to be adiabatic at all points, this allows for the temperature ratio, T/T_0

to be purely a function of Mach number, M, ratio of specific heats, γ, and the velocity ratio, U/U_∞ at all points in the flow. This adiabatic assumption results in equation 3.5 and is valid when there is no significant heat transfer to or from the flow (White, 2006).

$$\frac{T}{T_\infty} = 1 + M_\infty^2 \left(\frac{\gamma - 1}{2}\right)\left(1 - \frac{\vec{U}^2}{U_\infty^2}\right) \tag{3.5}$$

As stated previously, the velocity ratio, $\vec{U}/U_\infty$ is gathered from PIV, the Mach number, M is calculated using known conditions for the flow, and a standard value of $\gamma = 1.4$ for air is used. By the isentropic flow assumption, the temperature ratio seen in equation 3.5 can be extended to find the pressure ratio, p/p_∞ as seen in equation 3.6.

$$\frac{p}{p_\infty} = \left(\frac{T}{T_\infty}\right)^{\frac{\gamma}{\gamma-1}} \tag{3.6}$$

Though the relation shown in equation 3.6 holds for regions of isentropic flow, such an assumption is invalid in the strongly separated wake of a BFS. It is exactly that region of the flow which is of interest, however, as will be discussed later in section 3.3.5, the isentropic relation seen in equation 3.6 will form an important boundary condition for the solving of the Poisson equation.

$$\rho = \frac{p}{RT} \tag{3.7}$$

By the ideal gas law, seen in equation 3.7, an estimate for the density is made based on the pressure and temperature of the flow at a given point. This is necessary because, unlike in the original formulation by Gurka et al. (1999), the flow is compressible and the density will form an additional variable. The necessary steps to accommodate this new variable are outlined by Souverein et al. (2007) and van Oudheusden (2013).

3.3.2 Momentum equation

The momentum equation, which forms the basis for the approach, is seen in equation 3.8. This formulation contains the material derivative, $D\vec{U}/Dt$, which follows a fluid parcel through a changing vector field; the material derivative term is shown in an expanded form and is comprised of an unsteady time dependent term and a gradient of the velocity field.

$$\nabla p = -\rho\left(\frac{\partial \vec{U}}{\partial t} + \left(\vec{U} \cdot \nabla\right)\vec{U}\right) + \mu \nabla^2 \vec{U} \tag{3.8}$$

Because the present experimental work aims to study mean pressure field of a transonic flow, several terms can be discarded; those terms being the unsteady time derivative and the viscous term. The time dependent term because the mean flow field will be invariant in time and the viscous term because the Reynolds number will be sufficiently high, $\mathcal{O}(10^6)$. By the aforementioned assumptions and the momentum equation as seen in equation 3.9, the system is now adequately defined such that the pressure, p can be determined.

$$\nabla p = -\rho\left(\vec{U}\cdot\nabla\right)\vec{U} \tag{3.9}$$

Non-conservative approach The objective is to write the pressure-gradient term using solely those terms that are known when using PIV measurements. To do so, the present experiment follows the non-conservative approach as outlined by van Oudheusden (2008). As such, the non-conservative formulation of the momentum equation, in combination with stated assumptions, is seen in equation 3.10.

$$\frac{1}{p}\frac{\partial p}{\partial x_i} = \frac{\partial \ln(p/p_\infty)}{\partial x_i} = -\frac{1}{RT}u_j\frac{\partial u_i}{\partial x_j} \tag{3.10}$$

In equation 3.10 it can be seen that the density terms have been replaced by an ideal gas law based term as was indicated earlier; this is manifested as the specific gas constant, R, temperature, T, and pressure, p terms seen in the denominator. The left hand side of equation 3.10 also shows the recast pressure term, which is done for the Poisson formulation discussed later. The following section will cover the Reynolds averaging of the above equation.

3.3.3 Reynolds averaging

Reynolds averaging separates each variable into a mean and fluctuating component, $u = \overline{u}+u'$. Equation 3.11 shows the Reynolds averaged non-conservative momentum equation as outlined by van Oudheusden (2008). For a three-dimensional flow field, this process results in an additional nine Reynolds stress terms that describe the turbulent motion. Physically, the terms on the right hand side represent mean flow convection and turbulent stresses.

$$\left(\delta_{ij}+\frac{\overline{u_i'u_j'}}{RT}\right)\frac{\partial \ln(p/p_\infty)}{\partial x_j} = -\frac{1}{RT}\left(u_j\frac{\partial u_i}{\partial x_j}+\frac{\partial\overline{u_i'u_j'}}{\partial x_j}-\frac{\overline{u_i'u_j'}}{T}\frac{\partial T}{\partial x_j}\right) \tag{3.11}$$

3.3.4 Poisson formulation

Equation 3.11 is written such that the gradient of the pressure term, p/p_∞ is the sole remaining unknown. This term will be solved for using a Poisson equation approach as opposed to one of spatial integration. This is done because a spatial-integration approach would compound the error far away from the point where initial conditions are imposed (van Oudheusden, 2013).

This method takes preference because the quality of the boundary conditions which are to be used cannot be ascertained. Additionally, this helps to account for measurement errors that yield physical inconsistencies in the recorded flow field that otherwise does abide by natural laws (van Oudheusden, 2008).

$$\mathbf{Ap} = \mathbf{f} \quad \rightarrow \quad \begin{bmatrix} 1 + \frac{\overline{u'u'}}{RT} & \frac{\overline{u'v'}}{RT} & \frac{\overline{u'w'}}{RT} \\ \frac{\overline{v'u'}}{RT} & 1 + \frac{\overline{v'v'}}{RT} & \frac{\overline{v'w'}}{RT} \\ \frac{\overline{w'u'}}{RT} & \frac{\overline{w'v'}}{RT} & 1 + \frac{\overline{w'w'}}{RT} \end{bmatrix} \begin{bmatrix} \frac{\partial \ln(p/p_\infty)}{\partial x} \\ \frac{\partial \ln(p/p_\infty)}{\partial y} \\ \frac{\partial \ln(p/p_\infty)}{\partial z} \end{bmatrix} = \begin{bmatrix} f_x \\ f_y \\ f_z \end{bmatrix} \tag{3.12}$$

Expanded, equation 3.11 can be written as three separated linear equations which can then be arranged as a matrix product. The linear system is shown in equation 3.12. The matrix, **f**, follows the system as used by Ragni (2012) and can be seen below in equation 3.13. Spatial variation in density will be quite small as the flow is only mildly compressible, for that reason, the spatial density gradient terms are ommitted due to their relative insignificance. These terms are later reinstated in section 5.4 to demonstrate that they have a negligible impact on the pressure reconstruction.

$$\begin{bmatrix} f_x \\ f_y \\ f_z \end{bmatrix} = -\frac{1}{RT} \begin{bmatrix} \overline{u}\frac{\partial \overline{u}}{\partial x} + \overline{v}\frac{\partial \overline{u}}{\partial y} + \overline{w}\frac{\partial \overline{u}}{\partial z} + \frac{\partial \overline{u'u'}}{\partial x} + \frac{\partial \overline{u'v'}}{\partial y} + \frac{\partial \overline{u'w'}}{\partial z} \\ \overline{u}\frac{\partial \overline{v}}{\partial x} + \overline{v}\frac{\partial \overline{v}}{\partial y} + \overline{w}\frac{\partial \overline{v}}{\partial z} + \frac{\partial \overline{u'v'}}{\partial x} + \frac{\partial \overline{v'v'}}{\partial y} + \frac{\partial \overline{v'w'}}{\partial z} \\ \overline{u}\frac{\partial \overline{w}}{\partial x} + \overline{v}\frac{\partial \overline{w}}{\partial y} + \overline{w}\frac{\partial \overline{w}}{\partial z} + \frac{\partial \overline{u'w'}}{\partial x} + \frac{\partial \overline{v'w'}}{\partial y} + \frac{\partial \overline{w'w'}}{\partial z} \end{bmatrix} \tag{3.13}$$

By taking the divergence of the system of equations, seen in 3.12, the resultant formulation represents a Poisson equation, an elliptical, linear, partial differential equation. The reason for recasting the momentum equation as seen on the left side of equation 3.10 is to allow for the left hand side of equation 3.12 to be written as the following, where **F** forms the solution of the **p** matrix containing pressure gradients, $\mathbf{F} = \nabla \cdot \mathbf{A}^{-1}\mathbf{f}$.

$$\nabla^2 \ln(p/p_\infty) = \frac{\partial^2 (p/p_\infty)}{\partial x^2} + \frac{\partial^2 (p/p_\infty)}{\partial y^2} + \frac{\partial^2 (p/p_\infty)}{\partial z^2} = \mathbf{F} \tag{3.14}$$

Due to the masking of PIV images, the domain upon which the Poisson equation is solved is complex; see the light blue region in Figure 3.4. For this reason, a least-squares spectral element method will be used to solve the Poisson equation based on work by Jeon et al. (2015).

3.3.5 Boundary conditions

Boundary conditions which are used for the solving of the Poisson equation are seen in Figure 3.4. Along the top bound of the field of view, an isentropic flow assumption is valid and therefore, the pressure is known and implemented by a Dirichlet boundary condition; this follows equations 3.5 and 3.6. The isentropic assumption is not valid in the wake of the BFS due to the highly separated flow; therefore, at all other bounds, a Neumann boundary condition is used relating the pressure gradient to the velocity gradient.

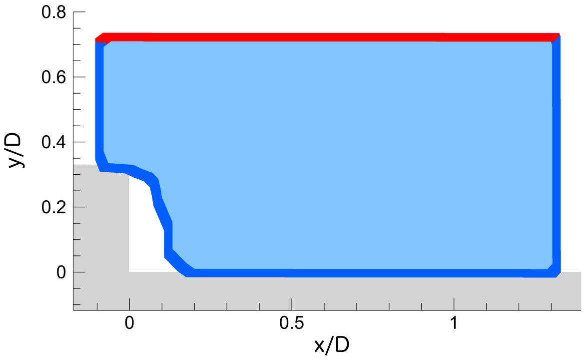

Figure 3.4: Boundary conditions employed for pressure reconstruction; red is type 1 Dirichlet and dark blue is type 2 Neumann.

Chapter 4

Experimental Methods

The following chapter describes the experimental methods used for the two separate experimental campaigns that were conducted. The first experimental campaign served as as validation of the pressure reconstruction technique which would later be used to answer the main research question of this thesis. The second experimental campaign was conducted to determine the effect of nozzle length and exhaust plume presence on the flow topology aft of a transonic launch vehicle. Both of these campaigns made use of the same schlieren and PIV arrangements with slight variations that will be described in this chapter.

4.1 Flow facility

All experiments were conducted in the TST-27 wind tunnel at the High-Speed Aerodynamics laboratory of the Delft University of Technology. The TST-27 is a blowdown transonic and

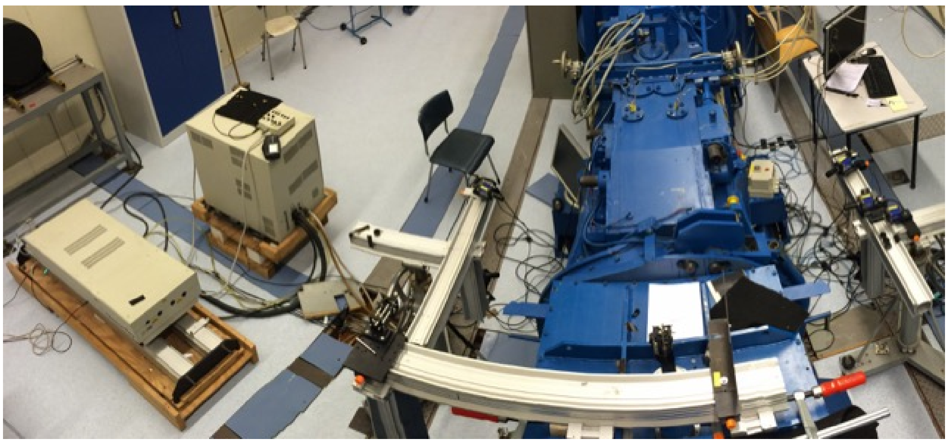

Figure 4.1: A panoramic view of the experimental setup showing most systems

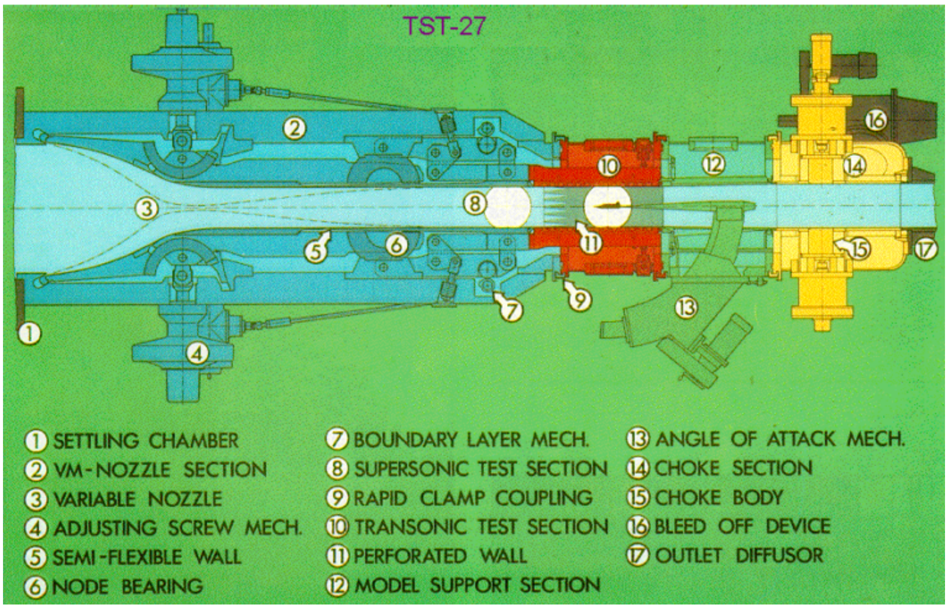

Figure 4.2: A labeled diagram of the TST-27 wind tunnel

supersonic capable wind tunnel with a test section width of 280 mm and a height of 270 mm; the height is variable from 250 mm to 270 mm, dependent upon Mach number. Dry, oil-free air that drives the tunnel is stored in a nearby 300 m^3 vessel that is pressurized to 40 bar. A multi-stage, 230 kW compressor system runs overnight in preparation for a day's worth of testing. Storage vessel pressure is not allowed to decrease below 20 bar and as such, there are approximately 300 seconds of run-time per day; total pressure is variable within 0.05 bar. A vibration test is performed and presented in section 4.5.6 to ensure that operation of the tunnel does not interfere with image recording.

Figure 4.2 shows a cutaway diagram of the TST-27 wind tunnel, though it is shown with the variable angle of attack model section. The freestream Mach number in the test section is variable from 0.5-0.85 and 1.15-4.2 and this is achieved by the variable throat and upper and lower walls in the convergent divergent section of the wind tunnel; the Mach number is variable during a run. For supersonic cases, the flow becomes sonic in the throat and thus increases in velocity through the divergent section. For subsonic cases, the flow remains subsonic at all points due to the larger throat size that never allows the flow to become sonic; this leads to a greater mass flow when compared to a supersonic wind tunnel run. Additionally, for subsonic flows, a variable choke downstream of the test section in the outlet diffuser ensures that small variations in the Mach number are adjusted for. Unit Reynolds number in the flow varies from $3.8 \cdot 10^7\ m^{-1}$ in transonic flows to $1.3 \cdot 10^8\ m^{-1}$ at Mach 4.0.

Optical access to the test section is provided by two, 30 cm diameter, circular quartz glass windows on either side of the wind tunnel; these optical access points are utilized for both the PIV and Schlieren optical techniques used in these experiments. Both the left and the right optical window are visible in Figure 4.3(a) with the sting mounted model visible in the test section. For the PIV measurements, a laser probe was inserted into the tunnel downstream of the model; the laser probe is visible in Figure 4.3(b) with the cutoff plate mounted to facilitate a clear definition of the illuminated field of view. The laser probe was present in the wind tunnel for all experiments but was only used for the PIV measurements which required laser illumination.

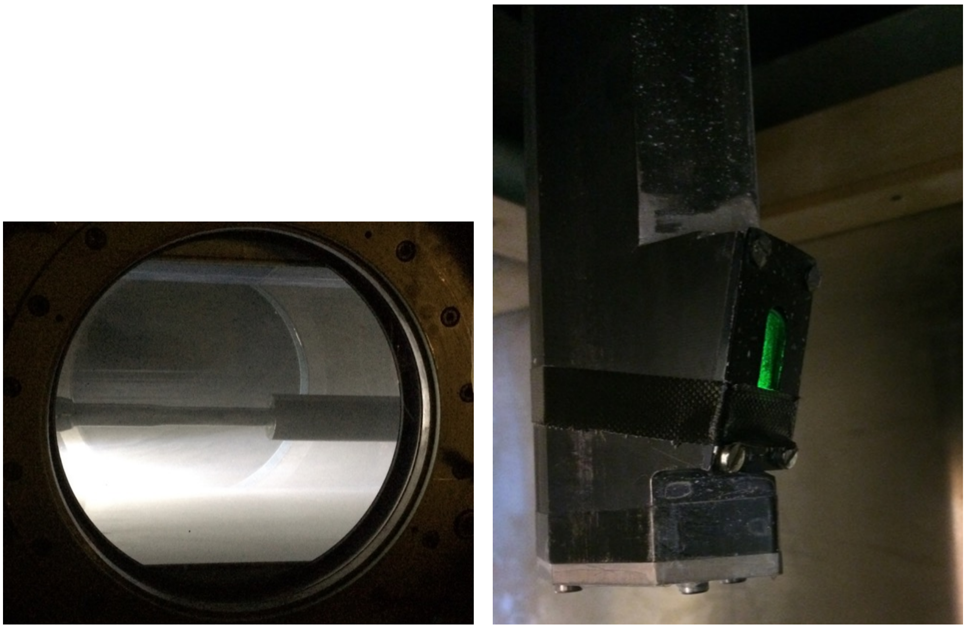

(a) Optical access windows (b) Laser probe with cutoff plate

Figure 4.3: Optical components of the TST-27 wind tunnel

4.1.1 Flow conditions

Due to differences in total pressure, p_0 and Mach number for each measurement set there are variations in the Reynolds number. For all cases, the approximate dynamic viscosity was $\mu \approx 1.79 \cdot 10^{-5}$ kg/m·s, the specific gas constant, $R = 287.058$ J/kg·K, and the ratio of specific heats, $\gamma = 1.4$. Due to the difference in total pressure, there is a difference in the air density in the settling chamber and thus the freestream; the density was found by the ideal gas law. All diameter based Reynolds numbers, Re_D are shown in Table 4.1. These values are rounded and serve as approximations due to variations in temperature, accuracy of settling chamber pressure, etc.

	subsonic exp. camp. I	supersonic exp. camp. I	subsonic exp. camp. II
p_0 [bar]	2.0	2.0	1.5
M_∞	0.7	1.5	0.7
Re_D	$1.3 \cdot 10^6$	$1.2 \cdot 10^6$	$1.0 \cdot 10^6$

Table 4.1: Total pressure, freestream Mach number, and Reynolds number for all measurements

4.2 Validation model

The model used in the first experimental campaign was mounted in the wind tunnel via an afterbody sting. Main body length is 258 mm with a main body diameter of 50 mm. The afterbody has a diameter of 20 mm and gradually increases in diameter beyond the field of view for structural support. A turbulator strip near the nose of the model ensures that a consistent, fully developed turbulent boundary layer is present in the region of interest. The model is painted black to further mitigate reflections from the laser. Figure 4.4 shows a side view of the model with the aforementioned dimensions; the blue 'x' indicates the origin used for PIV and schlieren results.

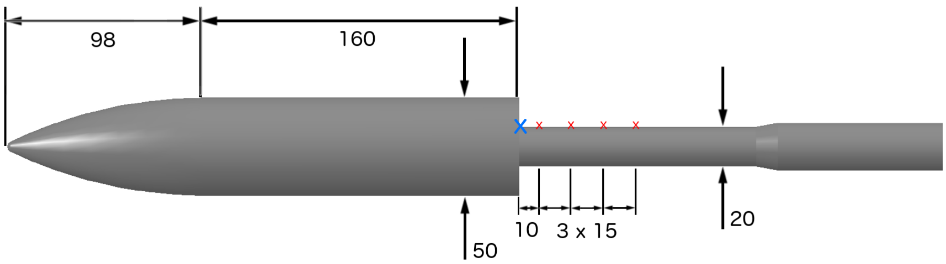

Figure 4.4: The sting mounted wind tunnel model [mm]

Four sting mounted Endevco 8507C-15 pressure transducers are equidistantly spaced 10, 25, 40, and 55 mm from the base; their locations are indicated in Figure 4.4 by the red marks on the afterbody. All transducers, at time of use, were less than one year from last certification and have a sensitivity of approximately 3.2mV/kPa and an acquisition frequency of 10 kHz. Additionally, two steady pressure taps are mounted approximately 30 mm and 70 mm upstream of the base on the main body of the model. Data acquisition for the aforementioned sensors was done using a National Instruments 9237 Half/Full Bridge Analog Input mounted in a cDAQ-9178 USB chassis communicating with LabView software. Pressure measurements were conducted simultaneously with the schlieren visualizations because the sting, including pressure transducers, was covered by black foil during PIV measurements to decrease reflections.

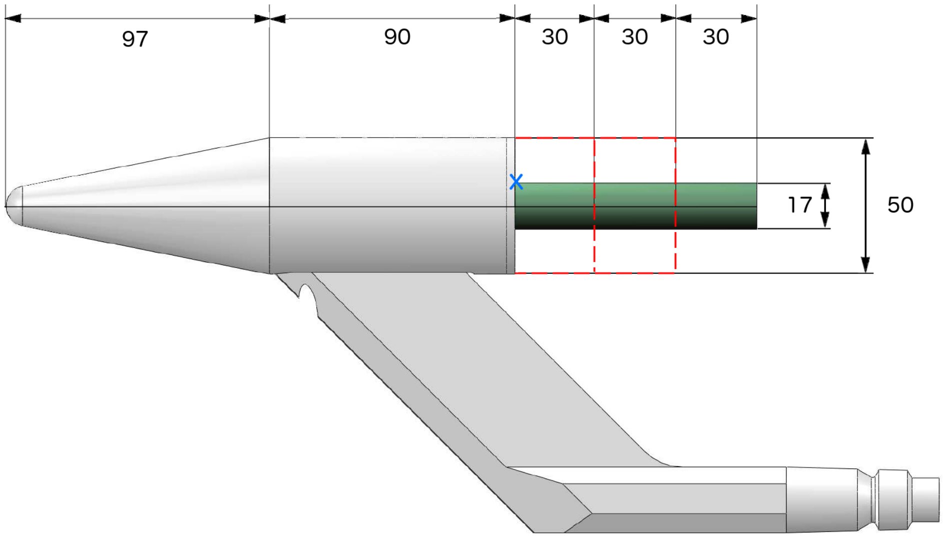

Figure 4.5: Dimensions of modified FESTIP model in side view [mm]

4.3 Cold plume model

The wind tunnel model for the second measurement campaign is a modified FESTIP (Future European Space Transportation Investigations Program) model originally used at the TU Delft by Bannink et al. (1997). Figure 4.5 shows a side view with dimensions of the modified model. Additionally, a blue 'x' indicates the origin of the tomographic PIV measurements and the red lines indicate the spacer positions. The model is also equipped with ten Druck Ltd PDCR-22, 0-15 psi differential pressure transducers along the top of the main body; the number seven transducer is used to determine the freestream Mach number. This model is also equipped with a trip strip on the nose to ensure a fully developed, turbulent boundary layer.

Modifications are made to the model to enable a variation in nozzle length, which is critical to being able to test cases of fluidic, hybrid, and solid reattachment of the shear layer. These modifications includes a new nozzle, spacer rings, and a backplate to be discussed hereafter. In Figure 4.5 the new nozzle is shown in green and the location of the spacer rings are shown in red. All newly fabricated parts are made of stainless steel to match that of the original model; additionally, all parts that are exposed to laser light are spray painted black to mitigate reflections. Lastly, all production work was carried out by the Dienst Elektronische en Mechanische Ontwikkeling (DEMO) of the TU Delft.

4.3.1 Nozzle

The nozzle is adapted from the original version drawn by Ing. F.J. Donker Duyvis and as such is designed to be an extension to 90 mm total 'exposed' length. The nozzle maintains the same area ratio, $A_{\text{exit}}/A^* = 11.67$ in order to ensure the same exit Mach number, $M_{\text{exit}} \approx 4.1$.

To facilitate the extension, the settling chamber diameter had to be decreased from 15 mm to 10 mm to ensure the presence of adequate material to handle the high pressure. A technical drawing of the nozzle can be seen in Appendix A.1. Settling chamber pressure is set to 100 bar and is regulated via a control unit which receives feedback from the pitot tube mounted within the nozzle as seen in Figure 4.6(a).

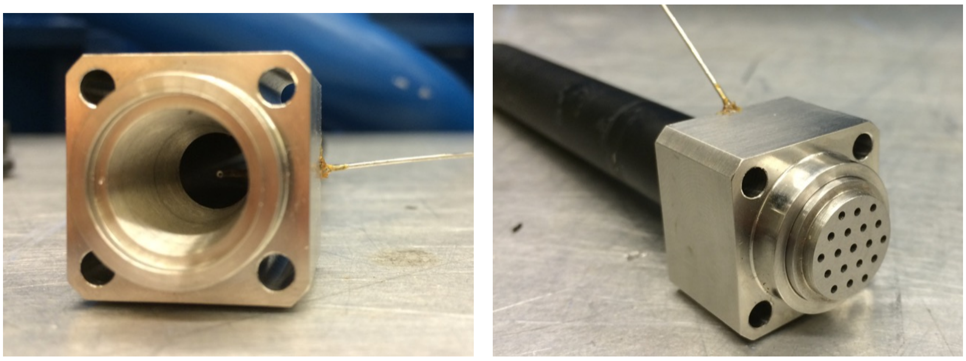

(a) Pitot tube mounted inside nozzle (b) Vorticy reduction plate installed

Figure 4.6: Modified nozzle showing pitot tube and perforated plate

A small perforated plate, seen in Figure 4.6(b), is meant to reduce flow fluctuations in the settling chamber. Before the plate, total pressure is approximately 200 bar and after the plate the total pressure is near the set value of 100 bar. Mating of the nozzle to the model is done using four M4 Allen head bolts in the same manner as the original. Technical drawings for the nozzle can be seen in Appendix A.1.

4.3.2 Backplate

A new backplate is also designed to allow for the attachment of a spacer ring. This new backplate is a modified version of the original design by Ing. F.J. Donker Duyvis. To facilitate the attachment of spacer rings, a new backplate is tapped for two M4 threads; the M4 bolts that attach to these threads run through the spacer ring and secure them to the model. To ensure a better fit. the backplate is also fitted with an o-ring at the interface with the nozzle. The backplate is mated to the model using six M2 flat head bolts in the same manner as the original; with a diameter of 50 mm, equal to that of the model main body diameter, the backplate attaches securely to the rear of the model. Figure 4.7(a) shows the aforementioned features on the backplate. A technical drawing of the backplate can be seen in Appendix A.2.

4.3.3 Spacer rings

Three separate spacer rings were made in order to change the effective nozzle length; one spacer ring is 30 mm in thickness and the remaining two are 15 mm in thickness. Two

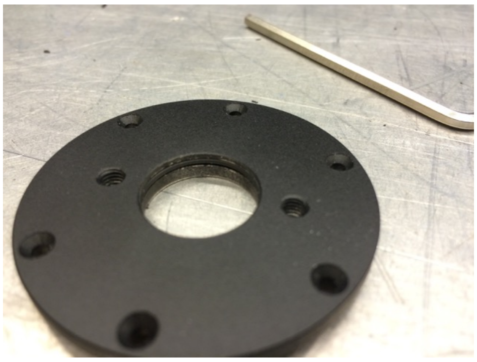

(a) Painted backplate showing M4 threads and M2 clearance holes

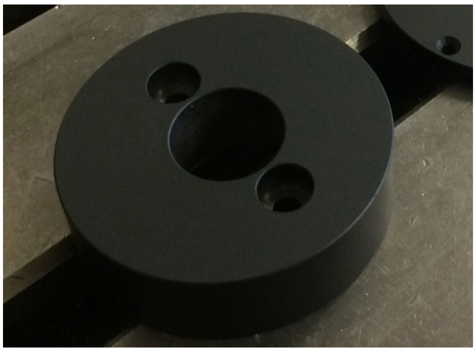

(b) 15 mm spacer ring showing M4 clearance holes

Figure 4.7: Backplate and 15 mm spacer ring

spacers of each 30 mm are required to achieve the desired L/D values of 0.6, 1.2, and 1.8 as shown in Figure 4.5. By separating one 30 mm spacer into two, individual 15 mm spacers the same model setup can also be used to investigate the additional L/D values of 0.9 and 1.5 which may be of interest to other researchers studying different Mach numbers; these extraneous L/D values are not shown in Figure 4.5.

4.3.4 Compressed air supply

The settling chamber pressure measurements are made via a 0.8 mm steel pitot tube ported to a Druck Limited PDCR910 (Ser. Num. 933532) strain type pressure transducer connected to the local HP1000 computer. A calibration was performed by technical staff before measurements were made. Total jet pressure is set via a FESTIP control unit as seen in Figure 4.8(a). Compressed air is supplied by four 50 liter tanks each filled to a pressure of 300 bar; two of these tanks are visible in Figure 4.8(b). The tanks are refilled after each run using a Bauer mini-verticus 3 compressor.

(a) The FESTIP control panel

(b) Two of four compressed air bottles

Figure 4.8: Control and supply of compressed air for cold plume

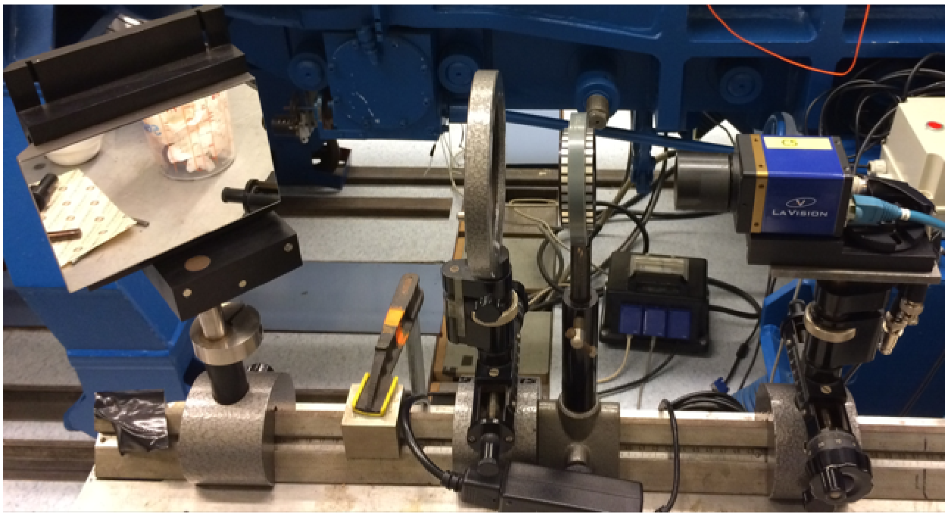

Figure 4.9: The Schlieren knife, optics, and camera

4.4 Schlieren imaging

The schlieren setup uses a z-type configuration which allows for a collimated beam of light, perpendicular to the flow, to cross through the test section. The beam is formed by two large, concave mirrors ($f = 3.5$ m). A short-arc Xenon lamp is used as the illumination source because it provides a very high luminance leading to a 'point like' light source. This consists of an OSRAM XBO W/1 150W Xenon bulb placed in a protective housing. A Siemens DC power supply provides the necessary 7.5A at approximately 20V to drive the lamp. This illumination source is continuous and as such, the necessary image intensity is controlled through the shutter of the camera.

The camera for the schlieren setup is of the same make and model as for the PIV setup; a LaVision branded Imperx B1610M Bobcat CCD camera. For more information regarding the camera itself, see section 4.5.1. Figure 4.9 shows the setup mounted on a rail that featured a mirror, the schlieren knife, a $f/200$ lens, and the camera with a barrel housing to protect the sensor. Light impinged directly on the sensor which was exposed to the air. Relative to the typical flow time scales, the shutter speed of the camera is long.

All schlieren images were averaged over approximately 200+ snapshots resulting in a mean flow field image. Two schlieren knife orientations were used, horizontal and vertical. The horizontal knife was used to visualize vertical gradients and the vertical knife was used to visualize horizontal gradients; this occurs as a result of vertical air density gradients deflecting light vertically to strike a horizontal cutoff, for example. This allows for the capturing of specific features, the horizontal gradient is best suited for shockwaves and the vertical gradient for boundary layers.

4.5 PIV arrangements

The PIV arrangements for both experimental campaigns will be discussed in the following section. There are many similarities in configuration between the two experimental campaigns but all specifics will be outlined and any differences will be noted.

4.5.1 Cameras and optics

All measurements, both Schlieren and PIV, made use of LaVision branded Imperx B1610M Bobcat CCD camera of the CoaXPress variation. As the name implies, the cameras are of the Charged Coupled Device (CCD) type and feature a maximum resolution of 1628 by 1236 pixels with a pixel size of 4.40 μm. The shortest possible interframe time is 200 ns and the lowest shutter speed is 1 μs. All cameras are set to output 12-bit monochrome images via a CAT-5 ethernet cable to a PC nearby. Triggering of the cameras occurs via a LaVision external PTU which is connected via RG-56 cable and BNC connectors. Power at 12VDC, 1.5A is provided by individual Imperx Lynx Gig-E AC adapters; the trigger mechanism and power supply input are combined into one hirose connector and attached to the rear of each camera. Figures 4.10(a) and 4.10(b) show a Bobcat camera unit with 75 mm Tamron optic attached.

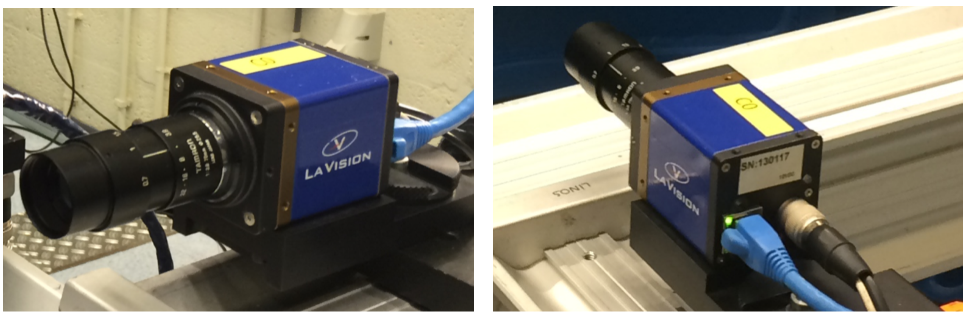

(a) Front of Bobcat camera (b) Rear of Bobcat camera

Figure 4.10: Imperx B1610M Bobcat CCD camera with 75 mm Tamron optic

4.5.2 Laser illumination

Illumination of the field of view is provided by a SpectraPhysics Quanta-Ray Neodymium-doped yttrium aluminium garnet (Nd:YAG) laser as seen in Figure 4.11(a). The laser light has a wavelength of 532 nm, which also yields the optimal relative response for the Bobcat monochrome cameras. For all runs the laser was set to full power yielding 400 mJ per pulse. Pulse duration was 7 ns and pulse separation time was 2.5 μs for all subsonic cases at $M = 0.7$ and 1.5 μs for all supersonic cases. The laser unit was positioned beside the wind tunnel and light was guided to the test section by three mirrors making three right angled turns as seen in Figure 4.11(b). Finally, the laser light is trimmed using a knife-edge plate over the probe outlet as seen in Figure 4.3(b) (Donker Duyvis, 2005). All triggering of the laser was controlled by the external PTU and DaVis 8.3.1.

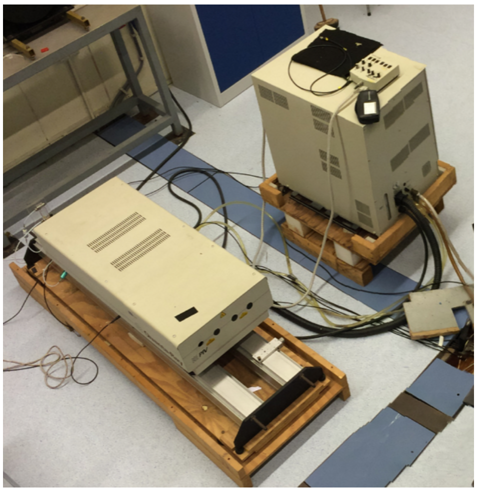

(a) Laser and control unit

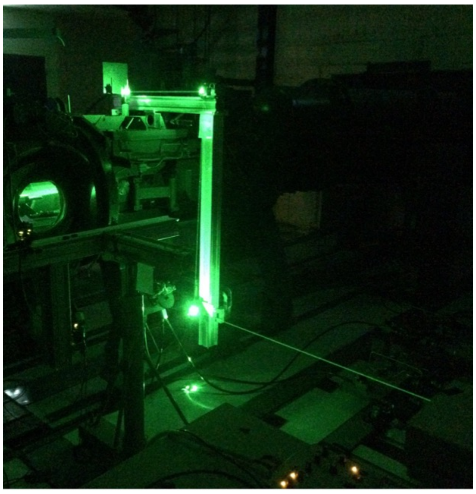

(b) Pulse path visualization

Figure 4.11: SpectraPhysics Nd:YAG laser

Practically, this resulted in an illuminated volume, the size of which, was on the order of a modern smartphone. This is represented by the light intensity profiles seen in Figure 4.12, which were averaged over 250 snapshots. The first experimental campaign featured a laser sheet thickness of approximately 5 mm, as seen in Figure 4.12(a), which was increased to 8 mm for the second experimental campaign, as seen in Figure 4.12(b). This was done in an effort to resolve more of the flow in the out-of-plane direction upon noting the possibility after the first measurement campaign.

4.5.3 Seeding

Seeding was injected into the settling chamber of the TST-27 using a PIVTEC atomizing DEHS seeder as seen in Figure 4.13(a). Bis(2-ethylhexyl) sebacate (DEHS) is compared to TiO_2 by Ragni et al. (2011) in which it is found to have similar performance in supersonic flows. The DEHS oil used in the experiments is produced by Merck Schuchardt OHG and has a nominal particle diameter of 1 μm when injected with the PIVTEC atomizing seeder. Particle response time, τ_p is approximately 2 μs (Ragni et al., 2011). This is comparable to dehydrated TiO_2 particles and has the added benefit of decreased health hazards during handling (C.D.C., 2011).

The flow was seeded using a rake in the settling chamber of the TST-27. Injection pressure of the seeder was consistently 1 bar above the total pressure in the settling chamber. In an

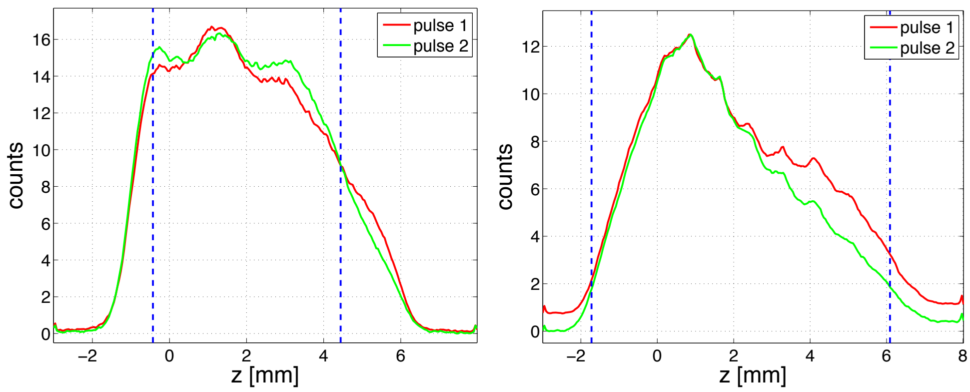

(a) Experimental campaign I

(b) Experimental campaign II

Figure 4.12: Z-profiles of laser volume

effort to achieve approximately 0.005 particles per pixel (ppv) in the resulting measurements, 6-15 injectors were activated on the seeder; this was done using the PIVPART-45 control unit seen in Figure 4.13(b). The ppv values are listed in the experimental matrices for each case; the values are calculated per voxel of 40 pixels per side and are averaged over all images acquired.

4.5.4 PIV camera arrangement

All cameras are mounted on stands that are firmly placed on the hard points of the tunnel hall floor. One camera stand is found on each side of the wind tunnel. For PIV measurements each camera was fitted with a 75 mm Tamron lens. Those cameras that do not perpendicularly face the field of view are fitted with a Scheimpflug adapter to rotate the focal plane such that it is parallel with the field of view. All CCD cameras, except camera 1, are placed at a 45° angle with respect to the x-y plane of the field of view, this yields a system aperture angle of 90° in a cross-like setup; per Scarano (2013a) this results in a near optimal tomographic reconstruction quality factor, Q. Figure 4.15(a) shows a top view and Figure 4.15(b) a rear view of the arrangement. This approach was used for both experimental campaigns.

Specific PIV related details for experimental campaign I are presented in Table 4.2. The column labeled ‘distance’ indicates the distance to the field of view for the camera placed at a right angle to said field of view. Additionally, the resulting magnification factor, M, the focal depth, and the resolution along with the freestream particle displacement are presented. Figure 4.14(a) illustrates the location of the field of view with respect to the model. Also shown in blue is the field of view for a planar 2C camera that was placed to view slightly upstream of the point of separation. This was done to study the in-flow boundary layer before separation and the results of this study are presented in section 5.4.

Following the same format as experimental campaign I, the PIV specifics for experimental

(a) PIVTEC atomizer (b) The PIVPART 45 control unit

Figure 4.13: Seeding atomizer and control unit

Settings						**Optical results**		**dx$_\infty$**	
Mach	$f_\#$	f [mm]	dt [μs]	dist. [mm]	M	focal depth [mm]	Res. [pix/mm]	[mm]	[pix]
0.7	5.6	75	2.5	816	0.1012	9.64	23.0	0.625	14.4
1.5			1.5					0.675	15.5

Table 4.2: PIV arrangement specifics for experimental campaign I

campaign II are presented in Table 4.3. During experimental campaign II, the camera arrangement was made to slide such that the field of view remained centered on the separated base region; for this reason, Table 4.3 shows slight variations in PIV specifics as the system was moved and recalibrated for each case. The resultant change in the location of the field of view is illustrated in Figure 4.14(b).

4.5.5 Image acquisition

A geometrical calibration (pin-hole model) using a three-dimensional LaVision Type 7 calibration plate was first completed for all arrangements. Each major measurement run of 250 or 500 recordings was preceded with a run of 50 recordings and reduced seeding density for the purposes of self-calibration. An iterative tomographic self-calibration routine was conducted (third order polynomial model) until all cameras achieved a RMS of fit below 0.2 pixels; most were significantly below that value around 0.1 pixels.

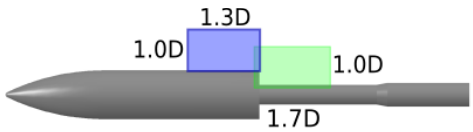

(a) Experimental campaign I

(b) Experimental campaign II

Figure 4.14: Fields of view for experimental campaigns I and II

Settings				Optical results				dx_∞	
Config.	$f_\#$	f [mm]	dt [μs]	dist. [mm]	M	focal depth [mm]	Res. [pix/mm]	[mm]	[pix]
0.6	5.6	75	2.5	794	0.1043	9.12	23.7	0.625	14.8
1.2				798	0.1036	9.22	23.6	0.625	14.7
1.8				794	0.1043	9.12	23.7	0.625	14.8

Table 4.3: PIV arrangement specifics for experimental campaign II

After a major measurement run was completed, an additional run of 50 recordings with reduced seeding was conducted for the purposes of verifying that the self-calibration was maintained over the course of the extended run. In tables 4.4 through 4.7 this is seen by the rightmost N pairs column. The leftmost column indicates the run number as it appears in the TST-27 logbook signed by the technician prior to every run.

Measurement runs during experimental campaign II were done in this fashion because it was estimated that the compressed air tanks would only be able to sustain the set NPR for 30.5 seconds. As a result of this, measurement runs occurred in 'volleys' which are indicated by the horizontal lines through Tables 4.5, 4.6, and 4.7. This was to maximize measurement efficiency by allowing the compressed air tanks to refill in between cold plume runs. The estimate based the total amount of air in the tanks on the ideal gas law; when the tanks are full they are pressurized to 300 bar and when empty are reduced to 100 bar. It is further assumed that the nozzle, which is the smallest geometric diameter in the entire system, is choked, thus achieving the maximum possible mass flow.

4.5.6 Wind Tunnel Vibration Test

A 'vibration test' was performed on the TST-27 to determine whether or not operation of the tunnel was interfering with the accurate recording of images. This was of concern because the CCD cameras were calibrated to sub-pixel accuracy which could be disturbed by the

WT			Seeding			Acquisition	
Run #	Mach	p_0 [bar]	Injectors	p [bar]	ppv	freq. [Hz]	N pairs
153	0.7	2.0	6	3.0	0.0047	10	50
154			15		0.0084		500
155			6		0.0049		50
156	1.5	2.0	6	3.0	0.0059	10	50
157			15		0.0096		500
158			6		0.0057		50

Table 4.4: Experimental matrix for experimental campaign I

WT			Model		Seeding			Acquisition	
Run #	Mach	p_0 [bar]	Config.	p_{jet} [bar]	Injectors	p [bar]	ppv	freq. [Hz]	N pairs
200	0.7	1.5	1.8	off	6	2.5	0.0084	10	50
201				100	12		0.0128		250
202				off	6		0.0087		50
203				off	12		0.0113		250
204				off	12		0.0117		250
209	0.7	1.5	1.8	off	6	2.5	0.0096	10	50
210				100	12		0.0134		250
211				off	6		0.0084		50

Table 4.5: Experimental matrix for L/D = 1.8 case of experimental campaign II

WT			Model		Seeding			Acquisition	
Run #	Mach	p_0 [bar]	Config.	p_{jet} [bar]	Injectors	p [bar]	ppv	freq. [Hz]	N pairs
213	0.7	1.5	0.6	off	6	2.5	0.0089	10	50
214				100	9		0.0140		250
215				off	9		0.0137		250
216				off	6		0.0090		50
217	0.7	1.5	0.6	off	6	2.5	0.0087	10	50
218				100	9		0.0110		250
219				off	9		0.0115		250
220				off	6		0.0088		50

Table 4.6: Experimental matrix for L/D = 0.6 case of experimental campaign II

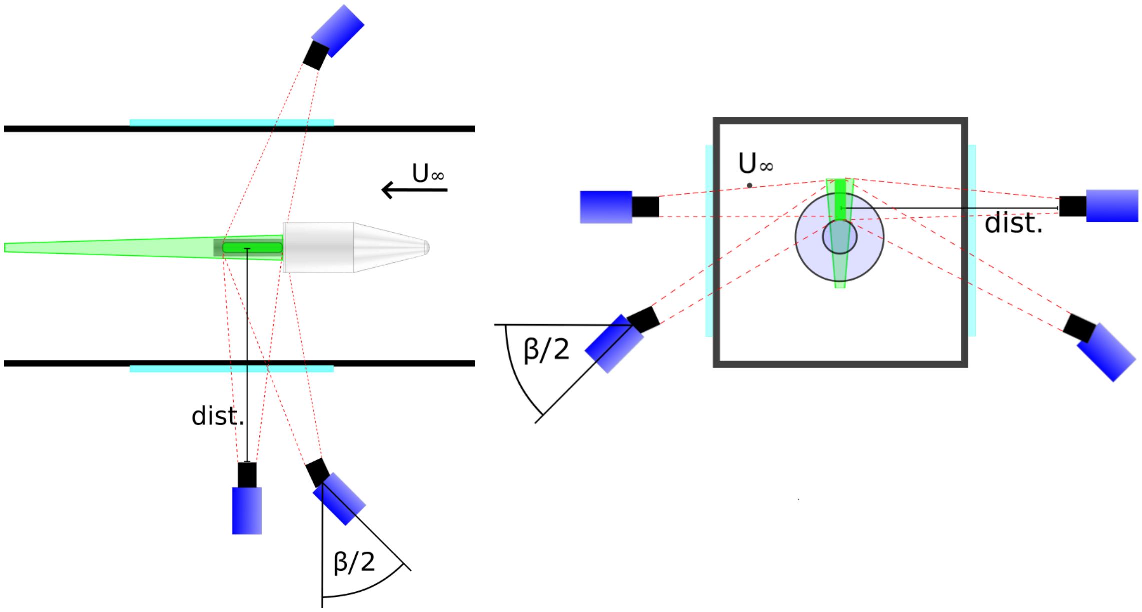

(a) Top view (b) Rear view

Figure 4.15: PIV arrangement for both experimental campaigns

slightest of motion. To ascertain whether or not this would be an issue, 10 images were taken from four of the tomographic, thus excluding the camera placed orthogonally to the FOV. Figure 4.5.6 shows the field of view of each camera subdivided into six separated domains over which particle groupings are identified; this is analogous to the self-calibartion image made by the DaVis software. Upon performing the test, the results do not show correlated motion in the imaged particles. If there were to be vibration, the excepted result would be correlated displacements for the cameras. Additionally, vibrations would not be equal among all cameras and some would display a differing displacement between the individual 'clouds'.

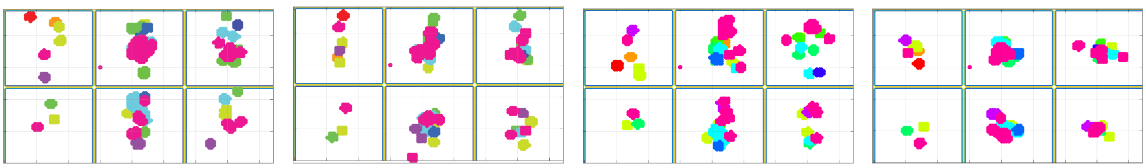

(a) cam 1 (b) cam 2 (c) cam 3 (d) cam 4

Figure 4.16: Vibration test results for TST-27 at Mach 0.7

*_

	WT		Model		Seeding			Acquisition	
Run #	Mach	p_0 [bar]	Config.	p_{jet} [bar]	Injectors	p [bar]	ppv	freq. [Hz]	N pairs
221	0.7	1.5	1.2	off	6	2.5	0.0098	10	50
222				100	9		0.0154		250
223				off	9		0.0145		250
224				off	6		0.011		50
225	0.7	1.5	1.2	off	6	2.5	0.0121	10	50
226				100	9		0.0148		250
227				off	9		0.0172		250
228				off	6		0.0132		50

Table 4.7: Experimental matrix for L/D = 1.2 case of experimental campaign II

4.5.7 Image processing

LaVision DaVis 8.3.1 was used for all processing work. The following section explains the processing steps in the approximate order in which they were performed.

Geometric mask First, portions of the model, which are visible in the recorded images, are geometrically masked to mitigate reflections. Subsequently, the working mask is saved and added from disk in additional cases; this is done to ensure that the same geometric mask is applied to each image set. For the creation of the initial geometric mask the `masking functions > add geometric mask` option is used and `masking functions > add mask from disk` for adding the mask from disk.

Algorithmic mask Recordings which featured the operational cold plume had an algorithmic mask applied during processing. Due to condensation in the cold plume, liquid oxygen caused very high reflections which were at the 4096 count, upper-limit of the 12-bit CCD sensor. To mask these regions of high intensity over a variable area, an algorithmic mask was applied to any pixel over 4000 counts by the `masking functions > add algorithmic mask` option. Where the algorithmic mask was used, a requirement of 100 valid pixels out of 500 vector fields was imposed.

Image preprocessing and non-linear filtering As a preprocessing step, each image is normalized with a local average smoothed over a 6 pixel radius. The local average is computed separately for each image. This step is found in the `tomographic PIV > image preprocessing` menu. Thereafter, to further increase the signal-to-noise ratio, a sliding average of 6 by 6 pixels is subtracted by the `non-linear filter > subtract sliding average` option.

Step	Size [voxel]	Overlap [%]	Peak search radius [voxel]	Volume binning	Passes
1	96	75	8	8x8x8	1
2	64		4	4x4x4	1
3	48		2	2x2x2	1
4	40		2	no	2
5	32		1	no	3

Table 4.8: Tomographic correlation window details

Volume reconstruction Tomographic volume reconstruction was done by means of a fast multiplicative algebraic reconstruction technique (fastMART) using all 5 cameras. The process uses an MLOS initialization, 3 CSMART iterations, 20 SMART iterations, and 22 smoothing iterations of 0.3 strength. Each voxel must be visible by a minimum of 3 cameras to be considered valid. These options are found under `tomographic PIV > volume reconstruction: fast MART`.

Volume correlation The tomographic volume correlation is performed in 5 steps, each using a 1:1 Gaussian-elliptical window with a 75% overlap; Gaussian window weighting is outlined by Kähler and Scholz (2006). Voxel size was gradually reduced from 96 to 32 voxels with a decreasing peak search radius; volume binning was performed for the first 3 steps, each consisting of 1 pass. For the final 2 steps, volume binning was not performed and the steps consisted of 2 and 3 passes, respectively. Each step required a 50% valid voxel per window. Table 4.8 shows the details for each step and window. This process is listed under `tomographic PIV > volume correlation (direct correlation)`.

For multi-pass steps, such as 4 and 5, multi-pass postprocessing is used for universal outlier detection, removal, and insertion. The operation uses the '2 x remove & insert' mode with an epsilon value of 0.1 pixels. Outlier removal threshold is set to 2 and insertion threshold is set to 3. Vectors that are inserted are based on a 5x5x5 interpolation of their nearest neighbors, requiring at minimum 6 valid vectors for a replacement. Lastly, a single 3x3x3 Gaussian smoothing operation is performed.

Processing of spurious vectors, referred to as outliers, is based on work by Westerweel and Scarano (2005). The aforementioned five steps shown in Table 4.8 are performed in an effort to increase the accuracy and reduce the computational costs of the reconstruction. Gaussian-elliptical windows reduce the number of outliers and better capture vertical velocity gradients by deforming into flat, elongated ellipses. Earlier steps with larger window sizes are used to 'predict' the rough particle shift which is then used to 'correct' the refined window of the following step; volume binning reduces the computational costs of this iterative process. Reductions in peak search radius are also done to reduce computational costs as the particle shifts become more precise.

Vector postprocessing Universal outlier detection, removal, and insertion is again used for the three-dimensional vector postprocessing after the tomographic volume correlation. A

case	# Vectors streamwise	radial	out-of-plane
exp. camp. I	140	244	15
$L/D = 0.6$	135	206	24
$L/D = 1.2$	117	205	24
$L/D = 1.8$	117	209	24

Table 4.9: Number of vectors per component direction for each experimental case

'2 x remove & insert' mode is used with an epsilon value of 0.1 pixels. The vector threshold is set to 2 and the insert threshold to 3. Insertion of new vectors is based on a 5x5x5 interpolation of nearest neighbors requiring a minimum of 6 valid vectors for successful operation. Lastly, a fill up all operation is used to replace missing vectors.

Resulting vector fields Table 4.9 shows the number of vectors per component direction for each experimental case. For the subsonic and supersonic cases of the first experimental campaign, this results in the same number of vectors because there are no changes to the PIV system. The increase in width of the measurement volume for the second experimental campaign is evident in the rise in the number of vectors in the out-of-plane direction. Slight variation in the three PIV arrangements of the second experimental campaign are due to the movement and recalibration of the system for each nozzle length case.

4.6 PIV uncertainty analysis

Error is defined as the difference between the true value and the measured value; a set of measurements is more accurate when this difference is minimal. Because the aforementioned true value is unknown, the uncertainty is quantified as an estimation of the error (Stern et al., 1999). The two main sources of uncertainty for the performed experiment are the limited ensemble size and those inherent in the PIV measurement technique; these two sources of uncertainty will be discussed in the present section. All uncertainty values for each experimental case are presented at the end of this section in Tables 4.10 through 4.14.

4.6.1 Ensemble size uncertainty

Recorded images are not correlated in time; based on the freestream particle displacement and the time step, particles move approximately 2.6 meters in between each image pair. The particles of one flow field snapshot are far removed from the field of view by the time of the following snapshot. Though the flowfield snapshots show instances of the unsteady motions of the shear layer, it is not possible to temporally resolve these features in the present experiment. As such, the mean flow field is studied as an ensemble average of all recorded images. Though an impossible and infinite number of images would be required to exactly match the theoretical mean flow field, an acceptable result can be gathered with several hundred images. The present section aims to quantify the mean flow field uncertainty which stems from the finite ensemble size.

The ensemble size uncertainty analysis follows the work by Benedict and Gould (1996) which is also discussed in the PhD theses by Humble (2009) and Sun (2014). Generally, the normalized uncertainty, ϵ is quantified by equation 4.1 when modelling the measurements as a Gaussian process. This model will be applied to the mean velocity components, the RMS of their fluctuations, and the Reynolds shear stress. All uncertainties are normalized by the freestream velocity, U_∞ and presented as a percentage thereof. Additionally, the uncertainties are quantified in voxels relative to the PIV system.

$$\epsilon = \frac{\sigma}{\mu\sqrt{N}} \tag{4.1}$$

For the streamwise, radial, and out-of-plane velocity components, the normalized uncertainty is seen in equation 4.2. The equations are defined by the RMS of the velocity fluctuations and the ensemble size. As such, the uncertainty of the mean flow field will be higher in regions that have higher velocity fluctuations, such as the reattachment location.

$$\epsilon_{\overline{u}} = \frac{\sqrt{\overline{u'^2}}}{\sqrt{N}} \qquad \epsilon_{\overline{v}} = \frac{\sqrt{\overline{v'^2}}}{\sqrt{N}} \qquad \epsilon_{\overline{w}} = \frac{\sqrt{\overline{w'^2}}}{\sqrt{N}} \tag{4.2}$$

The normalized uncertainty of the RMS of the streamwise, radial, and out-of-plane velocity components is seen in equation 4.3

$$\epsilon_{\langle u' \rangle} = \frac{\sqrt{\overline{u'^2}}}{\sqrt{2N}} \qquad \epsilon_{\langle v' \rangle} = \frac{\sqrt{\overline{v'^2}}}{\sqrt{2N}} \qquad \epsilon_{\langle w' \rangle} = \frac{\sqrt{\overline{w'^2}}}{\sqrt{2N}} \tag{4.3}$$

The normalized uncertainty of the Reynolds stress term is seen in equation 4.4. The term, $R_{\overline{u'v'}}$ is the correlation coefficient.

$$\epsilon_{\overline{u'v'}} = \frac{\sqrt{1 + R^2_{\overline{u'v'}}}\sqrt{\overline{u'^2}}\sqrt{\overline{v'^2}}}{\sqrt{N}} \quad \text{where} \quad R_{\overline{u'v'}} = \frac{\overline{u'v'}}{\sqrt{\overline{u'^2}}\sqrt{\overline{v'^2}}} \tag{4.4}$$

Visualization of convergence

Figure 4.17 shows the convergence to the mean flow field for the mean streamwise velocity, $\overline{u}/U_\infty$, the Reynolds stress, $\overline{u'v'}/U_\infty^2$, and the turbulence intensity, $\overline{u'}/U_\infty$. The convergence is visualized by comparing the difference between mean flow fields comprised of n and $n+1$ snapshots for all n up to $n = 500$. It can be seen in Figure 4.17 that the mean velocity, $\overline{u}/U_\infty$ convergence very quickly compared to both the turbulence intensity and the Reynolds stress. Adequate convergence of the Reynolds stress, $\overline{u'v'}/U_\infty^2$ requires significantly more samples than the mean velocity, which is consistent with findings by Hain et al. (2016). This illustration is included to provide insight into the higher ensemble size uncertainty for the Reynolds stress term.

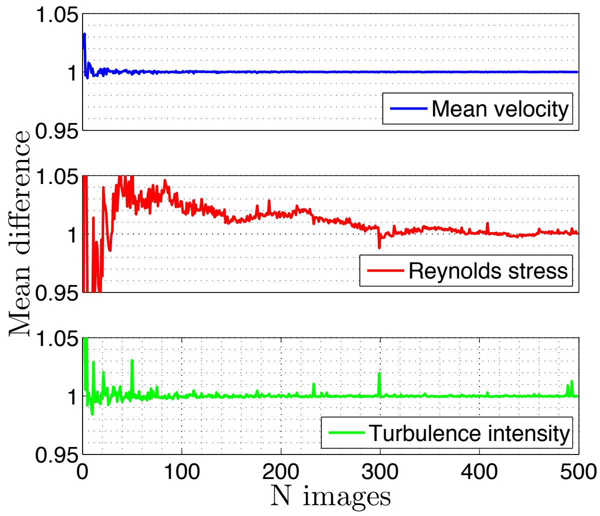

Figure 4.17: Convergence of mean flow field variables

4.6.2 PIV measurement uncertainty

A second major source of uncertainty comes from the PIV measurement technique itself. The images made by the system record the motion of the particles; as the particles do not follow the flow exactly, there is discrepancy between that which is recorded and the fluid motion. Additionally, during calculation of the vector fields, certain uncertainties are produced. Lastly, due to a finite spatial resolution, the results are only able to resolve flow features down to a certain scale. These three sources of uncertainty will be discussed in the present section.

Uncertainty due to particle slip

Seeding particles that are imaged in the flow have their own mass and inertia. For this reason, the seeding particles do not instantly and exactly follow the flow which is to be studied. As a result of this, an uncertainty arises between that which is measured and the flow itself. This uncertainty is quantified as the particle slip velocity, u_{slip} which is defined as the product of the particle response time, τ_p and the particle acceleration, a_p as seen in equation 4.5 (Sun, 2014).

$$u_{\text{slip}} \approx \tau_p \cdot a_p \tag{4.5}$$

As stated in section 4.5.3, the DEHS particles used in the present experiment have a particle response time, $\tau_p \approx 2\ \mu s$ (Ragni et al., 2011). When the density of the particles is much greater than that of air, the governing equations for the particle motion can be reduced to equation 4.6 (Melling (1997), Sun (2014)). The general equation, which is not presented herein, is stated by Melling (1997) and the simplification for DEHS particles in particular is made by Sun (2014). Equation 4.6 shows that particle acceleration is a function of the difference between particle and fluid velocity, u_p and u_f, respectively, divided by the response time of the particle, τ_p.

$$a_p = \frac{du_p}{dt} = \frac{u_p - u_f}{\tau_p} \tag{4.6}$$

For regions of steady flow, equation 4.6 can be simplified to 4.7 according to Ragni (2012).

$$a_p = \vec{U} \cdot \nabla \vec{U} \tag{4.7}$$

By substituting equation 4.7 into equation 4.5, the resulting equation for particle slip velocity is seen in equation 4.8. Note that the estimation for particle slip velocity seen below is only valid for regions without strong vortices. As such, it will be used as an estimate for areas outside of the recirculation region.

$$u_{\text{slip}} \approx \tau_p \cdot \left(\vec{U} \cdot \nabla \vec{U} \right) \tag{4.8}$$

In the recirculation region, estimations for the particle slip velocity will be based on the centrifugal acceleration term as this is the dominant force driving particles outward within said region (Sun, 2014). Equation 4.9 shows the approximate particle acceleration for those regions where strong vortical motion is present. According to Sun (2014), the magnitude of the velocity, $\vec{U}$ is estimated by the difference between freestream velocity, U_∞ and the convective shear layer velocity, $U_{\text{convective}}$. Additionally, the vortex radius, r is of the same order as the BFS step height, h and therefore is estimated as such.

$$a_p \approx \frac{\mid \vec{U}^2 \mid}{r} \tag{4.9}$$

The resultant particle slip velocity in the recirculation region is seen below in equation 4.10.

$$u_{\text{slip}} \approx \tau_p \cdot \left(\frac{\mid \vec{U}^2 \mid}{r} \right) \tag{4.10}$$

Uncertainty due to cross-correlation

For each instantaneous vector field representation of the flow, there is an associated uncertainty that arises due to the cross-correlation operation. The associated instantaneous velocity uncertainty is estimated by equation 4.11 (Humble, 2009). Therein, κ is the PIV image resolution in pix/mm and Δt is the associated pulse separation time of the PIV system. The ϵ_{cc} term is the uncertainty of the cross-correlation operation, which is conservatively estimated by Humble (2009) to be 0.2 voxels for tomographic PIV.

$$\epsilon_u = \frac{\epsilon_{\text{cc}}}{\kappa \Delta t} \tag{4.11}$$

The cross-correlation uncertainty, $\epsilon_{\text{cc}} = 0.2$ was also found to be conservative by Lynch and Scarano (2014), having performed a zero-time-delay test. Additionally, Elsinga et al. (2006) highlights that $\epsilon_{\text{cc}} = 0.2$ is a suitable uncertainty factor for cross-correlation of tomographic PIV measurements.

Uncertainty due to spatial resolution

Table 4.8 shows that the final window size for all PIV processing was 32 voxels. Due to an inherently finite window size, certain structures and motions within the flow, of a particular spatial frequency, are not resolved due to undersampling. All PIV experiments suffer an innate uncertainty as a result of this. Due to the limited spatial resolution, a ratio is defined by the minimum window size, WS, versus the spatial wavelength of the relevant flow feature, λ; the ratio is defined as the normalized window size, $l^* = \mathrm{WS}/\lambda$ and can be seen in the cardinal sinc function in equation 4.12 (Schrijer and Scarano, 2008).

$$\frac{u}{u_0} = \mathrm{sinc}\left(\frac{\mathrm{WS}}{\lambda}\right) \tag{4.12}$$

By the nature of the cardinal sinc function, if the window size, WS were to be smaller, the numerator in the function would be larger; this would lead to a decreased relative uncertainty in velocity. It follows then that an increase in spatial resolution allows for the capturing of smaller flow features. Therefore, as the normalized window size, l^* decreases toward zero, the relative velocity uncertainty decreases because the window size is able to adequately resolve the given flow feature (Schrijer and Scarano, 2008).

As the vector processing underwent multiple steps with reducing window sizes, as seen in Table 4.8, the window size used for the uncertainty due to spatial resolution will be set as the final window size of 32 voxels. As identified by De Kat and Van Oudheusden (2012), the spatial wavelength, λ is defined by the accepted ratio that $l^* = 0.5$; therefore, the smallest resolvable flow feature will have a length of twice the final window size, WS. This is equal to approximately 2.9 mm.

Theunissen (2012) states that the moving average approach to the interrogation process outlined Schrijer and Scarano (2008) has gained widespread acceptance among researchers. Spencer and Hollis (2005) additionally claims that the simplification works because it correctly captures the effects of the low-pass filtering induced when attempting to resolve flow features smaller than the interrogation window size.

4.6.3 Uncertainty remarks

Tables 4.10 through 4.14 show the normalized uncertainty for each of the conducted experimental cases. As noted, the uncertainties are derived from the limited ensemble size and the PIV measurement technique. All uncertainty values are normalized by the freestream velocity, U_∞ and presented as a percentage thereof. Additionally, a voxel value is presented such that the uncertainty can be observed relative to the PIV system. This is done by taking the dimensional uncertainties, ϵ and multiplying them by the time step, Δt and resolution in pix/m. The outermost measurement planes of the tomographic results were discarded for all presented results because these planes contained higher uncertainty values. Lastly, the summation of those uncertainties, which are rooted in velocity, is less than 5% for all experimental cases.

	[%]	[vox.]
$\epsilon_{\overline{u}}/U_\infty$	0.41	0.57
$\epsilon_{\overline{v}}/U_\infty$	0.29	0.40
$\epsilon_{\overline{w}}/U_\infty$	0.33	0.45
$\epsilon_{\langle u' \rangle}/U_\infty$	0.23	0.32
$\epsilon_{\langle v' \rangle}/U_\infty$	0.38	0.52
$\epsilon_{\langle w' \rangle}/U_\infty$	0.27	0.37
$\epsilon_{\overline{u'v'}}/U_\infty^2$	0.04	-
$\epsilon_{\tau_p}/U_\infty$	0.67	0.93
$\epsilon_{u(\epsilon_{cc})}/U_\infty$	0.35	0.49
ϵ_{SR}/U_∞	0.9	1.25

Table 4.10: Normalized uncertainty for Mach 0.7 validation case

	[%]	[vox.]
$\epsilon_{\overline{u}}/U_\infty$	0.32	0.45
$\epsilon_{\overline{v}}/U_\infty$	0.22	0.32
$\epsilon_{\overline{w}}/U_\infty$	0.26	0.37
$\epsilon_{\langle u' \rangle}/U_\infty$	0.18	0.26
$\epsilon_{\langle v' \rangle}/U_\infty$	0.34	0.50
$\epsilon_{\langle w' \rangle}/U_\infty$	0.24	0.35
$\epsilon_{\overline{u'v'}}/U_\infty^2$	0.02	-
$\epsilon_{\tau_p}/U_\infty$	0.86	1.20
$\epsilon_{u(\epsilon_{cc})}/U_\infty$	0.58	0.88
ϵ_{SR}/U_∞	0.9	1.37

Table 4.11: Normalized uncertainty for Mach 1.5 validation case

	[%]	[vox.]
$\epsilon_{\overline{u}}/U_\infty$	0.76	1.13
$\epsilon_{\overline{v}}/U_\infty$	0.54	0.80
$\epsilon_{\overline{w}}/U_\infty$	0.51	0.75
$\epsilon_{\langle u' \rangle}/U_\infty$	0.36	0.53
$\epsilon_{\langle v' \rangle}/U_\infty$	0.51	0.76
$\epsilon_{\langle w' \rangle}/U_\infty$	0.36	0.54
$\epsilon_{\overline{u'v'}}/U_\infty^2$	0.09	-
$\epsilon_{\tau_p}/U_\infty$	0.64	0.95
$\epsilon_{u(\epsilon_{cc})}/U_\infty$	0.34	0.47
ϵ_{SR}/U_∞	0.9	1.25

Table 4.12: Normalized uncertainty for $L/D = 0.6$ case

	[%]	[vox.]
$\epsilon_{\overline{u}}/U_\infty$	0.74	1.10
$\epsilon_{\overline{v}}/U_\infty$	0.52	0.78
$\epsilon_{\overline{w}}/U_\infty$	0.48	0.71
$\epsilon_{\langle u' \rangle}/U_\infty$	0.34	0.50
$\epsilon_{\langle v' \rangle}/U_\infty$	0.50	0.74
$\epsilon_{\langle w' \rangle}/U_\infty$	0.35	0.52
$\epsilon_{\overline{u'v'}}/U_\infty^2$	0.10	-
$\epsilon_{\tau_p}/U_\infty$	0.64	0.89
$\epsilon_{u(\epsilon_{cc})}/U_\infty$	0.34	0.47
ϵ_{SR}/U_∞	0.9	1.25

Table 4.13: Normalized uncertainty for $L/D = 1.2$ case

	[%]	[vox.]
$\epsilon_{\overline{u}}/U_\infty$	0.56	0.80
$\epsilon_{\overline{v}}/U_\infty$	0.39	0.57
$\epsilon_{\overline{w}}/U_\infty$	0.38	0.54
$\epsilon_{\langle u' \rangle}/U_\infty$	0.27	0.38
$\epsilon_{\langle v' \rangle}/U_\infty$	0.42	0.60
$\epsilon_{\langle w' \rangle}/U_\infty$	0.30	0.43
$\epsilon_{\overline{u'v'}}/U_\infty^2$	0.05	-
$\epsilon_{\tau_p}/U_\infty$	0.64	0.89
$\epsilon_{u(\epsilon_{cc})}/U_\infty$	0.34	0.47
ϵ_{SR}/U_∞	0.9	1.25

Table 4.14: Normalized uncertainty for $L/D = 1.8$ case

Chapter 5

Comparison and Validation of Measurement Technique

In the present chapter, the results from the first experimental campaign are presented; this entails the schlieren images, pressure transducers measurements, and the PIV measurements. As it was originally intended to test at subsonic and supersonic Mach numbers, the first experimental campaign included measurements at Mach 0.7 and 1.5. This was later abandoned in the second experimental campaign due to time constraints. As such, the results are still presented herein as a comparison to the main subsonic results.

5.1 Schlieren Results

All displayed images use the same origin as the PIV results; the origin is indicated by the blue 'x' in Figure 4.4 and is located at the foot of the BFS. The results for the supersonic case at Mach 1.5 are shown in Figure 5.1 and the subsonic case at Mach 0.7 are seen in Figure 5.2. For the purposes of better understanding the forthcoming PIV based mean flow field, the schlieren images serve to identify key topological features of interest.

Figure 5.1(a) shows the vertical density gradients in the supersonic flow field; it is particularly good for visualizing the boundary layer (BL) and shear layer (SL). The developed boundary layer can be seen flowing over the model and separating at the edge of the BFS; the sudden change from white to a darker, more freestream like black color alludes that there is a very steep vertical velocity gradient; this is indicative of a turbulent boundary layer. At the point of separation at the edge of the BFS, two major flow features are visible. The first is the separated shear layer which flows over the base and impinges downstream on the support sting; between the shear layer and the model, a recirculation region is visible because of its relatively higher density when compared to the freestream flow. A second feature emanating from the edge of the BFS is a Prandtl-Meyer expansion fan (PME). This diagonal feature

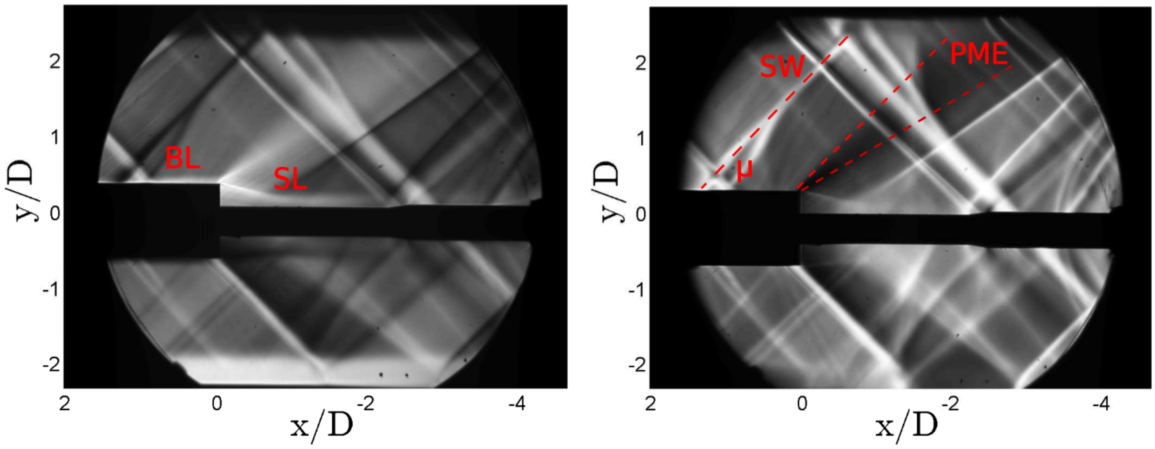

(a) Horizontal knife - vertical gradients

(b) Vertical knife - horizontal gradients

Figure 5.1: Schlieren mean flow field results at Mach = 1.5 using horizontal and vertical knife

also exhibits a large density gradient as it angles the freestream flow downwards, accelerating it in the process. As the shear layer reaches the sting, it is turned inward onto itself causing a recompression shockwave to occur near the point of reattachment.

Figure 5.1(b) shows the horizontal density gradients of the same mean flow field. From this perspective, the shockwaves (SW) are more apparent due to the strong horizontal velocity and density gradients which they impart. A downside of this perspective is the diminished view of the boundary layer and shear layer; the image is dominated by shockwaves, many of which originate at the nose of the model and reflect downstream off of the tunnel walls. Additional insight can be gained by calculating the Mach number, M based on the Mach angle, μ seen in equation 5.1. Based on an approximate Mach angle, $\mu = 40°$, the flow Mach number, $M \approx 1.55$.

$$M = \frac{1}{\sin \mu} \tag{5.1}$$

Furthermore, it can be concluded from Figures 5.1(a) and 5.1(b) that the shockwaves are adequately strong such that their visualization is not necessarily difficult; what is more difficult to capture is the boundary layer. Therefore, all subsequent schlieren measurements used a horizontal schlieren knife because this allowed for better insight into the boundary layer and shear layer while still allowing for adequate shockwave visualization.

Figure 5.2 shows the vertical density gradients of the mean flow field by schlieren for the subsonic Mach 0.7 case; it is a much simpler image when compared to the previous case. Note that the minimum exposure time of the Bobcat cameras is too long to make instantaneous features and thus single images appeared blurred in the freestream; additionally, due to the use of a continuous light source as opposed to a spark light source, further reduction in exposure time is impossible. Nevertheless, Figure 5.2 shows topological features which are paramount to the investigation.

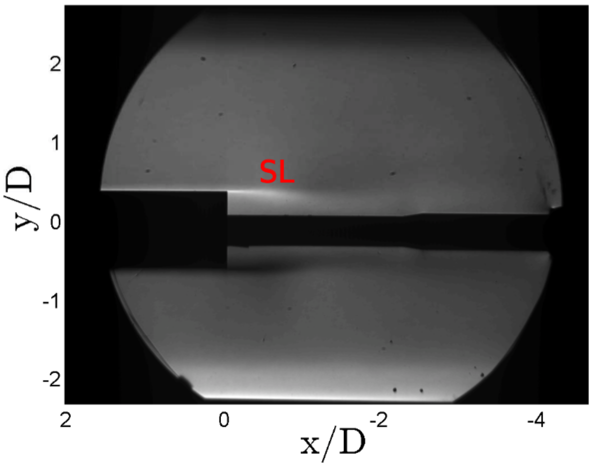

Figure 5.2: Schlieren mean flow field results at Mach = 0.7 using horizontal knife

The shear layer (SL) with its large vertical velocity gradient is seen to be emanating from the edge of the BFS. Though its mean reattachment location cannot be exactly ascertained from the image, it appears to be in the vicinity of the expected location at $x/D = -1.0$. In the subsonic case, seen in Figure 5.2, the shear layer reattachment location is seen to be significantly further downstream than the supersonic case seen in Figure 5.1. This is because of the presence of the PME in the supersonic case which causes a deflection in flow angle downward toward the sting; in turn, this leads to significantly shorter distances to the reattachment location as discussed in section 2.3.2.

The boundary layer is visible in both Figure 5.1(a) and Figure 5.2. A stark contrast in shade is evident at the edge of the boundary layer, this shows a strong density gradient, and thus velocity gradient. This density gradient, and the approximate boundary layer thickness, appears to be greater for the supersonic case compared to the subsonic case. A subsequent boundary layer analysis in section 5.4, particularly Figures 5.7(b) and 5.21(b), concludes that the incoming boundary layers are turbulent and that for the supersonic case this boundary layer is thicker and has a larger velocity gradient. Such a strong gradient is indicative of a turbulent boundary layer.

5.2 Unsteady Pressure Transducers

A Fast Fourier Transform (FFT) is performed using the sting mounted pressure transducer measurements. The frequency spectra are non-dimensionalized as the Strouhal number using the main body diameter and freestream velocity as introduced earlier in section 2.3.4, equation 2.4. As identified by Schrijer et al. (2014), the Strouhal peak of the first mode ($St \approx 0.08$) is clearly visible in the frequency spectra at all four measured locations, though the peak diminishes near the point of reattachment. Upon moving further downstream, the energy associated with the first mode is decreased and that associated with the second mode increases. The second mode represents vortex shedding occurring near the point of reattachment, the frequency of which is seen to be approximately $St \approx 0.17$. Comparatively, the same approach

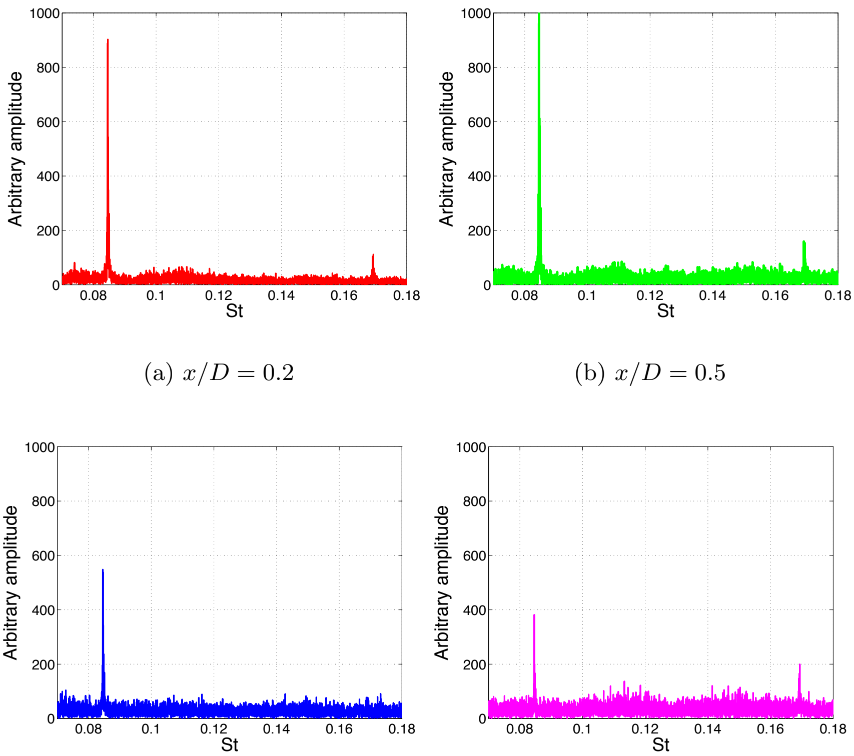

(a) $x/D = 0.2$

(b) $x/D = 0.5$

(c) $x/D = 0.8$

(d) $x/D = 1.1$

Figure 5.3: Non-dimensionalized frequency spectra for unsteady transducer measurements at Mach 0.7

using the pressure transducer measurements from the supersonic Mach 1.5 case yields different results. Therein, there are no apparent amplitude peaks and values only begin a linear rise near a Strouhal number on the order of $\mathcal{O}(10^{-4})$. This extra data is deemed extraneous, attributed to signal noise, by which it is concluded that the low-frequency unsteadiness found in the subsonic case is not present in the supersonic case.

5.3 Subsonic Case: Instantaneous Flow Results

Instantaneous PIV snapshots

The study of the mean flow field is comprised of 500 instantaneous snapshots of the flow field. Figure 5.4 shows two separate, uncorrelated instances of the instantaneous flow field; in those images, an unsteady shear layer can be seen which deviates from the mean. As discussed in theory in section 2.1.1, it appears as though the snapshots represent the two extremes of the second unsteady flapping mode, as identified by Schrijer et al. (2014). The left column in

Figure 5.4 shows an instance with a smaller recirculation region and the right column shows a significantly larger recirculation region; this can be linked to the momentum injection and ejection as discussed earlier. This shear layer flapping mode is attributed to the effect of large-scale vortical structures injecting and expelling momentum into the recirculation region at upstream or downstream locations, respectively.

The two other component directions, v and w appear significantly more chaotic and disorganized than the streamwise component, u. In all component directions, large, coherent vortical structures are present, particularly at the base of the BFS for the injection and further downstream for the ejection event. The large streamwise (u) component seen in Figure 5.4(a) is transferred to the radial component (v) during the ejection as seen in Figure 5.4(d). This occurrence shows good, qualitative agreement with Scharnowski et al. (2016a) who performed transonic PIV research on a two-dimensional BFS. Additionally, the time-averaged streamwise variation in Reynolds normal stresses, discussed in 5.4, also give insight into the unsteady motion taking place.

Out-of-plane vorticity

There is an increase in out-of-plane vorticity associated with the momentum injection and ejection events seen in Figure 5.4. As previously shown, these two snapshots mark the extreme ends of momentum injection and ejection of the second unsteady mode. As can be seen in the shear layer for both instances, predominantly clockwise rotating vortices can be seen pairing with counter-clockwise vortices near the point of reattachment, as defined by the right hand rule. The vortex pairing which is captured is also discussed in section 2.1.1.

Shear layer reattachment location

The mean shear layer reattachment location is found to be at approximately $\overline{x_r}/D = 0.99$. The probability density function (PDF) of the reattachment location of all 500 PIV snapshots is shown in Figure 5.6. The minimum reattachment location, $x_{r_{\min}}/D = 0.54$ and the maximum, $x_{r_{\max}}/D = 1.31$. Reattachment location was calculated by taking the 'radial' mean of the lowest three rows of the streamwise velocity component and fitting a third order polynomial to the streamwise velocity development; the reattachment location is determined as the x-intercept of the polynomial where the streamwise flow goes from negative to positive. The RMS of the deviation from the mean x_r location is $(x_r - \overline{x_r})_{\mathrm{RMS}}/D = 0.12$.

Correlation with backflow A cross-correlation is performed between the reattachment length, x_r and the maximum backflow in the recirculation region. It is found that the two flow variables, normalized by the subtraction of their means, share an inverse relationship with a correlation coefficient of -0.31. That is to say that when the reattachment length is long then the maximum backflow is decreased. This is representative of the second unsteady mode because when a momentum ejection event occurs, the reattachment length is long and the recirculation region ‘bursts’ sending momentum downstream. During such a bursting event the backflow is reduced, leading to a correlation between the two variables.

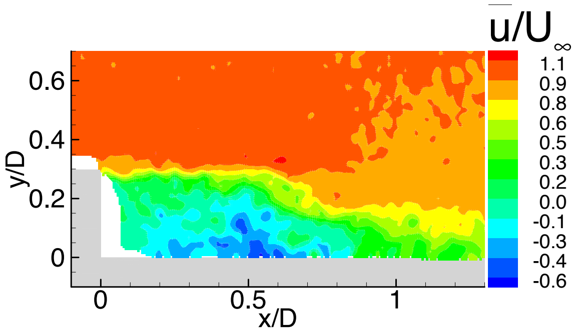

(a) u/U_∞

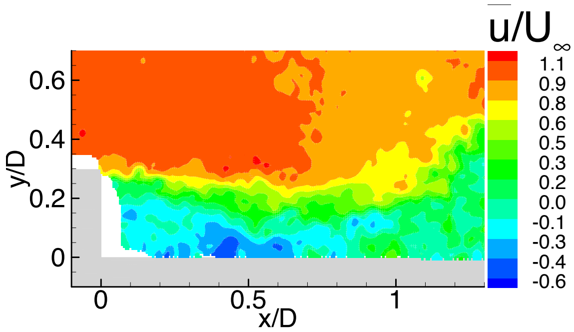

(b) u/U_∞

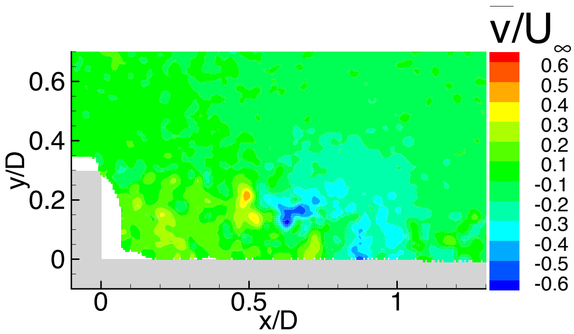

(c) v/U_∞

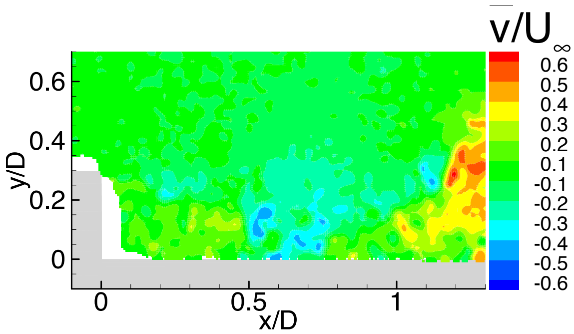

(d) v/U_∞

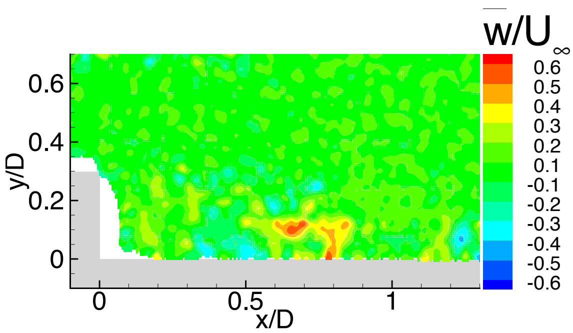

(e) w/U_∞

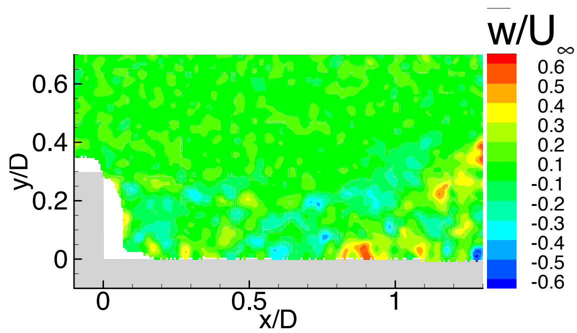

(f) w/U_∞

Figure 5.4: Instantaneous snapshots of the Mach 0.7 flow field; momentum injection (left) and ejection (right)

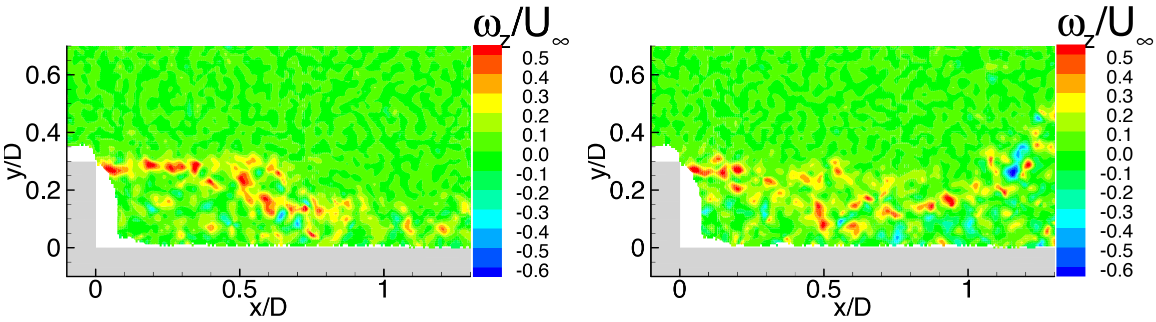

(a) momentum injection

(b) momentum ejection

Figure 5.5: Instantaneous out-of-plane vorticity, ω_z

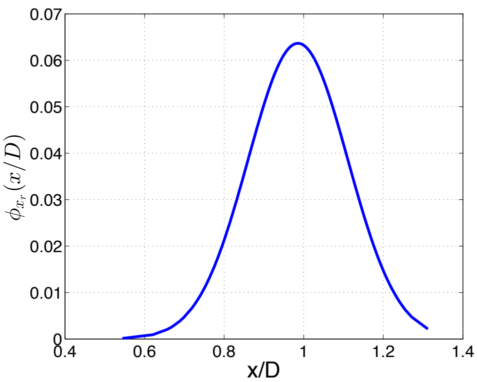

Figure 5.6: PDF of the reattachment location, x_r for Mach 0.7 case

5.4 Subsonic Case: Mean Flow Results

In-flow boundary layer

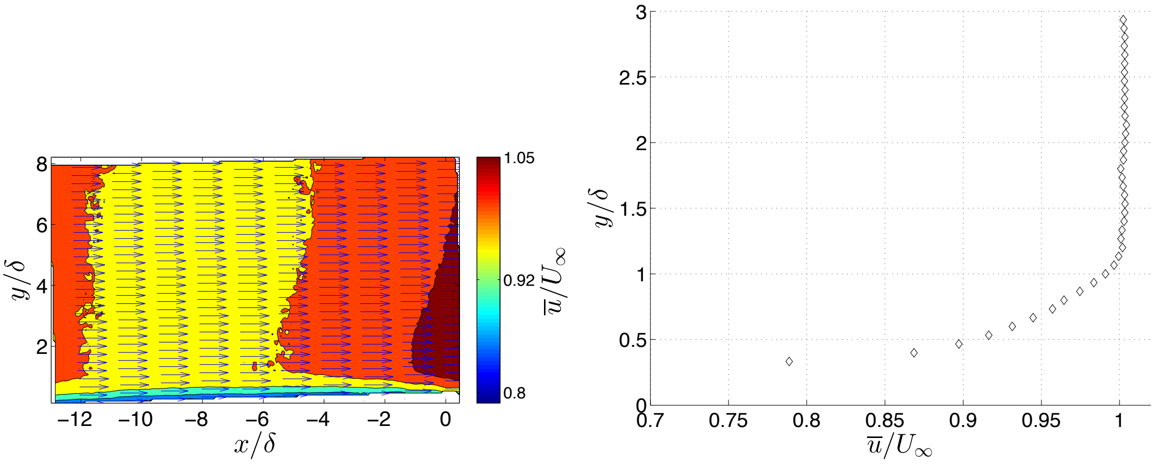

(a) mean velocity field

(b) velocity profile

Figure 5.7: Mean velocity field and velocity profile over model main body upstream of separation for Mach 0.7 case

The boundary layer is investigated to ascertain the freestream velocity, U_∞ and the type of boundary layer present before separation. This is done using an additional CCD camera in a planar 2C fashion mounted to view the region upstream of the point of separation. The resultant Planar FOV is 66 mm wide by 50 mm tall; the mean results are comprised of 250 image pairs. A general vector plot of the boundary layer is seen in Figure 5.7(a) and a velocity profile for the boundary layer is seen in Figure 5.7(b). Boundary layer thickness is taken as the height where $\overline{u} = 0.99 \cdot U_\infty$ and this is measured 25 mm upstream of the edge of the BFS. This is equivalent to 233 mm from the nose of the model and 135 mm from the beginning of the main body (see Figure 4.4).

The resultant velocity profile for the Mach 0.7 case shows a boundary layer thickness, $\delta \approx 4.8$ mm or $\delta/D \approx 0.10$. The steep increase in velocity seen in Figure 5.7(b) is indicative of a turbulent boundary layer. To reinforce this conclusion, the Reynolds number is sufficiently high, the reattachment length of the BFS is in line with that of a turbulent incoming boundary layer according to Isomoto and Honami (1989), and the model is equipped with a 'trip-strip'.

The PIV system is unable to resolve velocity exactly at the wall; instead, the first measured velocities are at a height of approximately 1.5 mm above the wall. Due to this, only the outer layer of the boundary layer is measured (Pope, 2000); the lowest calculated y^+ value is approximately 1,000. The velocity profile is investigated as the dimensionless wall variables, y^+ and u^+ using Coles' law of the wake; from this investigation it is concluded that the PIV system was unable to sufficiently resolve the flow field close to the wall, thus hindering further boundary layer study.

Mean velocity field

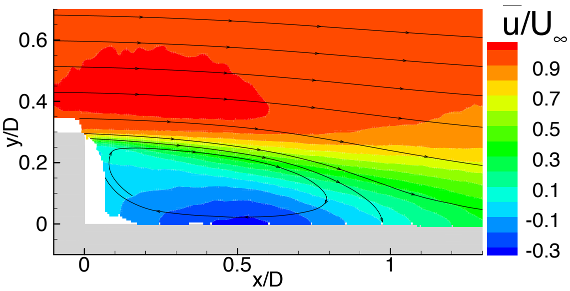

(a) Streamwise, $\overline{u}$

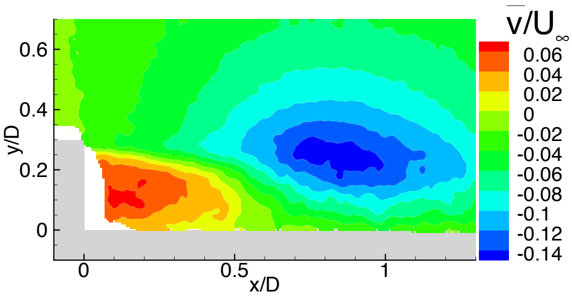

(b) Radial, $\overline{v}$

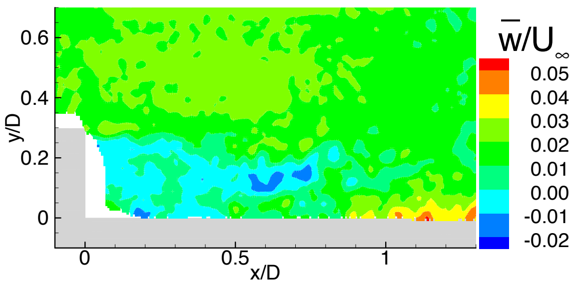

(c) Out-of-plane, $\overline{w}$

Figure 5.8: Mean velocity components for Mach 0.7 case

Figure 5.8 shows the mean velocity components in the streamwise, radial, and out-of-plane directions; these values are nondimensionalized with the freestream velocity, $U_\infty = 242.5$ m/s. As is expected with this model, the reattachment is entirely solid due to the practically infinite L/D length. though this has been stated by Bitter et al. (2011) to have the potential to slightly delay flow reattachment when compared to a finite afterbody length (e.g. $L/D = 1.2$). Figure 5.8(a), which presents the streamwise component, $\overline{u}$ in particular, shows that the mean reattachment location is at approximately $\overline{x_r}/D = 0.99$, which is in accordance with other measurements as discussed in section 2.1.2.

Maximum backflow is $-0.33 \cdot U_\infty$, which occurs at $x/D = 0.51$ very low and close to the sting. The aforementioned work by Bitter et al. (2011) also tested a sting mounted rocket model at, among other Mach numbers, Mach 0.7, $Re_D = 1e6$ using PIV. A qualitative comparison of Figure 5.8(a) with results presented by Bitter et al. (2011) shows very good agreement. Additionally, Bitter et al. (2011) found a maximum backflow velocity of 35% of freestream velocity, U_∞. Such good agreement demonstrates that the flow field is adequately converged when one considers that Bitter et al. (2011) used 8,000 images, correlated in time, compared to the 500 uncorrelated images used herein.

Figures 5.8(b) and 5.8(c) show the mean radial and out-of-plane velocity components, respectively. These images appear 'noisier' due to the higher normalized uncertainty for these velocity components as outlined in section 4.6; nevertheless, they provide important insight into the flow field. The radial velocity component seen in Figure 5.8(b) shows the effects of the recirculation region and the shear layer which separates it from the outer flow field.

Figure 5.8(c) shows the out-of-plane component of the mean, axisymmetric flow field. As such, it is expected to be zero but upon inspecting the figure, non-zero values are found. Maximum out-of-plane velocity is measured to be $0.05 \cdot U_\infty$ or roughly 12 m/s, though most values are far closer to $0.02 \cdot U_\infty$, which is approximately 5 m/s. Table 4.10 shows the statistical uncertainties for these measurements, which at maximum are $0.05 \cdot U_\infty$. If the flow were completely symmetrical, the model perfectly aligned, and the mean flow field fully converged, the plot would show zero at all points. That not being the case means that each of the aforementioned issues could play some role in Figure 5.8(c) being non-zero. It is stated by Gentile et al. (2016), that due to the very low frequency of the precessing antisymmetric mode, it is not visible in a mean flow field.

Velocity statistics

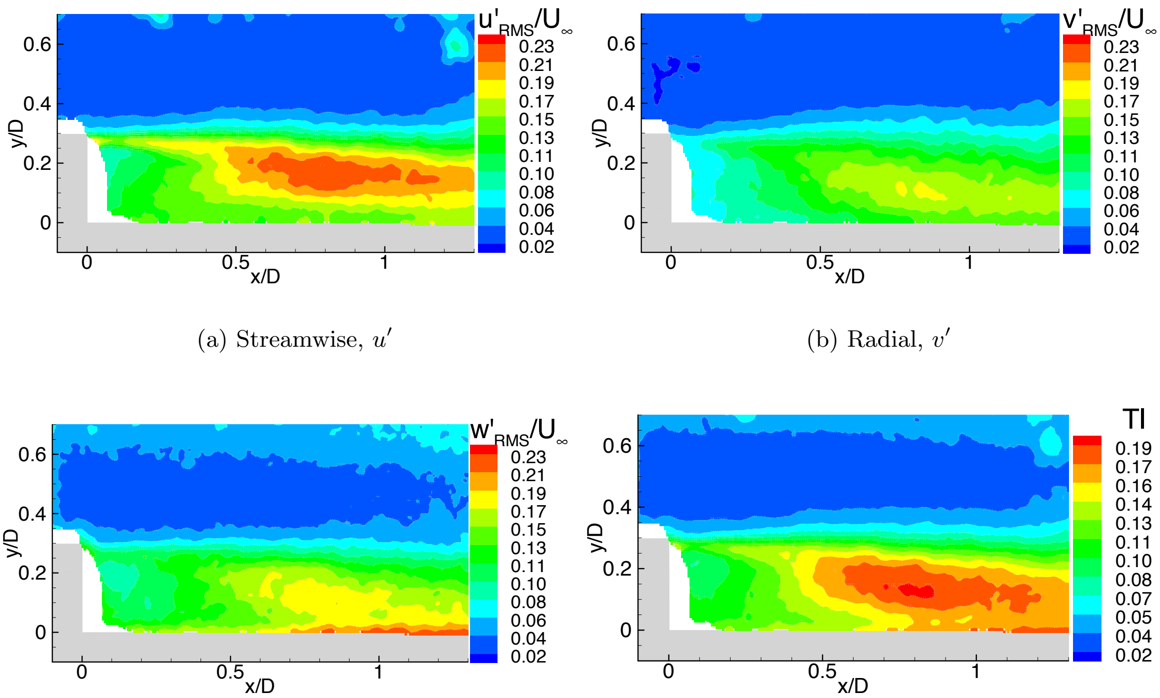

(a) Streamwise, u'

(b) Radial, v'

(c) Out-of-plane, w'

(d) Turbulence Intensity

Figure 5.9: RMS of velocity fluctuations and turbulence intensity for Mach 0.7 case

The RMS of the velocity fluctuations in all three component directions are presented in Figure 5.9; the components are normalized and the resulting plots share the same scale for comparison. The maximum streamwise fluctuation, $u' = 58.5$ m/s ($u' = 0.24 \cdot U_\infty$) occurring slightly upstream of the point of reattachment at $x/D = 0.86$. In the radial direction, the maximum fluctuation of the velocity, $v' = 48.1$ m/s ($v' = 0.20 \cdot U_\infty$) occurring slightly downstream of reattachment at $x/D = 1.12$. The maximum out-of-plane velocity fluctuation, $w' = 62.6$ m/s ($w' = 0.26 \cdot U_\infty$) occurs further downstream at $x/D = 1.39$.

The RMS values presented in Figure 5.9 give insight into the unsteadiness of the flow field. As discussed in section 2.1.3, certain topological flow features of the BFS exhibit unsteady oscillations, exclusively in the wake of the BFS. The freestream flow exhibits no unsteady motion and therefore the RMS of the velocity fluctuations in all component directions is practically zero. Figure 5.9(a) shows the greatest variation in velocity fluctuations in the streamwise direction in the wake of the BFS; this is caused by the unsteadiness in the separated shear layer, convection of vortices, and the reattachment process. In this unsteadiness, the reattachment location of the separated shear layer varies in a streamwise direction. The momentum injection and ejection from the recirculation region is seen in the instantaneous flow fields in section 5.3, Figure 5.4.

The same unsteady modes identified by Schrijer et al. (2014) also present flow unsteadiness in the other two component directions, v' and w' as seen in Figures 5.9(b) and 5.9(c), respectively. When comparing the unsteadiness in component directions, it is clear that the majority of unsteady motion is in the streamwise direction and that the radial and out-of-plane directions possess significantly less unsteadiness. This unsteadiness can still be attributed to the motion of the shear layer as previously identified and shows that this topological flow feature also fluctuates in a three-dimensional manner.

Figure 5.9(d) shows the turbulence intensity calculated using equation 5.2. The greatest turbulence intensity ($T.I. \approx 0.21 \cdot U_\infty$) is found downstream of the point of reattachment at $x/D \approx 1.43$, as is observed in Figure 5.9(d). This is indicative of the highly three-dimensional and turbulent flows associated with the recirculation and reattachment regions of the BFS.

$$\text{Turbulence intensity} = \frac{\sqrt{\frac{(u'_{\mathrm{RMS}})^2+(v'_{\mathrm{RMS}})^2+(w'_{\mathrm{RMS}})^2}{3}}}{U_\infty} \tag{5.2}$$

Reynolds stress

The Reynolds stress terms, $\overline{u'v'}$, $\overline{u'w'}$, and $\overline{u'w'}$ are shown in Figure 5.10. Good, qualitative agreement is found between the result shown herein and that from Bitter et al. (2011) for the $\overline{u'v'}$ stress term. Quantitatively, the maximum achieved Reynolds stress for the Mach 0.7 case is approximately 6% of U_∞ compared to 2% as reported by Bitter et al. (2011). When comparing the Reynolds stress terms among themselves, it can be seen that the in-plane stresses are larger than those involving the out-of-plane, w term. Compared to a maximum value of 6%, as mentioned previously, the Reynolds stresses, $\overline{u'w'}$ and $\overline{v'w'}$ each achieve a maximum of 1.5%.

The negative valued Reynolds stress, as seen in Figure 5.10(a), is indicative of turbulence production (White, 2006). This is to be expected from a separated flow aft of a BFS as discussed in Chapter 2. It can be seen that a majority of the turbulent production occurs in a streamwise and radial direction, as indicated by the larger quantities in the in-plane Reynolds stress, $\overline{u'v'}$. Later, the terms of the mean pressure reconstruction will show that these in-plane terms are also the most important for the performance of said technique.

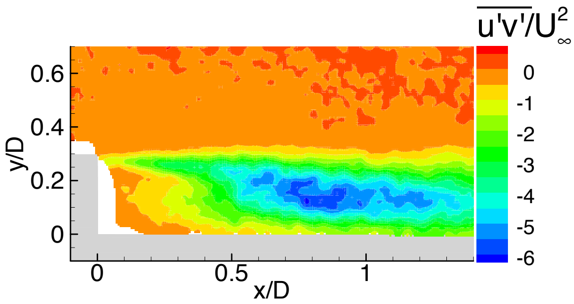

(a) $\overline{u'v'}$

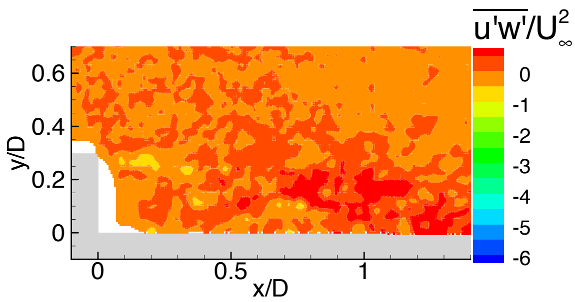

(b) $\overline{u'w'}$

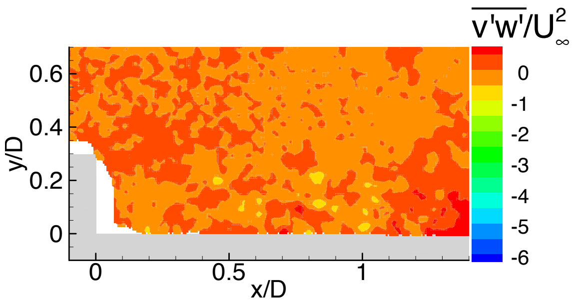

(c) $\overline{v'w'}$

Figure 5.10: Reynolds stress terms for the Mach 0.7 case

Mixing layer analysis

The separated mixing layer forms an important part of the study of the BFS. In the following section, the streamwise development of several important parameters will be investigated. The PIV results used herein provide sufficiently high resolution for such a study, though Simon et al. (2007) and Weiss et al. (2009) recommend using nearly 60 stations for better insight into streamwise development; the present analysis makes use of six equidistantly placed stations at $x/D = 0.2, 0.4, 0.6, 0.8, 1.0$, and 1.2.

Streamwise velocity

Figure 5.11 shows the development of the mean streamwise velocity, $\overline{u}$ as a function of streamwise distance, x/D. The data for the plot is derived from the mean flow field seen in Figure 5.8(a) where datasets are taken for streamwise stations; the stations are indicated in the figure. It can be seen that the velocity gradient of the shear layer gradually decreases when moving

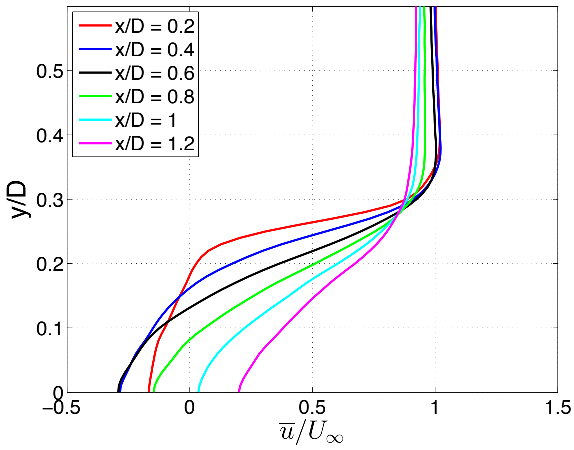

Figure 5.11: Streamwise velocity development for Mach 0.7 case

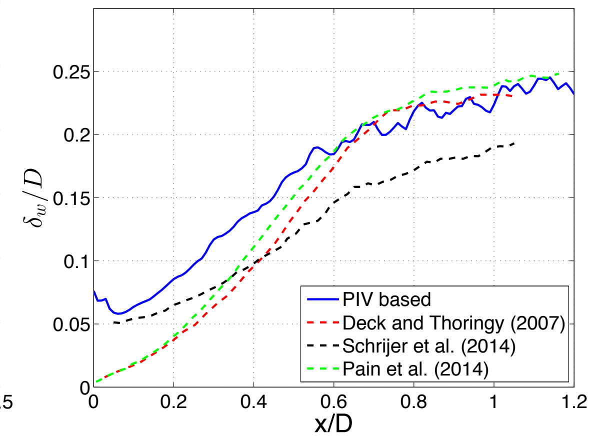

Figure 5.12: Streamwise vorticity thickness development for Mach 0.7 case

downstream; as expected, eventually all reach freestream velocity. This demonstrates a thickening of the shear layer due to fluid entrainement and momentum transfer across the shear layer and into the recirculation region. Additionally, the backflow is greater at $x/D = 0.4$ than at $x/D = 0.2$, this is because the point of maximum backflow occurs at approximately $x/D \approx 0.5$.

Vorticity thickness

As part of the mixing layer analysis, the streamwise development of the characteristic shear layer thickness is an important aspect to investigate; according to Pope (2000), the shear layer is defined by given velocity gradients in the flow. The characteristic thickness of the shear layer can be defined as its vorticity thickness. This approach works better than investigating the shear layer thickness because the bounds of the shear layer, as defined by the velocity gradients, are not well known. Deck and Thorigny (2007) defines the vorticity thickness as seen in equation 5.3.

$$\delta_w(x) = \max_y \left[\frac{U_\infty - \overline{u}_{\min}}{\frac{\partial \langle u \rangle (x,y)}{\partial y}} \right] \tag{5.3}$$

Figure 5.12 shows the vorticity thickness as a function of streamwise distance, x/D. In the recirculation region, the slope of the streamwise vorticity thickness development is approximately $d\delta_w/dx \approx 0.25$. Overall, the PIV based vorticity thickness finds the best agreement with the experimental PIV results from Schrijer et al. (2014), which also did not feature an exhaust plume. The visible disparity close to the BFS is most likely due to the limited spatial resolution of the measurements. Nearer the point of reattachment, these results feature better agreement in vorticity growth rate.

The results from Deck and Thorigny (2007) and Pain et al. (2014) were based on a numerical ZDES simulation, with a nozzle length $L/D = 1.2$ and without an exhaust plume. In Figure

5.12 it can be seen that the agreement in the recirculation region is worse with these numerical results and improves further downstream; the vorticity growth rate of the results by Deck and Thorigny (2007) is approximately $\frac{d\delta_w}{dx} \approx 0.35$, significantly higher than that reported for the present results. The increased vorticity growth rate of the numerical simulations could be due to the finite afterbody length, $L/D = 1.2$ which leads to a more turbulent wake, in turn ingesting more vortices into the recirculation region, as discussed in Chapter 2.

Streamwise Reynolds normal stresses

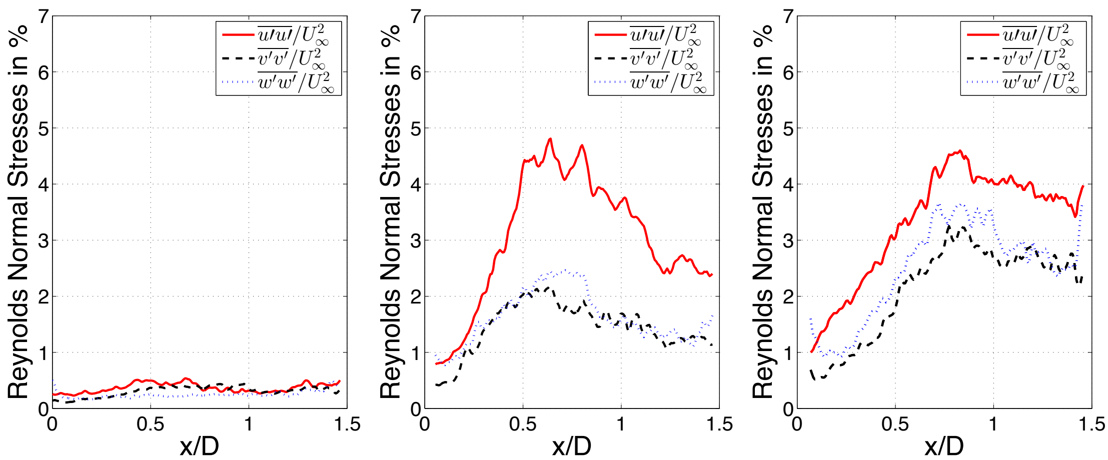

(a) Top of BFS ($y/D = 0.33$) (b) 2/3 of BFS ($y/D = 0.22$) (c) 1/3 of BFS ($y/D = 0.11$)

Figure 5.13: Streamwise development of Reynolds normal stresses at varying BFS heights

The streamwise development of the Reynolds normal stresses is presented in Figure 5.13. Results show the mean Reynolds normal stresses plotted streamwise for three separate planes perpendicular to the BFS. At the upper edge of the BFS step, Figure 5.13(a) shows the normal Reynolds stresses to be quite small when compared to the far larger values found in the wake of the BFS. Additionally, there is no clearly dominant component direction as all are approximately equal. Figure 5.13(b) shows a lower plane, closer to the afterbody, where the values have increased dramatically. The strong increase in the streamwise Reynolds normal stress, $\overline{u'u'}$ is evidence of the three-dimensional nature of the BFS wake. Such dominance of the streamwise term is most likely a result of the deformation of the rolling vortex-pairs in the shear layer interacting with the recirculation region (Scharnowski et al., 2016a).

Upon moving one plane lower, the other two Reynolds normal stress terms, $\overline{v'v'}$ and $\overline{w'w'}$ increased their value to match that of the streamwise component, $\overline{u'u'}$, which has stayed largely the same. This occurs closer to the sting and further downstream, indicating more equal, turbulent fluctuations in all component directions, especially at the point of reattachment. This is indicative of the chaotic and turbulent nature of the flow at the point of reattachment.

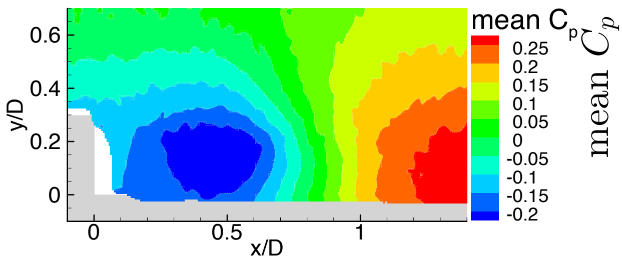

Figure 5.14: Mean C_p for Mach 0.7 case

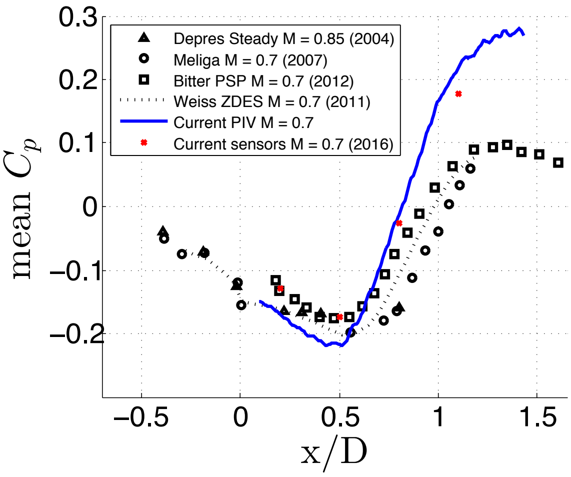

Figure 5.15: Comparison of mean C_p to pressure transducers and literature

Mean pressure

Figure 5.14 shows the central slice of the reconstructed mean pressure volume; the main body and afterbody of the model, equipped with pressure transducers, are also visible in the figure. Figure 5.15 shows the wall pressure value as resolved by the PIV based pressure reconstruction. The values for the wall pressure are taken as the average of the lowest two rows of the data. The pressure transducers seen in Figure 5.15 are those indicated by red x's in the model illustration seen in Figure 4.4; these pressure transducers are located on the sting at $x/D = 0.2$, 0.5, 0.8, and 1.1. Additionally, the results from the present experiment are compared to literature.

Qualitatively, the mean C_p seen in Figure 5.14 is as expected from section 2.2.2, Figure 2.5. The mean pressure coefficient reaches a minimum wall value of -0.19 at $x/D \approx 0.5$; Deprés et al. (2004) measured a minimum $C_p = -0.17$ at the same location, $x/D = 0.5$. Generally, it is accepted that for subsonic BFS flows ($M_\infty \leq 0.85$) that $C_{p_{\min}} \approx -0.125$ (Deprés et al., 2004). In Figure 5.15, the agreement between the PIV based pressure reconstruction and the pressure transducers is very good, showing an average offset in C_p of 0.019 or approximately 10%.

Figure 5.15 also shows the PIV based pressure reconstruction compared to BFS results from other researchers; the literature covers a broad range of experimental methods. Deprés et al. (2004) used approximately 80 PM131-Statham transducers at $Re_D = 1.2 \cdot 10^6$; Meliga and Reijasse (2007) experimentally investigated wall-pressure on an axisymmetric model with two boosters using 12 Statham sensors at $Re_D = 1.35 \cdot 10^6$. Bitter et al. (2012) used pressure sensitive paint to make wall-pressure measurements on an axisymmetric model at $Re_d = 1.0 \cdot 10^6$; Lastly, Weiss and Deck (2011) used ZDES to numerically investigate an axisymmetric BFS flow. The results from the present experiment show better agreement nearer the base of the BFS.

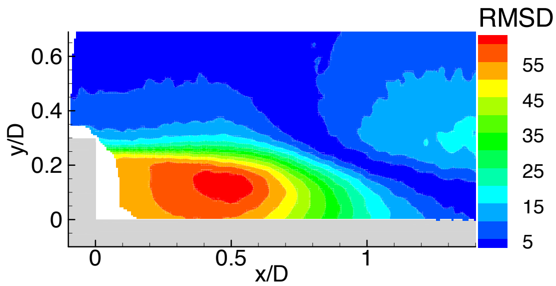

Figure 5.16: RMSD of Poisson solver result and isentropic assumption applied to entire flow field

The collective literature data shows an approximate trend of $dC_p/dx \approx 0.5$ whereas the PIV based results and pressure transducers show a steeper gradient of approximately $dC_p/dx \approx 0.8$ for the region $0.5 \leq x/D \leq 1.0$. Though, in the recirculation region the agreement with literature is quite good, about 0.0175 offset in C_p or 10%, this grows when moving downstream. Physically, the sharper increase is indicative of a higher streamwise pressure gradient, dC_p/dx for the present experiment. Toward the point of reattachment, the offset in C_p has grown to approximately 0.1 or 50%.

When moving further from the base, both the PIV based pressure reconstruction and the transducer measured pressure values diverge from the literature; though, the general trend is maintained, the difference is apparent. It is encouraging that the two separate techniques used in the present experiment are still in very good agreement with one another; this lends credence to the fact that there is a fundamental difference between this experiment and the data which is sourced from literature.

Validity of isentropic boundary condition Figure 5.16 shows the RMSD between the aforementioned tomographic reconstruction and the mean pressure calculated when assuming isentropic flow at all points. This is done to ensure that the assumption of isentropic flow along the top bound is valid. It can be seen that along the top bound, the RMSD percentage is approximately 1% in the upstream region and slightly higher when moving downstream. The recirculation region, directly in the wake of the BFS shows the greatest deviation. From Figure 5.16 it can be concluded that the approach taken for the present calculation incorporates a valid assumption of isentropic flow.

PIV Component Reduction for Pressure Reconstruction

The original pressure formulation used for the tomographic PIV results as presented earlier, is seen in equation 5.4. The resulting central slice of the pressure reconstruction is visible in Figure 5.17(b). This is the benchmark by which the reduction to planar PIV will be compared.

Using the tomographic PIV results which were gathered through experimentation, an artificial reduction to 2D2C PIV will be created by eliminating terms which cannot be measured with said technique.

$$
\begin{aligned}
\frac{\partial \overline{p}}{\partial x} &= -\frac{1}{RT}\left[\overline{u}\frac{\partial \overline{u}}{\partial x}+\overline{v}\frac{\partial \overline{u}}{\partial y}+\overline{w}\frac{\partial \overline{u}}{\partial z}+\frac{\partial \overline{u'u'}}{\partial x}+\frac{\partial \overline{u'v'}}{\partial y}+\frac{\partial \overline{u'w'}}{\partial z}\right]\\
\frac{\partial \overline{p}}{\partial y} &= -\frac{1}{RT}\left[\overline{u}\frac{\partial \overline{v}}{\partial x}+\overline{v}\frac{\partial \overline{v}}{\partial y}+\overline{w}\frac{\partial \overline{v}}{\partial z}+\frac{\partial \overline{u'v'}}{\partial x}+\frac{\partial \overline{v'v'}}{\partial y}+\frac{\partial \overline{v'w'}}{\partial z}\right]\\
\frac{\partial \overline{p}}{\partial z} &= -\frac{1}{RT}\left[\overline{u}\frac{\partial \overline{w}}{\partial x}+\overline{v}\frac{\partial \overline{w}}{\partial y}+\overline{w}\frac{\partial \overline{w}}{\partial z}+\frac{\partial \overline{u'w'}}{\partial x}+\frac{\partial \overline{v'w'}}{\partial y}+\frac{\partial \overline{w'w'}}{\partial z}\right]
\end{aligned}
\tag{5.4}
$$

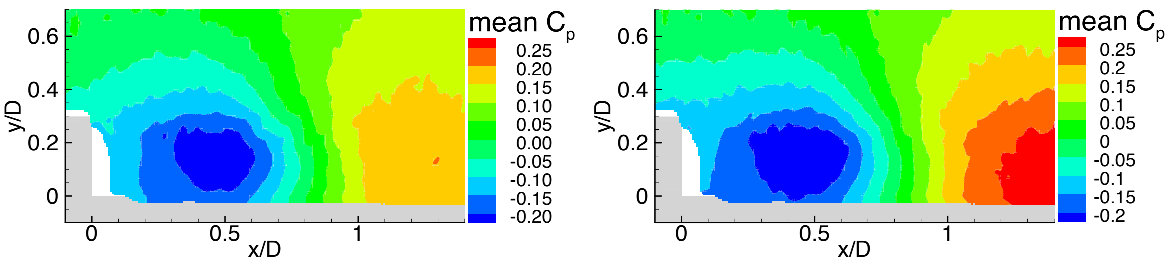

(a) Planar PIV

(b) Tomographic PIV

Figure 5.17: Contour plots of mean C_p

Tomographic to planar PIV

The planar PIV formulation is seen in equation 5.5 in which all out-of-plane velocity, w components, and derivatives thereof, are eliminated. The resulting coefficient of pressure along the central plane using the planar PIV formulation is visible in Figure 5.17(a). This result would essentially be identical to an artificial stereo PIV result created by only eliminating the out-of-plane derivatives. Additionally, both the tomographic and planar formulations are shown without their respective Reynolds stress terms and spatial density gradient terms are added to asses their effect.

$$
\begin{aligned}
\frac{\partial \overline{p}}{\partial x} &= -\frac{1}{RT}\left[\overline{u}\frac{\partial \overline{u}}{\partial x}+\overline{v}\frac{\partial \overline{u}}{\partial y}+\frac{\partial \overline{u'u'}}{\partial x}+\frac{\partial \overline{u'v'}}{\partial y}\right]\\
\frac{\partial \overline{p}}{\partial y} &= -\frac{1}{RT}\left[\overline{u}\frac{\partial \overline{v}}{\partial x}+\overline{v}\frac{\partial \overline{v}}{\partial y}+\frac{\partial \overline{u'v'}}{\partial x}+\frac{\partial \overline{v'v'}}{\partial y}\right]
\end{aligned}
\tag{5.5}
$$

Comparison of 2C and 3C formulations

In Figures 5.17(b) and 5.17(a), when comparing the full 2C and 3C formulations, it can be seen that the contour plots show some dissimilarities; It follows from the two flow field

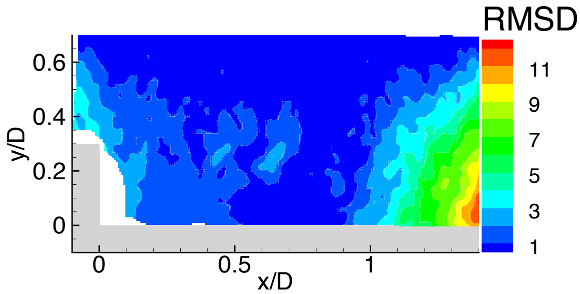

Figure 5.18: RMSD of planar and tomographic pressure reconstruction formulations

images that Figure 5.18 shows the global Root Mean Square Deviation (RMSD) for which the average deviation is 4.4%. The most notable difference is after the reattachment point where the RMSD grows to approximately 12%. Another slight deviation in the first half of the recirculation region presents a RMSD of 1.5%. Before reattachment, the agreement is very good with a RMSD of 0.8%. Figure 5.19 also shows both formulations compared to the pressure transducer measurements. Both the 2D2C and 3D3C formulations show good agreement with the pressure transducers, exhibiting the same difference seen in section 5.4.

RS term	$\frac{\partial \overline{u'u'}}{\partial x}$	$\frac{\partial \overline{u'v'}}{\partial y}$	$\frac{\partial \overline{u'w'}}{\partial z}$
global mean	0.48	-0.53	-1.30
stand. dev	3.84	3.33	1.53
RS term	$\frac{\partial \overline{u'v'}}{\partial x}$	$\frac{\partial \overline{v'v'}}{\partial y}$	$\frac{\partial \overline{v'w'}}{\partial z}$
global mean	-0.31	-0.26	0.14
stand. dev	1.34	0.95	0.36
RS term	$\frac{\partial \overline{u'w'}}{\partial x}$	$\frac{\partial \overline{v'w'}}{\partial y}$	$\frac{\partial \overline{w'w'}}{\partial z}$
global mean	-0.01	-0.01	0.03
stand. dev	1.34	0.37	1.39

Table 5.1: The global mean and standard deviation of the Reynolds stress terms; all values absolute ($\cdot 10^5$).

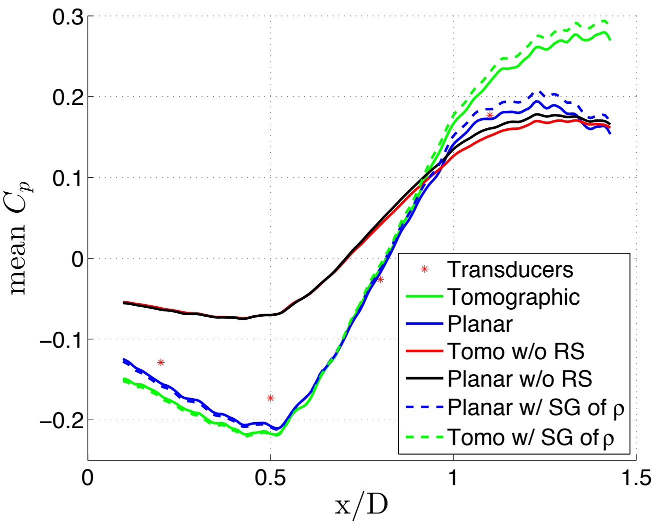

Figure 5.19: Coefficient of pressure of 2C and 3C formulations and pressure transducers

When comparing the 2C and 3C formulations with and without Reynolds stress terms (RS), it can be seen that said terms have the largest impact in the recirculation region; there, by excluding the terms, the largest discrepancy among the formulations is seen. This occurs across the streamwise distance with a high variation in Reynolds stress, as seen in Figure 5.10. In particular, the Reynolds stresses, $\overline{u'v'}$ and $\overline{w'w'}$, seen in Figures 5.10(a) and 5.10(b), respectively, cover a broad range and form the largest gradients of all Reynolds stresses behind the BFS. This large discrepancy, caused by the absence of the Reynolds stress terms, is because these nine (or four in the planar case) tensor stress components form the turbulent portion of the formulation (White, 2006). Modeling a turbulent flow field, such as the base of the BFS being studied, without such turbulent components will lead to an inaccurate result as can be seen in Figure 5.19. Because there is less difference between the planar and tomographic formulations without Reynolds stress terms, it can be concluded that these terms are responsible for the difference between the original 2C and 3C formulations.

As such, it is of interest to investigate which Reynolds stress terms have the largest effect on the pressure reconstruction. To this end, Table 5.1 shows the global mean and standard deviation of each term. Therein it can be seen that those contributing to the streamwise pressure gradient, $\partial\overline{p}/\partial x$ are the most significant. The Reynolds stress terms contributing to the radial pressure gradient, $\partial\overline{p}/\partial y$ are slightly smaller whereas those in the out-of-plane direction, $\partial\overline{p}/\partial z$ are a full order of magnitude smaller. All nine Reynolds stress terms can be seen in Appendix C.

As expected, the addition of the spatial gradient density terms (SG of ρ) does not strongly alter the mean C_p result because the flow is only mildly incompressible, resulting in relatively small density and temperature gradients; Both 3C and 2C formulations lie within 1% of the original. This justifies why these terms were omitted from the original formulation as seen in equation 5.4. The terms which were added to the original formulation are given in equation 5.6; note that equation 5.6 shows these terms for the tomographic formulation and that the planar formulation omits all out-of-plane velocity components and derivatives thereof. The resultant formulations with density spatial gradient terms seen in Figure 5.19 can be seen to very closely follow the original formulations. This is because of the aforementioned minimal density gradients in the flow and the small effect of these terms seen in equation 5.6.

$$
\begin{aligned}
\cdots \quad & \frac{1}{RT}\left[-\frac{\overline{u'u'}}{T}\frac{\partial T}{\partial x}-\frac{\overline{u'v'}}{T}\frac{\partial T}{\partial y}-\frac{\overline{u'w'}}{T}\frac{\partial T}{\partial z}\right]\\
\cdots \quad & \frac{1}{RT}\left[-\frac{\overline{u'v'}}{T}\frac{\partial T}{\partial x}-\frac{\overline{v'v'}}{T}\frac{\partial T}{\partial y}-\frac{\overline{v'w'}}{T}\frac{\partial T}{\partial z}\right]\\
\cdots \quad & \frac{1}{RT}\left[-\frac{\overline{u'w'}}{T}\frac{\partial T}{\partial x}-\frac{\overline{v'w'}}{T}\frac{\partial T}{\partial y}-\frac{\overline{w'w'}}{T}\frac{\partial T}{\partial z}\right]
\end{aligned}
\tag{5.6}
$$

Explanation of differences between 2C and 3C As described in section 2.1.2, the reattachment point is the region of the flow field that is expected to have the highest turbulence intensity. Regions which are more turbulent also have more out-of-plane, or three-dimensional, flow features. It follows then that the greatest differences between the 2C and 3C formulations is at those points where greater out-of-plane flow occurs. The tomographic 3C formulation takes these out-of-plane motions, w into account whereas the planar 2C formulation does not. As the Reynolds stress terms have their greatest influence in these highly turbulent regions, their omission leads to the greatest discrepancies in said region.

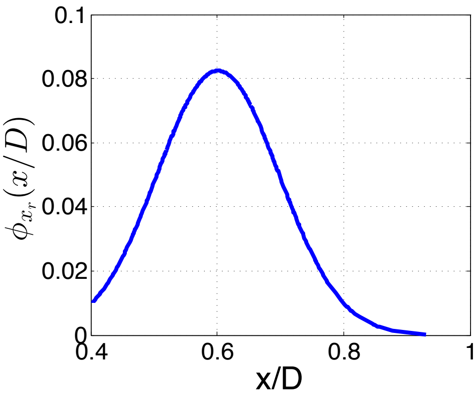

Figure 5.20: PDF of the reattachment location, x_r for Mach 1.5 case

5.5 Supersonic Case: Mean Flow Results

Shear layer reattachment location

As is discussed in section 2.3.2, the supersonic case features a shorted mean reattachment length, $\overline{x_r}/D = 0.6$. The minimum reattachment length is $x_{r_{\text{min}}}/D = 0.40$ and the maximum length is $x_{r_{\text{max}}}/D = 0.93$. The RMS of the deviation from the mean reattachment location is $x_{r_{\text{RMS}}} = 0.09$, which is lower than the value calculated for the Mach 0.7 case ($x_{r_{\text{RMS}}} = 0.12$). Additionally, the peak of the distribution reaches 0.08 whereas for the subsonic case this peak reached 0.065, approximately. From this it can be concluded that the reattachment length for the supersonic case shows slightly less variation when compared to the subsonic case. Figure 5.20 shows the plotted PDF distribution for the reattachment location, x_r.

In-flow boundary layer

Figure 5.21 shows the mean velocity field and profile for the boundary layer belonging to the supersonic case. For the Mach 1.5 case the boundary layer thickness was slightly larger, $\delta \approx 5.7$ mm or $\delta/D \approx 0.12$, compared to $\delta \approx 4.8$ mm or $\delta/D \approx 0.10$ for the subsonic case. As similarly observed by Scharnowski et al. (2016a), the supersonic case shows a more pronounced 'velocity overshoot' at the edge of the boundary layer than the subsonic case. When compared to the velocity profile of the subsonic case shown in Figure 5.7(b), the supersonic case displays a steeper velocity profile, which would indicate a more turbulent boundary layer. This follows logically in that the Reynolds number for the supersonic case is higher.

Mean velocity field

The supersonic PIV results are worth analyzing to better understand how the BFS flow field changes when transitioning to supersonic flow. The mean velocity components and the RMS

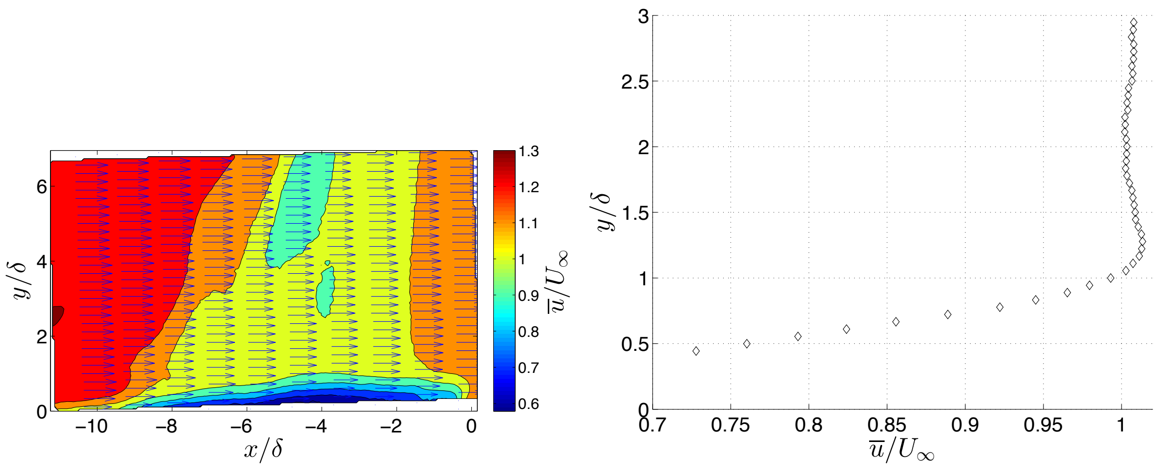

(a) mean velocity field

(b) velocity profile

Figure 5.21: Mean velocity field and velocity profile over model main body upstream of separation for Mach 1.5 case

of their fluctuating terms nicely resolve the topological flow features discussed in Chapter 2.

Figure 5.22 shows the three mean velocity components for the supersonic case at Mach 1.5. The freestream velocity, $U_\infty = 343.8$ m/s and quickly expands over the PME to a maximum velocity of $U = 449.3$ m/s. As is expected and discussed in section 2.3.2, the reattachment length is significantly reduced due to the flow downturn caused by the PME; the reattachment length is approximately $\overline{x_r}/D \approx 0.6$. Maximum backflow is $-0.22 \cdot U_\infty$ occurring in the recirculation region at $x/D = 0.41$. Topological flow field features are particularly visible in Figure 5.22(b) where the PME is visible at the edge of the BFS and a recompression shock is visible beyond the point of reattachment. Figure 5.22(c) shows similar out-of-plane velocity values to the subsonic case, which could imply a non-axisymmetric flow field or a slightly misaligned model.

Velocity statistics

The RMS of the velocity fluctuations appear to be more contained to a smaller recirculation region than the subsonic case. The maximum fluctuation in the streamwise direction is $0.21 \cdot U_\infty$ at $x/D = 0.58$ slightly upstream from the point of reattachment. In the radial direction, the maximum fluctuation is $0.14 \cdot U_\infty$ at $x/D = 0.26$, which is well within the recirculation region. In the out-of-plane direction, the maximum fluctuation is $0.19 \cdot U_\infty$ at $x/D = 0.86$, well downstream from the reattachment location. The PME emminating from the base of the BFS and the reattachment shock are visible in Figures 5.23(a) and 5.23(b), there they cause slightly higher RMS values due to their strong streamwise and radial velocity gradients. The reduced size of the high RMS regions, when compared to the subsonic case, demonstrate that the regions of highly unsteady motion are lower for the supersonic BFS

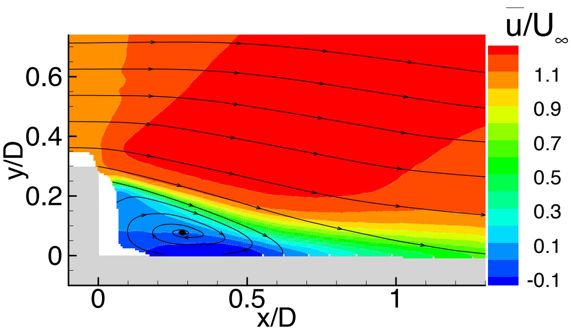

(a) Streamwise, $\overline{u}$

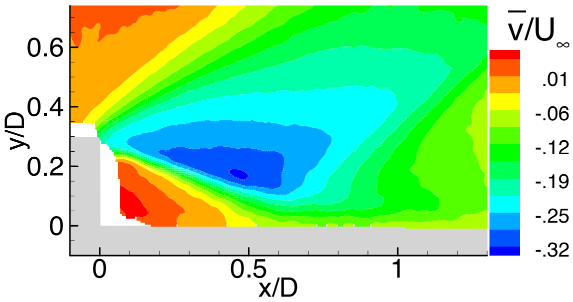

(b) Radial, $\overline{v}$

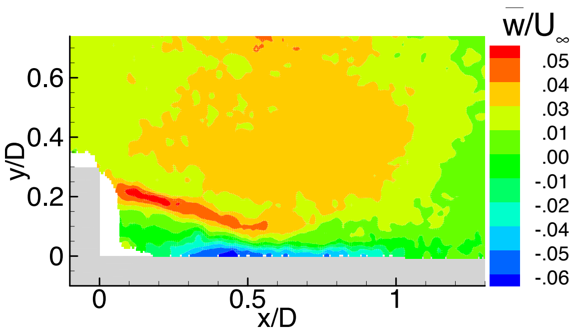

(c) Out-of-plane, $\overline{w}$

Figure 5.22: Mean velocity components for Mach 1.5 case

flows; the supersonic flow field, generally, appears to be quite steady.

Mean pressure

The PME which is a central topological feature in the resolved flow field is an isentropic feature; as such, the pressure reconstruction can still be performed but due to the presence of shockwaves, the total pressure is no longer that which was set in the settling chamber. To account for this, the Mach number upstream, M_1 of the shockwave is found based on the Mach angle, μ in the schlieren images; this also allows for the calculation of the flow deflection angle, θ using equation 5.7. The Mach number downstream of the oblique shockwave is calculated using equation 5.8. The ratio of total pressure upstream and downstream, $p_{0,1}/p_{0,2}$ is calculated using these Mach numbers, M_1 and M_2, and angles in equation 5.9. By this approach, the total pressure ratio is $p_{0,2}p_{0,1} = 0.99$, the flow deflection angle is approximately zero, and the Mach number downstream of the oblique shockwave is $M_2 = 1.324$, which lends

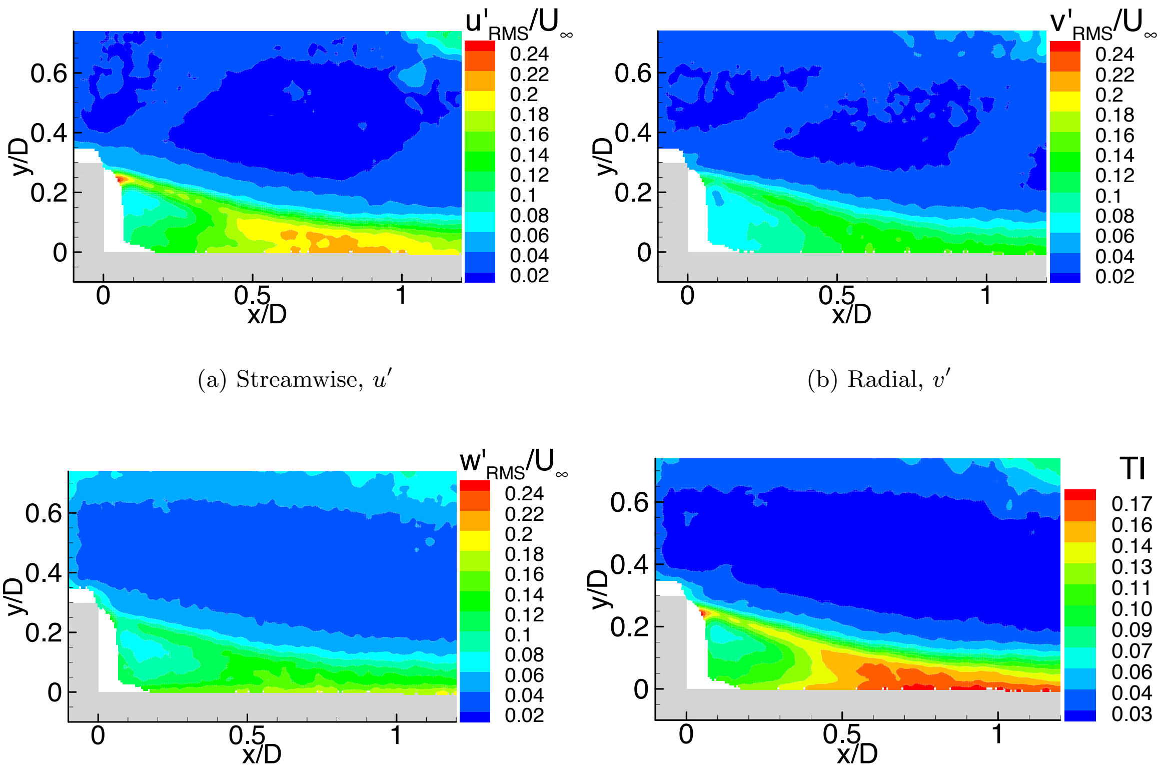

(a) Streamwise, u'

(b) Radial, v'

(c) Out-of-plane, w'

(d) Turbulence Intensity

Figure 5.23: RMS of velocity fluctuations and turbulence intensity for Mach 1.5 case

sufficient information to perform the pressure reconstruction.

$$\cot(\theta) = \tan(\mu)\left(\frac{(\gamma+1)M_1^2}{2(M_1^2\sin^2(s)-1} - 1\right) \tag{5.7}$$

$$M_2^2\sin^2(\mu-\theta) = \frac{(\gamma-1)M_1^2\sin^2(\mu)+2}{2\gamma M_1^2\sin^2(\mu)-(\gamma-1)} \tag{5.8}$$

$$\frac{p_{0,2}}{p_{0,1}} = \left(\frac{(\gamma+1)M_1^2\sin^2(\mu)}{(\gamma-1)M_1^2\sin^2(\mu)+2}\right)^{\frac{\gamma}{\gamma-1}}\left(\frac{\gamma+1}{2\gamma M_1^2\sin^2(\mu)-\gamma+1}\right)^{\frac{1}{\gamma-1}} \tag{5.9}$$

The resulting coefficient of pressure is seen in Figure 5.24. It can be seen that pressure is far lower than the subsonic case and this is to be expected due to the higher Mach number. A large pressure drop is exhibited over the PME where the flow accelerates to approximately $U_\infty \approx 450$ m/s. Thereafter, the flow decelerates over the oblique shockwave and the C_p begins to rise. The shockwave is not an isentropic feature and this brings into disrepute the validity

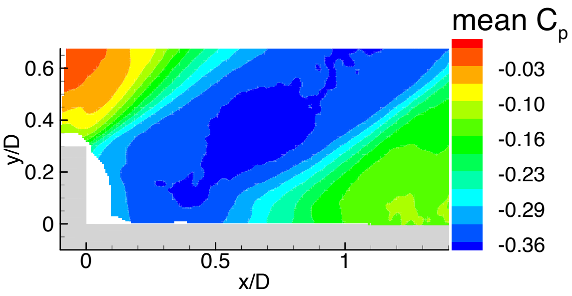

Figure 5.24: Mean C_p for Mach 1.5 case

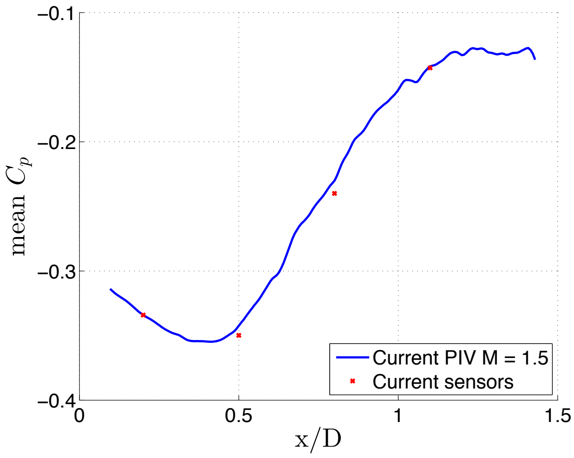

Figure 5.25: Comparison of mean C_p to pressure transducers for Mach = 1.5

of the supersonic pressure reconstruction. In comparison to the pressure transducers there is very good agreement, as seen in Figure 5.25. Due to a lack of literature on supersonic pressure in the wake of a BFS, further comparison is not made.

5.6 Intermediate Conclusions

Based on the results presented in this section, it has been demonstrated that the system makes quantitative flow field analysis possible. The mean flow field, based on 500 image pairs, is nicely converged; the Reynolds stress terms are the slowest to converge. At the tested Reynolds numbers, the incoming boundary layer is fully turbulent and due to similar test parameters, is also expected to be turbulent in the second experimental campaign. The mean reattachment location is near $L/D = 1.0$, which follows from the discussion in section 2.1.2.

Changes in spanwise flow variables are small and do not necessarily lend additional insight, except when performing a pressure reconstruction; in such cases, it has been shown that results are more accurate when also considering out-of-plane components. The pressure reconstruction shows good agreement with both the sting mounted pressure transducers and literature. Through the additional supersonic results, it is clear that the PIV system used herein is capable of resolving supersonic flow features.

The steady flow features that were discussed in Chapter 2 are nicely resolved by the PIV system. Additionally, instances of the unsteady motion are also visible in individual snapshots as presented in section 5.3. Now the work can shift focus to answering the research question at hand. In the following chapter, the results of the second experimental campaign will be discussed.

Chapter 6

Influence of Exhaust Plume and Nozzle Length

The following chapter presents the results of the effects of the exhaust plume and varying nozzle length. As mentioned previously, it was originally intended to test at both sub- and supersonic Mach numbers. Schlieren visualization results are provided for subsonic and supersonic conditions. PIV data are only provided for the subsonic case due to time constraints upon discovering that the TST-27 would not properly 'start' at the set supersonic conditions. As the first experimental campaign presented in Chapter 5 dealt primarily with familiarization of the flow field and validation of the methods used to study it, the results presented in this chapter will serve to answer the research questions at hand.

6.1 Schlieren Results

For the second experimental campaign, the presence of the exhaust plume affects the topological flow features of interest. Based on the reasoning presented in section 5.1, that vertical gradients gave more insight into relevant shear and boundary layers, the second experimental campaign used a horizontal schlieren knife exclusively; as such, all schlieren images presented in this section show vertical density gradients. The results presented herein were used to test the effect of varying jet pressure, $p_{0,\text{jet}}$, total pressure, p_0, freestream Mach number, M_∞, and nozzle length, L/D; the effects of these changes will be discussed.

Table 6.1 shows the experimental matrix and the resultant nozzle pressure ratio (NPR) values for each of the cases shown herein. The NPR is defined as the ratio between the total pressure of the jet and the freestream pressure, NPR $= p_{0,\text{jet}}/p_\infty$. Calculation p_{jet} is based on the expansion of the flow to Mach 4.1 at the nozzle exit. Changes in the NPR can also been seen in the size and shape of the exhaust plume.

M_∞	p_0 [bar]	p_∞ [bar]	$p_{0,jet}$ [bar]	p_{jet} [bar]	NPR
2.0	2.0	0.256	100	0.578	390
2.0	3.0	0.383	100	0.578	261
2.0	3.0	0.383	15	0.87	39
2.0	3.0	0.383	25	0.145	65
0.7	2.0	1.44	58	0.335	40
0.7	1.5	1.08	100	0.578	93

Table 6.1: NPR values calculated for the schlieren cases

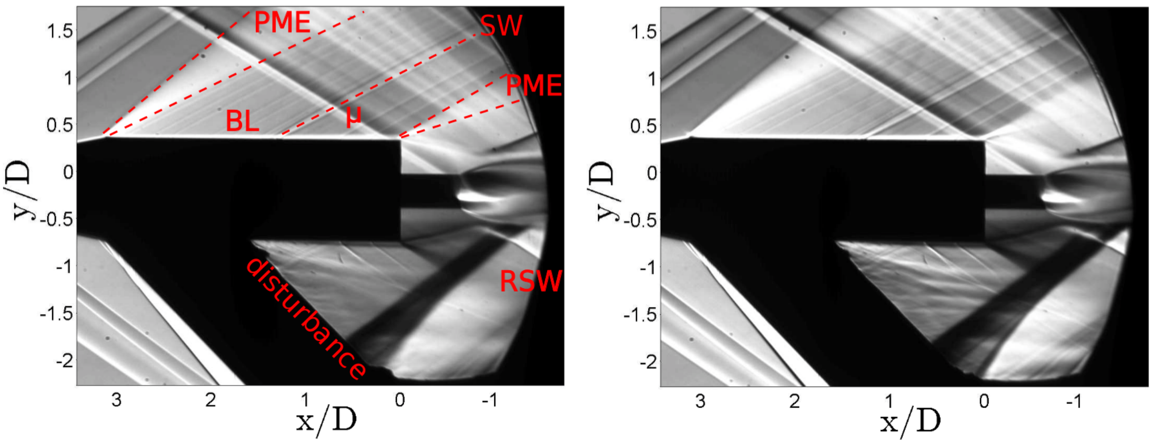

(a) $p_0 = 2.0$ bar (b) $p_0 = 3.0$ bar

Figure 6.1: Schlieren mean flow field results at Mach $= 2.0$ with varied total pressure and $p_{0,\text{jet}} = 100$ bar for $L/D = 0.6$ configuration

Figure 6.1 shows the shortest nozzle configuration ($L/D = 0.6$) in a supersonic Mach 2.0 flow. The same features that were present in experimental campaign I are present but their interaction with the exhaust plume is new. First, there are shockwaves reflected off of the tunnel walls, these originate at the nose of the model. At the interface of the nose and main body, the wall turns away from the flow and the first PME is seen. A boundary layer (BL) can be seen developing over the body. As the flow reaches the edge of the BFS, the sudden increase in cross-sectional area brings the presence of a second PME. The PME causes the separated shear layer, also emanating from the edge of the BFS to turn sharply downward. Upon impinging on the exhaust plume, a recompression shock (RSW) can be seen that forms near the top of the exhaust plume. These features are evident independent of total pressure, p_0.

Though a large increase in NPR is calculated, the increase in total pressure, p_0 does not seem to affect the size of the exhaust plume, which is underexpanded in Figure 6.1(a) and similarly underexpanded in Figure 6.1(b). The nozzle is underexpanded in both cases due to the jet pressure, $p_{0,\text{jet}} = 100$ bar which is significantly higher than the freestream pressure, p_∞. In both cases the wind tunnel is operated at Mach $= 2.0$, therefore the isentropic pressure ratio, p_∞/p_0 remains constant, which leads to a higher p_∞ for the case where $p_0 = 3.0$ bar.

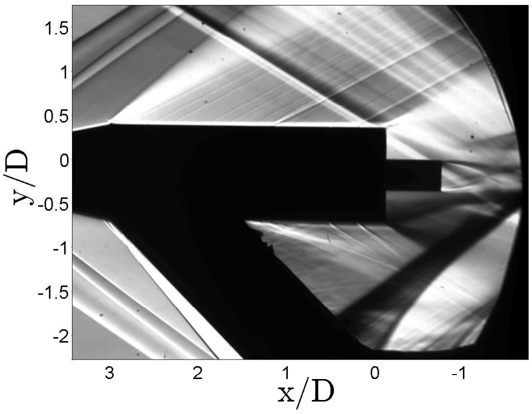

Figure 6.2: Schlieren mean flow field results at Mach 2.0 with $p_0 = 3.0$ bar and $p_{0,\text{jet}} = 15.0$ bar for $L/D = 0.6$ configuration

Therefore, the ratio between $p_{0,\text{jet}}$ and p_0 is smaller when $p_0 = 3.0$ bar, which leads to a slightly less underexpanded nozzle. Figure 6.2 shows that these effects are still present when the jet pressure is significantly reduced to $p_{\text{jet}} = 15.0$ bar, though there are some differences. Most notable is that the density gradient due to the recompression shockwave appears less than the cases where $p_{0,\text{jet}} = 100$ bar. This is due to the fact that when $p_{0,\text{jet}} = 15.0$ bar, the exhaust plume is not nearly as underexpanded, as indicated by the decreased NPR, which leads to the shear layer being deflected at a less severe angle, resulting in a weaker recompression shockwave.

For the case where $L/D = 1.8$, the recompression shock is seen to occur upstream of the exhaust nozzle in a case of solid reattachment. It can also be seen that the increased Mach number, M, when compared to the first experimental campaign, has led to a decreased Mach angle, μ in all aforementioned supersonic cases. Using the same method as outlined in section 5.1 by equation 5.1, with a Mach angle of approximately 28°, the apparent Mach number, $M \approx 2.13$. This longest case where $L/D = 1.8$ is most similar to the sting mounted model used in the first experimental campaign. Additionally, a disturbance can be seen beneath the model, which is caused by the presence of the mount affixed to the model.

As in the first experimental campaign, the subsonic flow shows a thinner boundary layer than the supersonic flow. Due to the lower Mach number, the isentropic pressure ratio, p_∞/p_0 leads to a higher freestream pressure, p_∞, which is evident by the reduced size of the exhaust plume; the exhaust is not as underexanded as the supersonic case seen in Figure 6.1 which used the same $p_{0,\text{jet}}$ pressure. This is quantified as a reduced NPR value for the subsonic cases as the ratio between p_{jet} and p_∞ is decreased. The shear layer which emanates from the edge of the BFS is seen to impinge upon the exhaust plume, as expected. Furthermore, the image displayed in Figure 6.4(b), where $p_0 = 1.5$ bar and $p_{0,\text{jet}} = 100.0$ bar, represents the operating parameters for which all remaining experiments were conducted.

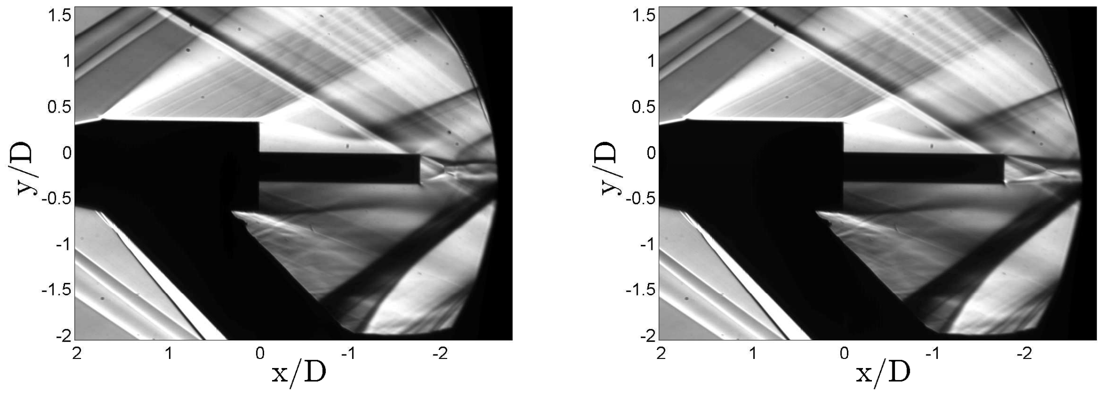

(a) $p_{\text{jet}} = 15.0$ bar

(b) $p_{\text{jet}} = 25.0$ bar

Figure 6.3: Schlieren mean flow field results at Mach = 2.0, $p_0 = 3.0$ bar with varied jet pressure for $L/D = 1.8$ configuration

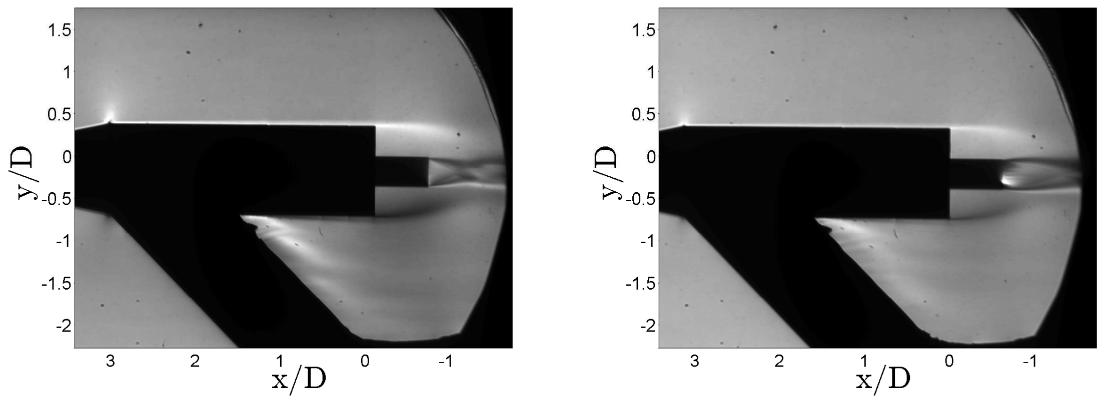

(a) $p_0 = 2.0$ bar, $p_{\text{jet}} = 58.0$ bar

(b) $p_0 = 1.5$ bar, $p_{\text{jet}} = 100.0$ bar

Figure 6.4: Schlieren mean flow field results at Mach = 0.7 with varied jet pressure and total pressure for $L/D = 0.6$ configuration

6.2 PIV Results

Shear layer reattachment location

The method used to find the reattachment location was the same as that used in section 5.3 for the first experimental campaign. Figure 6.5 shows the PDF distribution for the reattachment location for all cases except those with length, $L/D = 0.6$; in that case, the shear layer was found to always impinge within the plume and, as such, did not really have a 'reattachment location' per definition. The minimum, maximum, and mean reattachment lengths, x_r for the solid (L/D = 1.8) and hybrid (L/D = 1.2) cases are shown in Table 6.2. Also shown in the table is the RMS of the deviation from the mean for the reattachment length; for the sting mounted model this value was 0.12. There appears to be little variation caused by either the presence of the jet or the length of the nozzle. Furthermore, the minimum x_r for all cases is slightly closer to the base when compared to the sting mounted model and features a slightly increased statistical instability.

Additionally, Figure 6.5 shows that the hybrid case predominantly features solid reattachment as opposed to fluidic reattachment. This is in agreement with what is described by Gentile et al. (2016); an additional 10 mm spacer ring would make the length of the hybrid case coincide with the mean reattachment length, x_r. It is recommended that future investigations consider this case as truly being 'hybrid'.

Correlation with backflow Using the same approach as was used previously, Table 6.3 shows that the model used in the second experimental campaign featured a reduced correlation coefficient between the reattachment location and the maximum backflow. It can be seen that the fluidic and solid reattachment cases both feature a correlation coefficient of about -0.2. Variation is seen in the hybrid case with and without jet. This difference appears to show that the presence of the jet has a noticeable affect on the correlation within the unsteady flow dynamics in the wake of the model.

(x/D)	L/D = 1.2 w/ jet	L/D = 1.2 w/o jet	L/D = 1.8 w/ jet	L/D = 1.8 w/o jet
min	0.37	0.43	0.42	0.49
max	1.25	1.26	1.31	1.26
mean	0.91	0.94	0.97	0.98
RMS	0.13	0.14	0.14	0.13

Table 6.2: Reattachment location for hybrid and solid cases

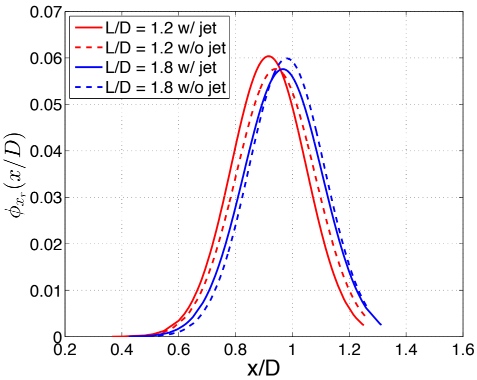

Figure 6.5: PDF of the reattachment length, x_r as x/D for varying L/D cases

	L/D = 0.6 w/ jet	L/D = 0.6 w/o jet	L/D = 1.2 w/ jet	L/D = 1.2 w/o jet	L/D = 1.8 w/ jet	L/D = 1.8 w/o jet
corr. coeff.	-0.20	-0.20	-0.15	-0.24	-0.20	-0.22

Table 6.3: Correlation coefficient for reattachment location and maximum backflow for all cases

Mean streamwise velocity

Figures 6.6, 6.7, and 6.8 show the mean streamwise velocity, $\overline{u}$ for each of the six cases; all figures share the same colorbar for the sake of comparison. It appears as though there is little variation between each of the individual cases seen in the figures. Table 6.4 shows the maximum backflow and its location for each of the six cases. Compared to the sting mounted model, which had a max backflow of $-0.33 \cdot U_\infty$ at $x/D = 0.51$ (see section 5.4), the maximum backflow for all cases herein appears to be fairly similar although slightly reduced. Location of maximum backflow is in the same vicinity with the $L/D = 1.2$ configuration showing a location approximately 10% closer to the base.

According to the PDF shown in Figure 6.5, the 'hybrid' reattachment case predominantly features solid reattachment with occasional cases of fluidic reattachment. The mean reattachment location at approximately $x/D = 1.0$ is in accordance with Gentile et al. (2016) for axisymmetric BFS flows. As such, it is expected that the $L/D = 1.2$ case will bear more resemblance to the longer, solid reattachment case, $L/D = 1.8$. Mean velocity of the streamwise component for the $L/D = 1.8$ length is shown in Figure 6.8. There is no discernible difference between the two cases, both qualitatively or of such magnitude to fall outside of the margin of uncertainty. Compared to the other reattachment cases, with or without exhaust

	L/D = 0.6 w/ jet	L/D = 0.6 w/o jet	L/D = 1.2 w/ jet	L/D = 1.2 w/o jet	L/D = 1.8 w/ jet	L/D = 1.8 w/o jet
vel. $[\overline{u}/U_\infty]$	-0.33	-0.31	-0.29	-0.32	-0.29	-0.32
loc. [x/D]	0.49	0.50	0.44	0.47	0.56	0.54

Table 6.4: Maximum backflow value and location for all cases

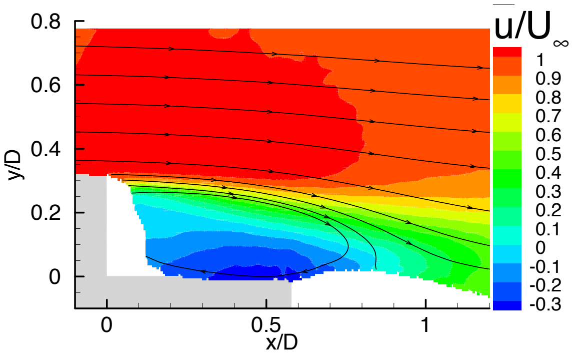

(a) $L/D = 0.6$ w/ jet

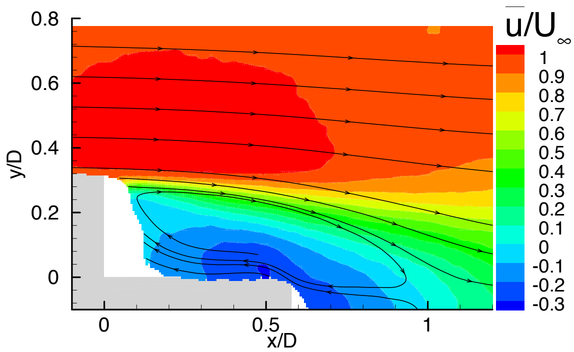

(b) $L/D = 0.6$ w/o jet

Figure 6.6: Mean streamwise velocity component, $\overline{u}$ for $L/D = 0.6$ case

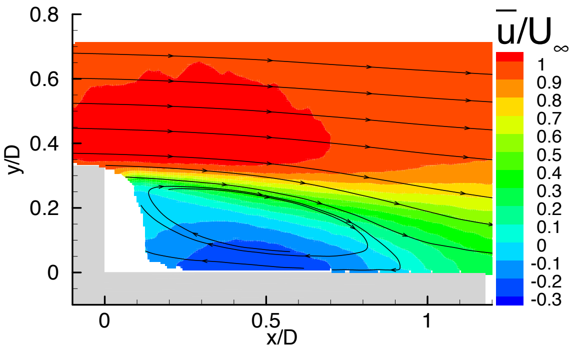

(a) $L/D = 1.2$ w/ jet

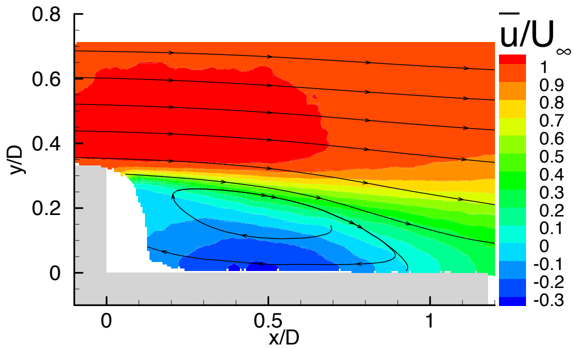

(b) $L/D = 1.2$ w/o jet

Figure 6.7: Mean streamwise velocity component, $\overline{u}$ for $L/D = 1.2$ case

plume, there is no noticeable difference.

Velocity statistics

The RMS of the radial velocity fluctuations are shown for all six cases in Figures 6.9, 6.10, and 6.11. Additionally, Table 6.5 shows the minimum, maximum, and mean radial velocity fluctuation for each of the cases. Compared to the sting mounted model, discussed in section 5.4, the largest fluctuations are greater but do not appear to follow a discernible trend.

Figure 6.9 shows the RMS values for the $L/D = 0.6$ case. The RMS values appear to be higher in the case without the exhaust plume. That is to say that, statistically, the flow field exhibits fewer unsteady fluctuations in the radial velocity component than the case without an exhaust plume. This could allude to a stabilizing factor imparted by the presence of the jet; the difference is a 21% reduction in mean velocity fluctuation value as seen in Table 6.5.

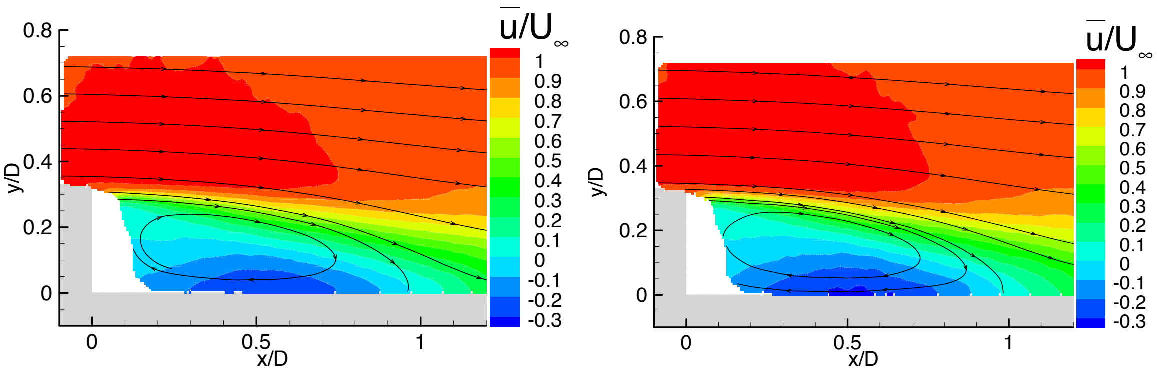

(a) $L/D = 1.8$ w/ jet

(b) $L/D = 1.8$ w/o jet

Figure 6.8: Mean streamwise velocity component, $\overline{u}$ for $L/D = 1.8$ case

	L/D = 0.6 w/ jet	L/D = 0.6 w/o jet	L/D = 1.2 w/ jet	L/D = 1.2 w/o jet	L/D = 1.8 w/ jet	L/D = 1.8 w/o jet
min	2.2	2.2	1.9	1.9	2.2	1.6
max	22.6	30.0	27.9	24.2	20.6	21.3
mean	9.1	11.3	10.2	10.5	8.5	8.3
$x_{\mathbf{max}}/D$	1.21	1.11	1.21	1.27	1.15	1.02

Table 6.5: RMS of radial velocity fluctuations as percentage of U_∞ for all cases

As discussed in section 2.2.2, the finite nozzle length without an active exhaust plume gives rise to an additional recirculation region at the nozzle exit, which could be the cause for the increased instability.

The RMS of the radial velocity fluctuations show the greatest values in the $L/D = 1.2$ case with exhaust plume. This is a significant result because the greatest development in Reynolds normal stresses are found for the same case. This lends credence to the finding that the $L/D = 1.2$ case with an exhaust plume feature the greatest amount of turbulent mixing in the wake of the BFS.

The RMS of the velocity fluctuations for the solid reattachment length case are shown in Figure 6.11. The velocity fluctuation RMS shows the lowest mean value of all length cases at $0.083 \cdot U_\infty$ and the presence of the jet does little to change that $(0.083 \cdot U_\infty)$. As with the hybrid case, there could be an inherent unsteadiness in a finite afterbody without exhaust plume as discussed in Chapter 2. Due to the inability of the present experimental arrangement to capture the end of the nozzle for the solid reattachment case, the statistical turbulence could be reduced.

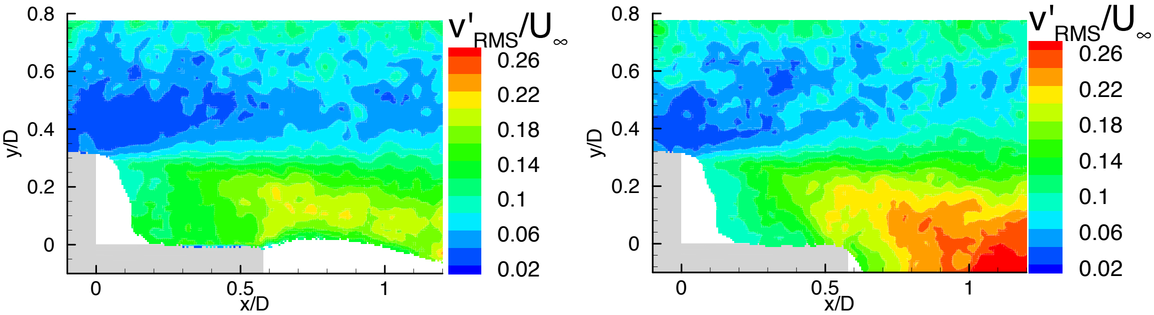

(a) $L/D = 0.6$ w/ jet (b) $L/D = 0.6$ w/o jet

Figure 6.9: RMS of the radial velocity fluctuations, v' for $L/D = 0.6$ case

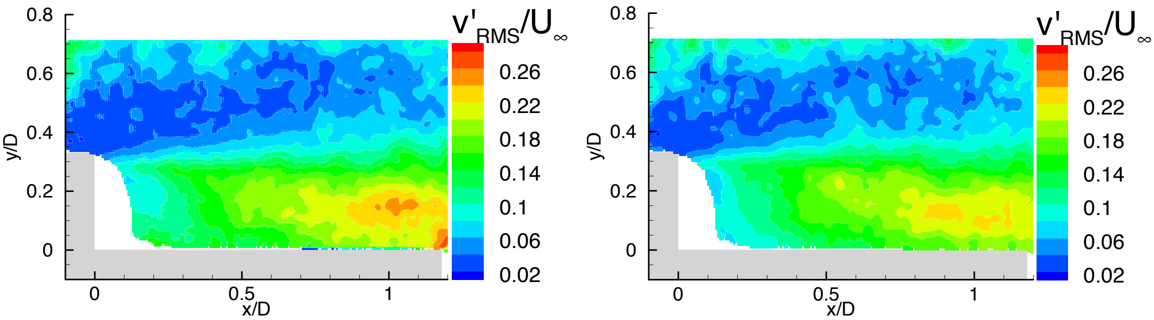

(a) $L/D = 1.2$ w/ jet (b) $L/D = 1.2$ w/o jet

Figure 6.10: RMS of the radial velocity fluctuations, v' for $L/D = 1.2$ case

Mean pressure

The mean pressure, C_p values for all cases are shown in Table 6.6; therein it can be seen that the presence of the jet only creates a notable difference in mean pressure during the fluidic reattachment of the $L/D = 0.6$ nozzle length. This is attributed to the 'jet-suction' effect as described by Deprés et al. (2004) and is absent from all other nozzle length cases. Additionally, the variation in the location of minimum C_p does not vary much from the expected location of $x/D = 0.5$.

Figure 6.12 shows a comparison of the fluidic reattachment case with and without jet presence. Figure 6.12(c) shows the wall pressure on the nozzle, therefore this data only stretches to the end of the nozzle at $x/D = 0.6$. Most significant from the result is that the PIV based pressure reconstruction has captured the 'jet-suction' effect as described by Deprés et al. (2004). This is noticed by the nearly constant difference between the cases with and without exhaust jet. Compared to the pressure transducer results from Deprés et al. (2004), also visible in Figure 6.12(c), the difference between the two cases is not as large. Data points from Deprés et al. (2004) show an approximate drop in C_p of 0.1 (71% change) whereas the present results show

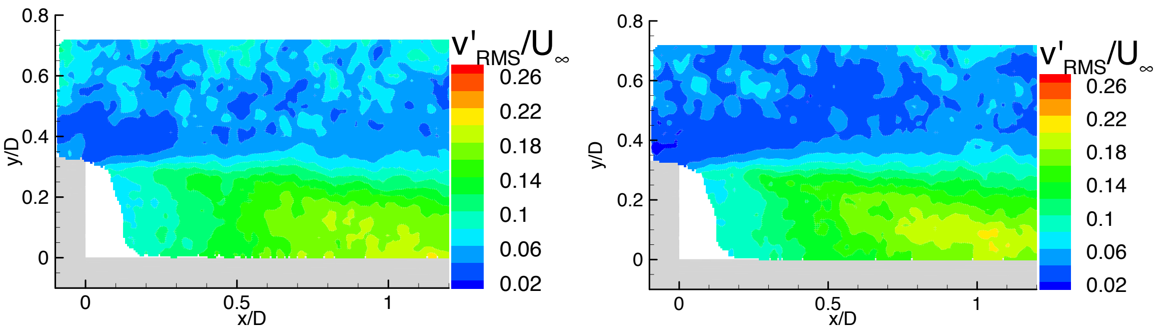

(a) $L/D = 1.8$ w/ jet

(b) $L/D = 1.8$ w/o jet

Figure 6.11: RMS of the radial velocity fluctuations, v' for $L/D = 1.8$ case

Wall C_p ($x/D \leq 0.6$)	L/D = 0.6 w/ jet	L/D = 0.6 w/o jet	L/D = 1.2 w/ jet	L/D = 1.2 w/o jet	L/D = 1.8 w/ jet	L/D = 1.8 w/o jet
mean	-0.19	-0.16	-0.17	-0.17	-0.17	-0.16
min.	-0.21	-0.18	-0.18	-0.17	-0.17	-0.19
loc. [x/D]	0.49	0.50	0.44	0.47	0.56	0.54

Table 6.6: C_p min and mean values and location for all cases

a consistent decrease of approximately 0.04 (22% change). Jet results from Deprés et al. (2004) use an NPR = 33 and test a range of NPR values (NPR = 8.3, 12.4, and 32.4). It is noted that the difference caused by the jet-suction effect increases with increasing NPR. Therefore, it would have been expected that the difference seen in the present experiment using NPR $\approx$ 100 would be larger.

The 'jet-suction' effect that was captured for the short nozzle length is absent from the hybrid case; this is to be expected according to Deprés et al. (2004) because its occurrence is dependent upon fluidic reattachment. In Table 6.6 it can be seen that the mean pressure for the $L/D = 1.2$ case is lower than that of the shorter, $L/D = 0.6$ case; this is also in agreement with Deprés et al. (2004). There is however poor agreement in the C_p values when comparing the present measurements with those of Deprés et al. (2004). Though the two measurements show better agreement close to the base and in the recirculation region, there is an approximate deviation of 0.1 toward the point of reattachment.

Figures 6.14(a) and 6.14(b) show C_p over the field of view with little difference between the two solid reattachment cases. Figure 6.14(c) shows a comparison of the wall pressure to results for a long afterbody (L >> D) case from Deprés et al. (2004). There is little difference between either the complete field of view or the pressure along the nozzle and both cases feature good agreement with the literature; both average RMSD of 3% across the length of the nozzle. There is a slight decrease in pressure in the recirculation region for the case without the jet, this is visible in the darkened area in Figure 6.14(b) and the lower value near $x/D = 0.5$ in Figure 6.14(c).

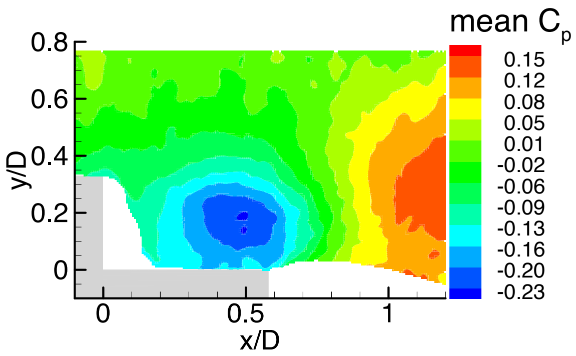

(a) $L/D = 0.6$ w/ jet

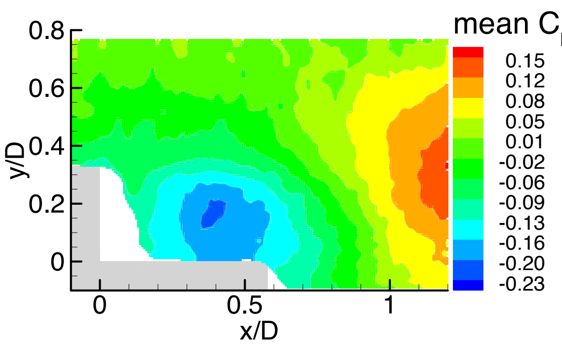

(b) $L/D = 0.6$ w/o jet

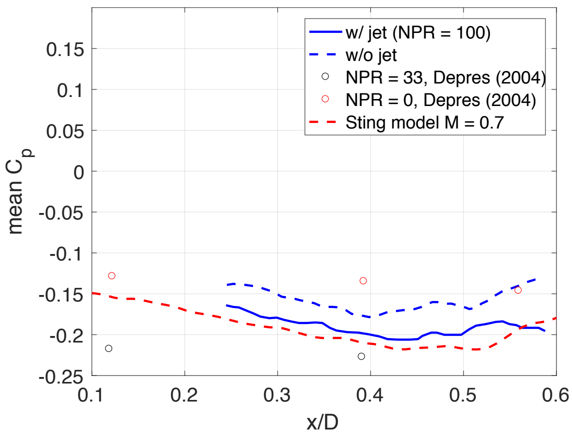

(c) Comparison

Figure 6.12: Mean C_p for $L/D = 0.6$ case

Compared to the sting mounted model, the jet equipped model appears to show a more shallow pressure gradient in the streamwise direction. For the sting mounted model, the gradient value was $dC_p/dx \approx 0.5$ whereas for the jet equipped model this is approximately $dC_p/dx \approx 0.35$. Generally, the datasets are in good agreement; all results are of the same order.

Mixing layer

Streamwise velocity development

The streamwise velocity development for each of the nozzle lengths can be seen in Figures 6.15, 6.17, and 6.19. There appears to be little variation caused by the presence or absence of the jet. Evidence of the jet can be seen in the lower portion of Figure 6.15 where the velocity profile near the exhaust appears to be accelerated at lower heights. Furthermore, each of the

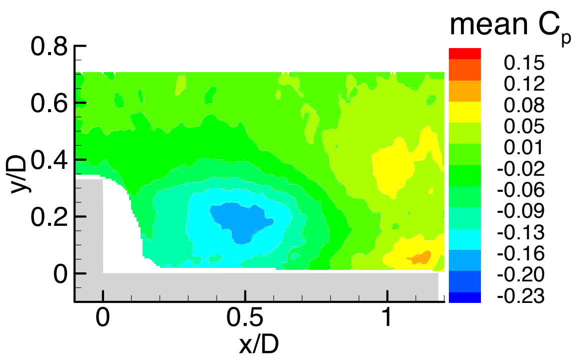

(a) $L/D = 1.2$ w/ jet

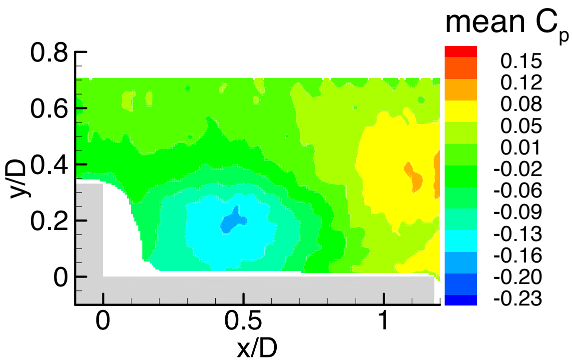

(b) $L/D = 1.2$ w/o jet

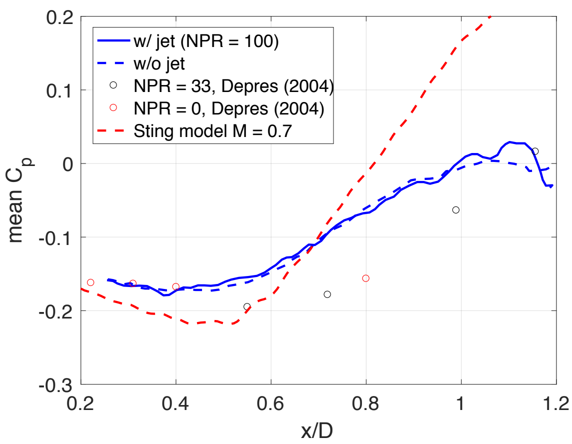

(c) Comparison

Figure 6.13: Mean C_p for $L/D = 1.2$ case

streamwise stations appears to show a similar velocity profile regardless of the given nozzle length. Stations further downstream do appear to show a slightly larger difference between the jet and non-jet cases, especially for the $L/D = 1.2$ case seen in Figure 6.17, which could be attributed to the increased streamwise velocity due to the jet. For the $L/D = 1.8$ the jet is so far downstream that it no longer influences the wake of the BFS in the FOV.

The streamwise velocity development for the hybrid case is shown in Figure 6.17. Generally, there appears to be little variation caused by the presence of the exhaust plume, though the small deviation seen in Figure 6.15 caused by the jet is absent. There does appear to be a small increase in streamwise velocity at the last station, which could be caused by its proximity to the nozzle exit. Figure 6.19 shows the streamwise velocity development of the solid reattachment configuration. As with all other cases, there is little effect imparted by the jet. Upon moving downstream, the growth of the shear layer is evident by the reduction in gradient in the velocity.

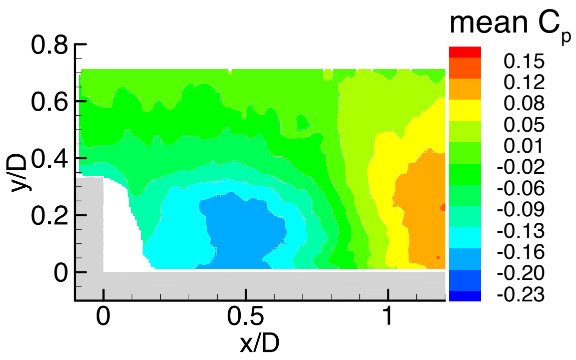

(a) $L/D = 1.8$ w/ jet

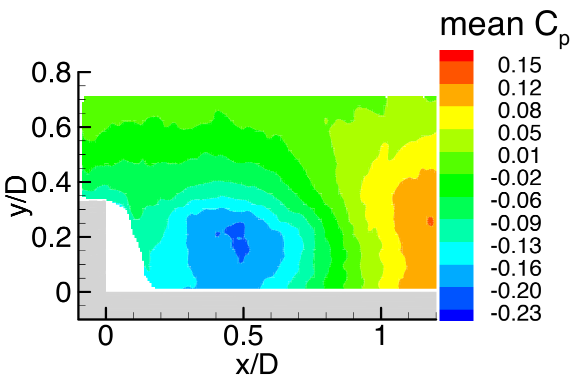

(b) $L/D = 1.8$ w/o jet

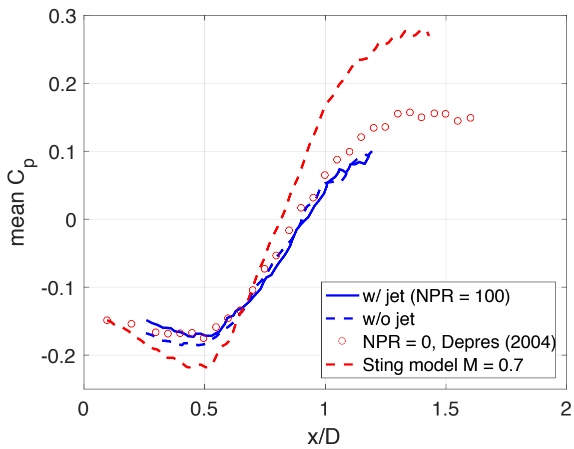

(c) Comparison

Figure 6.14: Mean C_p for $L/D = 1.8$ case

Streamwise vorticity thickness

Figures 6.16, 6.18, and 6.20 show each of the three length cases compared to the sting mounted model and several results from literature. The numerical ZDES results by Deck and Thorigny (2007) used a plume-equipped model of length, $L/D = 1.2$ with an NPR ≈ 34 ($Re_D \approx 1.1 \cdot 10^6$). Schrijer et al. (2014) used PIV om the same model used herein, but without an exhaust plume at $Re_D = 1.3 \cdot 10^6$. Additional numerical ZDES results from Pain et al. (2014) also used an exhaust plume equipped model tested at $Re_D = 1.2 \cdot 10^6$. Recall that for the measurements of the second experimental campaign, $Re_D = 1.0 \cdot 10^6$.

The results for the transonic sting mounted model show a greater vorticity thickness offset before the point of reattachment due to the spatial resolution. That is to say, all of the present experiments show negligibly lower vorticity thicknesses in the separated shear layer and recirculation regions. In this region, all length cases feature a streamwise development,

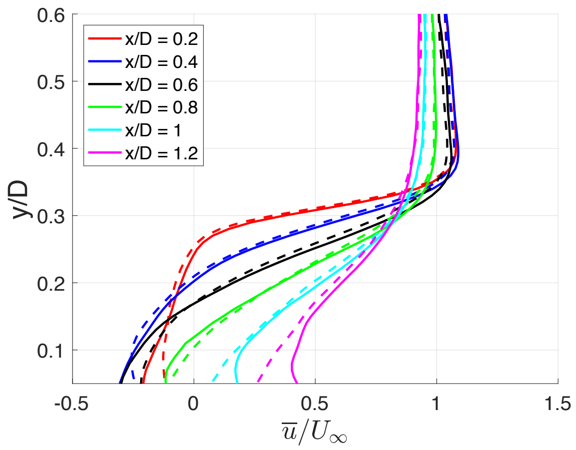

Figure 6.15: Streamwise velocity development for $L/D = 0.6$ case; solid line (with jet) and dashed line (without jet)

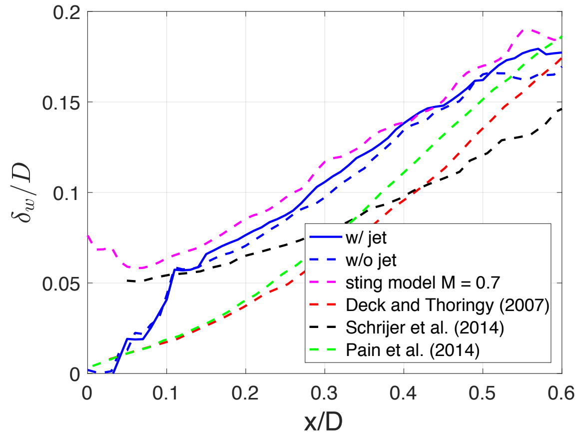

Figure 6.16: Streamwise vorticity thickness development for $L/D = 0.6$ case; solid line (with jet) and dashed line (without jet)

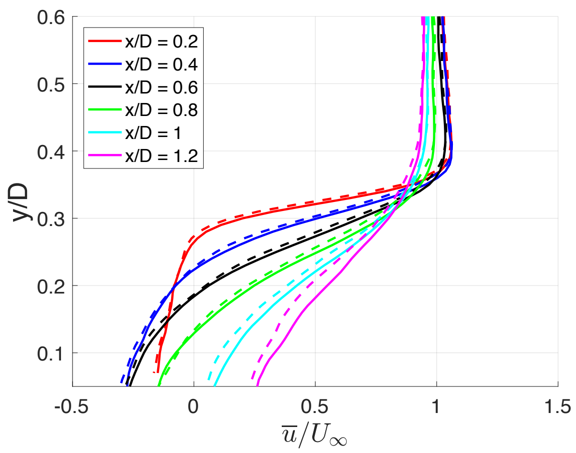

Figure 6.17: Streamwise velocity development for $L/D = 1.2$ case; solid line (with jet) and dashed line (without jet)

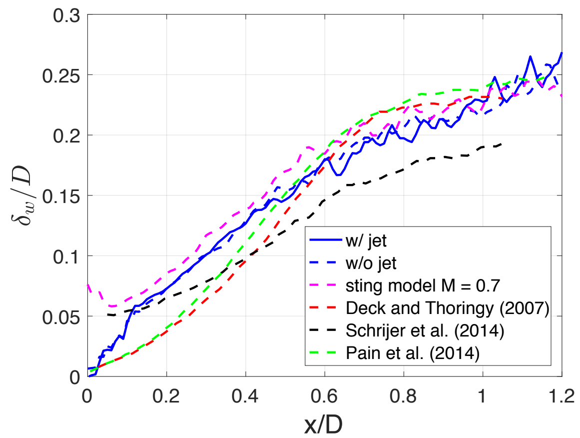

Figure 6.18: Streamwise vorticity thickness development for $L/D = 1.2$ case; solid line (with jet) and dashed line (without jet)

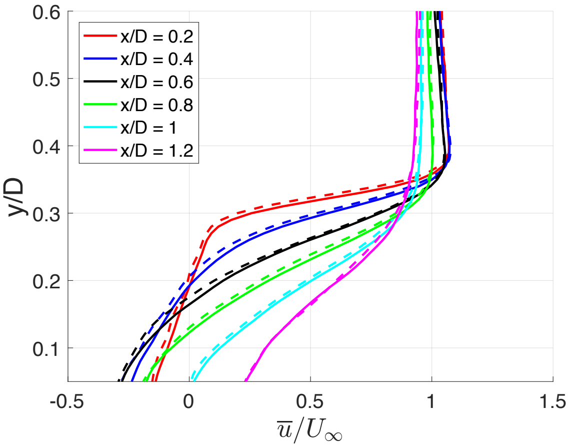

Figure 6.19: Streamwise velocity development for $L/D = 1.8$ case

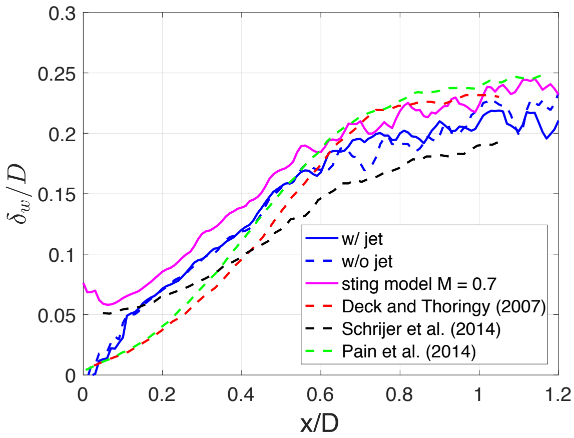

Figure 6.20: Streamwise vorticity thickness development for $L/D = 1.8$ case

$d\delta_w/dx \approx 0.25$. In each of the cases, the presence of the jet has little effect on the development of the vorticity thickness. This increased vorticity thickness cannot be attributed to the exhaust plume because there is little difference between the cases with and without plume; as such, the difference may be caused by another variation between the models.

Figure 6.18 shows the streamwise vorticity development for the hybrid case. The slope of the vorticity development of the separated shear layer is again $d\delta_w/dx \approx 0.25$, which is also equal to the value for the sting mounted model. The $L/D = 1.2$ nozzle length best matches with the numerical results by Deck and Thorigny (2007) and Pain et al. (2014) as the same nozzle length. This could explain the improved agreement between the present results and the literature nearer the point of reattachment.

Figure 6.20 shows the streamwise vorticity development for the solid reattachment case. As with all other cases, the gradient is approximately $d\delta_w/dx \approx 0.25$ and is unchanged by the presence of the exhaust plume. The literature data published by Deck and Thorigny (2007) and Pain et al. (2014) used a model with afterbody of length $L/D = 1.2$, whereas Schrijer et al. (2014) used an L/D of 2.5. Schrijer et al. (2014) notes a slightly reduced gradient of $d\delta_w/dx = 0.2$ and shows better overall agreement with the present results.

Streamwise Reynolds normal stresses

The Reynolds stress development shown in Figure 6.21 follows a similar trend as shown in Figure 5.13 for the sting mounted model, albeit a bit noisier. Though the Reynolds normal stresses achieve approximately 8%, which is significantly higher than the nearly 5% measured for the sting mounted model. Also, it appears as though for the Reynolds normal stress, $\overline{u'u'}$ that the absence of the jet causes a higher value in the lowest two measurement planes. In the 'middle' plane the RMSD caused by the presence of the jet for the streamwise Reynolds normal stress is 1.2%.

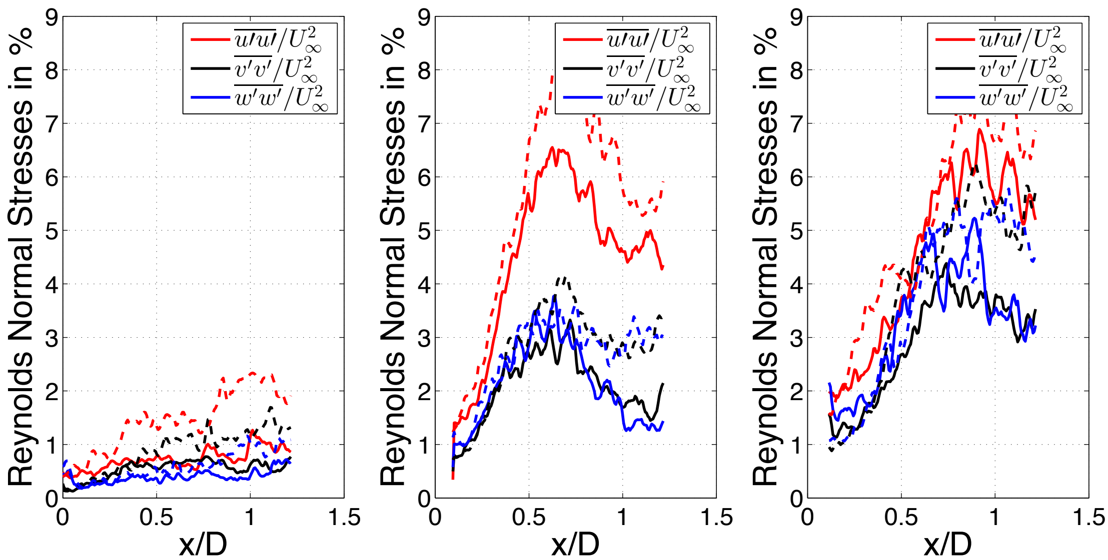

(a) Top of BFS ($y/D = 0.33$) (b) 2/3 of BFS ($y/D = 0.22$) (c) 1/3 of BFS ($y/D = 0.11$)

Figure 6.21: Streamwise development of Reynolds normal stresses at varying BFS heights for the $L/D = 0.6$ case; solid line (with jet) and dashed line (without jet)

The development of the Reynolds normal stresses for the $L/D = 1.2$ case show the greatest values out of all cases at roughly 8%. This follows nicely from the radial velocity fluctuations for which the greatest values are also found in the same length case. From this it can be reasonably be deduced that the level of turbulent mixing happening in the wake of the BFS is greatest for this nozzle length. Additionally, the effect of the jet seems to provide a slight increase in this turbulent mixing as seen in Figure 6.22(b).

In Figure 6.21 it was seen that the case with an exhaust plume has lower Reynolds normal stresses than the case with plume. This is the opposite for the increase in Reynolds normal stresses seen on the central plane in Figure 6.22(b) for the $L/D = 0.6$ case. RMSD caused by the presence of the jet for the streamwise componet is 0.7 %, which is less than the 1.2% reported for the shorter nozzle length.

The streamwise development of the Reynolds normal stresses for the $L/D = 1.8$ case most closely resembles that of the sting mounted model discussed in section 5.4 and seen in Figure 5.13; this is apparent in both trend and magnitude, both achieving a maximum percentage of approximately 5%. The upper plane at the top of the BFS shows very low Reynolds stress with little variation. The lower two planes show an increase, first most significantly for $\overline{u'u'}$ and later for all three normal stresses. The effect of the jet is seen as a small RMSD of 1.0% for the streamwise component on the 'middle' plane.

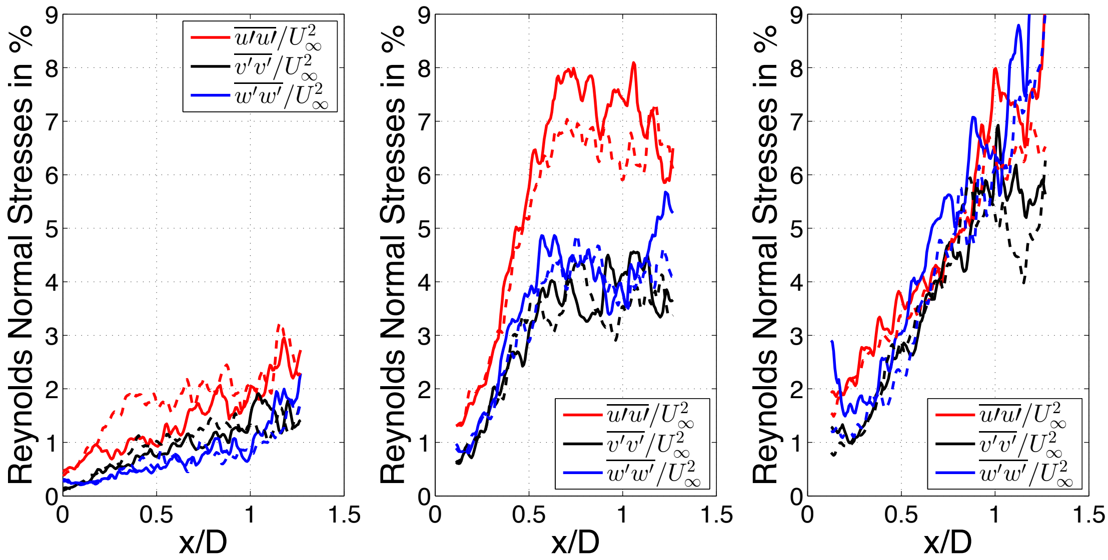

(a) Top of BFS ($y/D = 0.33$) (b) 2/3 of BFS ($y/D = 0.22$) (c) 1/3 of BFS ($y/D = 0.11$)

Figure 6.22: Streamwise development of Reynolds normal stresses at varying BFS heights for the $L/D = 1.2$ case; solid line (with jet) and dashed line (without jet)

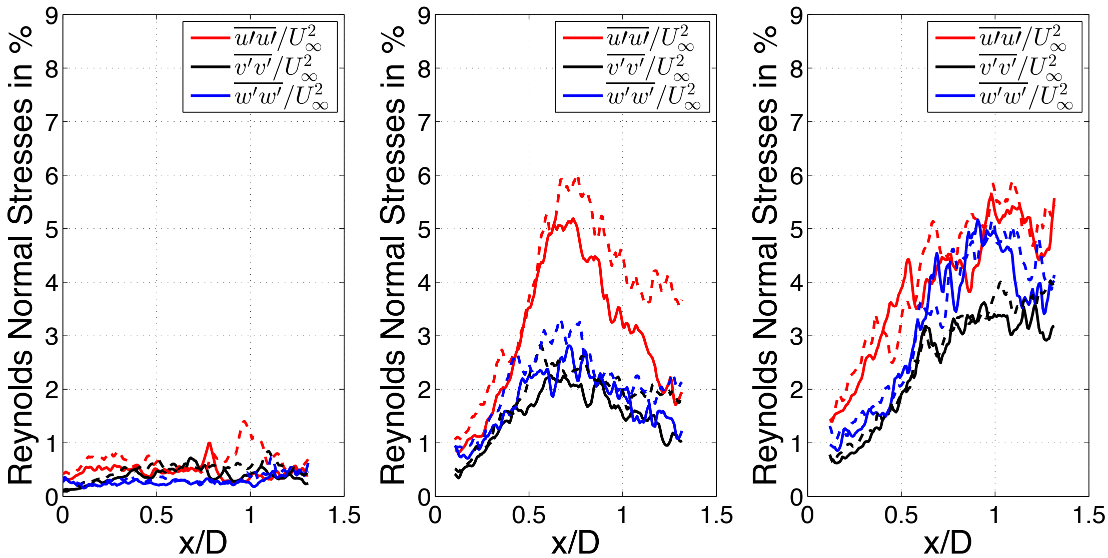

(a) Top of BFS ($y/D = 0.33$) (b) 2/3 of BFS ($y/D = 0.22$) (c) 1/3 of BFS ($y/D = 0.11$)

Figure 6.23: Streamwise development of Reynolds normal stresses at varying BFS heights for the $L/D = 1.8$ case; solid line (with jet) and dashed line (without jet)

6.3 Discussion of Observations

The largest velocity fluctuations are found in the $L/D = 1.2$ case. Statistically, it can be stated that the hybrid reattachment case features the greatest unsteadiness when compared to the other two cases. Additionally, the presence of the exhaust plume seems to increase the unsteadiness compared to the case without an exhaust plume. As stated in the theoretical discussion in Chapter 2, the afterbody without exhaust plume has an additional recirculation region in the wake of the nozzle exit. For the nozzle of length, $L/D = 1.2$ this potentially unstable region is out of the field of view. This could mean that the cause for the RMS difference is simply the lack of a complete view of the flow field.

For the $L/D = 0.6$ case, the aforementioned near-wake is visible in the field of view. When comparing the cases with and without an exhaust plume, the opposite is noted in comparison to the $L/D = 1.2$ cases. For the shorter nozzle length, the exhaust plume seems to induce a stabilizing effect as evidenced by a decrease in the RMS of the velocity fluctuations. This could potentially also be occurring in the hybrid length case but because the near-wake is not included in the field of view, such conclusions cannot be made. The longest case, which features the most consistent solidly reattaching shear layer, is most like the sting mounted model in all respects; this comes as no surprise.

The development of the shear layer and the mixing which occurs within the region near the base is resolved equally well for each of the three nozzle length cases; all length cases resolve a main recirculation region, a separated shear layer, and its impingement point, attaching to either a solid surface or the fluid. The development of the Reynolds normal stresses show the largest values and growth rates for the $L/D = 1.2$ length case, which is promising and lends validity to the earlier statement that this is the most turbulent case; further testing can be done to further enforce these claims. Investigations of the separated shear layer, by way of vorticity development and streamwise velocity development show little difference between the separate nozzle lengths or caused by the presence of the plume.

A difference in cases is noticed for the mean pressure fields. As is expected from literature, when fluidic reattachment occurs the presence of the exhaust plume can have an effect referred to as the 'jet-suction' effect. The measured difference is not as large as that which is found in literature even though this case used a larger NPR. In the two longer nozzle length cases the presence of the jet had no effect on the wall pressure values, which is also in agreement with literature.

Chapter 7

Conclusions and Recommendations

Lastly, the conclusions and recommendations for future work based on the results from the second experimental campaign presented in chapter 6. Therein it was concluded that the $L/D = 1.2$ nozzle length featured the greatest turbulent mixing in the wake of the BFS. This is reasoned from the increased velocity fluctuations which could lead to buffeting of the nozzle. For that reason, it is first and foremost concluded to avoid such a hybrid reattachment in the design of a launch vehicle because of the potential for exhaust gas entrainment and subsequent thermal loading of the base.

The nozzle length, $L/D = 0.6$ has been shown to feature the same 'jet-suction' effect as outlined by Deprés et al. (2004); this highlights the promise of the PIV based pressure reconstruction technique. Additionally, the presence of the jet appears to have a stabilizing effect for cases with fluidic reattachment. Though less turbulent than the BFS wake of the $L/D = 1.2$ case, the fluidic reattachment case was still more turbulent than the longest, solid reattachment case. As such, it is the noted from the perspective of flow stability, that the $L/D = 1.8$ is the best option; that being said, it will also constitute the heaviest option, which is of concern when designing a launch vehicle. The shortest, $L/D = 0.6$ case can cause ingestion of the exhaust plume and the intermediate $L/D = 1.2$ case causes the highest turbulent mixing in the BFS wake; contrary to these, the longest nozzle length most closely resembles the sting mounted model.

It has been shown that the momentum equation based pressure reconstruction is in very good agreement with pressure transducer measurements in the same region. The results presented in this regard show that the approach used herein performs well in both subsonic and supersonic, non-isentropic BFS wakes. More so than others, the Reynolds stress terms are an important contributing term for the pressure reconstruction. As expected for flows with a Reynolds number in excess of 10^6, the inviscid flow assumption is valid. Out-of-plane flow components are of importance in the recirculation and reattachment regions where the flow is more turbulent. With the artificially created planar PIV results it was shown that the lack of these terms causes a slight deviation from the pressure transducer measurements.

The supersonic case was a more stable flow field. This was seen in the RMS of the reattachment length, the RMS of the velocity fluctuations, and the pressure transducer measurements. The unsteady motion that exists in the transonic case is thus largely diminished or non-existent in the supersonic case. Naturally, engineers should continue to design the launch vehicle for its entire ascent profile, but investigations into flow behavior at higher Mach numbers were serve to improve understanding.

Recommendations for future configurations

It has been found that the $L/D = 1.2$ configuration did not quite provide a 'hybrid' reattachment case with equal parts fluidic and solid reattachment. Instead, a vast majority of cases feature solid reattachment with a mean length, $\overline{x_r}/D \approx 1.0$; this is in agreement with Gentile et al. (2016). Future research should take this into account by fabricating an additional 10 mm spacer ring to create a true hybrid reattachment configuration.

More generally, the model modifications that have been produced should continue to be used for testing at various Mach numbers. This may require the production of additional spacer rings to cause the same solid, hybrid, and fluidic reattachment cases. In doing so, research could be conducted at different Mach numbers to see if the hybrid reattachment case causes the same increased turbulent mixing at different Mach numbers.

This is a key research question that remains, because as the vehicle continues to accelerate, it will eventually travel at supersonic speeds, thus drastically decreasing the reattachment length. It was shown for the supersonic case of the first experimental campaign that the reattachment length of a supersonic flow was $x_r/D = 0.6$. Thus, if the $L/D = 0.6$ case were to be recommended as the best configuration for a transonic launch vehicle, such a nozzle length may quickly resemble the hybrid case seen herein once the vehicle is traveling at supersonic speeds. With this in mind, the $L/D = 1.8$ case was concluded as the most stable option because once immersed in supersonic flow, the BFS will still feature solid reattachment.

As noted by Deprés et al. (2004), the NPR value with which the cold plume is operated has an effect on the C_p. This is especially true in cases featuring fluid reattachment (L/D = 0.6) and it has been noted by Deprés et al. (2004) that an increase in NPR increases the jet suction effect. In the present thesis it was demonstrated that the jet suction effect can be detected using the present PIV based pressure reconstruction for an NPR = 100. Future researchers should also attempt to capture the effect of NPR on C_p. Additionally, various cases of fluidic reattachment could be investigated to see if there are varying degrees of the effect dependent upon nozzle length (e.g. $L/D = 0.4$, 0.8, etc.).

Recommendations for future measurements

Using tomographic PIV to study an axisymmetric BSF at transonic Mach numbers was a unique aspect of the present thesis. That being said, future researchers studying this same flow field are dissuaded from using tomographic PIV. Though, it did provide a more accurate pressure reconstruction near the highly turbulent reattachment location due to in-plane components, there was little extra insight gathered from the spanwise velocity data. The out-of-plane components, which separate tomographic PIV from planar PIV, were not worth the added complexity of the measurement apparatus or the reduction in spatial resolution when compared to planar PIV. The present tomographic experiments had a spatial resolution of 23 pix/mm which led to greater uncertainty; using planar PIV, a greater spatial resolution, upwards of 40 pix/mm could be achieved.

That being said, with the instantaneous snapshots of the flow, the spanwise velocity was used to try and find evidence for the slow, processing shear layer as described by Deck and Thorigny (2007), Weiss and Deck (2011), and Gentile et al. (2016). The present experiments featured an afterbody diameter of 20 mm and 17 mm which were viewed with a volume depth of 5 mm and 8 mm in experimental campaigns I and II, respectively. As such, these volumes did not feature the depth to adequately image such a slow, meandering shear layer as it passed through the field of view. That being said, this recommendation to avoid tomographic PIV for transonic axisymmetric BFS flows hinges on advancements in PIV laser and imaging hardware. Should advancements allow for the flow to be more spatially or temporally resolved, the identification of such unsteady topological flow features may be possible.

One of the conclusions of the present work was that the hybrid reattachment length case was the most turbulent. This could be wrongfully based on the hybrid case managing to capture that region near the nozzle exit which is highly turbulent and failing to do so for the solid reattachment case. Future investigations should also image the near-wake of the BFS and nozzle to determine the turbulent statistics in that region; this will be more feasible if a multi-camera planar system is used instead of a tomographic system. Though the present experiment aimed to resolve the wake of the BFS within the confines of the nozzle area, the aforementioned downstream location could still yield insightful conclusion for the exhaust gas entrainment scenario discussed in the introduction.

At present, using the same hardware used for the experiments performed in this thesis work, experiments could also be conducted with the illuminated volume being positioned perpendicular to the incoming flow. This would allow for the capturing of a far broader flow field at the expense of resolution in the streamwise direction. Such measurements were already performed by Gentile et al. (2016) at far lower Reynolds numbers ($Re_D = 6.7 \cdot 10^4$) on a model without afterbody; the addition of an afterbody, as is the case herein, would complicate the illumination of the field of view.

Closing

These results and conclusions provide insight to future designers of space launch vehicles in the preliminary design phase. Tomographic PIV has been used to identify flow features, and their behavior, which other researchers had previously used other experimental techniques to measure. Additionally, the velocimetric data was used to perform an analysis of the wake of a BFS and to reconstruct a pressure field in that region. The effect of geometrical changes on these topological features was used to make general recommendations for the design of space launch vehicles.

Bibliography

E.W. Adams and J.P. Johnston. Effects of the separating shear layer on the reattachment flow structure Part 2: Reattachment length and wall shear stress. *Experiments in Fluids*, 6(1):493–499, 1988.

J. Anderson. *Fundamentals of Aerodynamics*. McGraw Hill, New York, 5th edition, 2011.

Arianespace. Press Conference to Flight 157 - {Ariane 5} {ECA}. Paris, France, 2003.

W.J. Bannink, P.G. Bakker, and E.M. Houtman. FESTIP Aerothermodyanmics: Experimental Investigation of Base Flow and Exhaust Plume Interaction. *Memorandum M-775*, (March), 1997.

L.H. Benedict and R.D. Gould. Towards better uncertainty estimates for turbulence statistics. *Experiments in Fluids*, 22:129–136, 1996. ISSN 0723-4864. doi: 10.1007/s003480050030.

M. Bitter, S. Scharnowski, R. Hain, and C.J. Kähler. High-repetition-rate PIV investigations on a generic rocket model in sub- and supersonic flows. *Experiments in Fluids*, 50(4): 1019–1030, 2011. ISSN 07234864. doi: 10.1007/s00348-010-0988-8.

M. Bitter, T. Hara, R. Hain, D. Yorita, K. Asai, and C.J. Kähler. Characterization of pressure dynamics in an axisymmetric separating/reattaching flow using fast-responding pressure-sensitive paint. *Experiments in Fluids*, 53(6):1737–1749, 2012.

P. Bradshaw and F.Y.F. Wong. The reattachment and relaxation of a turbulent shear layer. *Journal of Fluid Mechanics*, 52:113–135, 1972.

C.E. Brennen. *Fundamentals of Multiphase Flow*. Cambridge University Press, 2005. ISBN 9780511807169. doi: 10.1017/CBO9780511807169.

F.K. Browand. An experimental investigation of the instability of an incompressible, separated shear layer. *Journal of Fluid Mechanics*, 26(2):281–307, 1966.

C.D.C. Intelligence Bulletin 63: Occupational Exposure to Titanium Dioxide, 2011.

Z. Chen, S. Yi, L. He, L. Tian, and Y. Zhu. An experimental study on fine structures of supersonic laminar / turbulent flow over a backward-facing step based on NPLS. *Chinese Science Bulletin*, 57(6):584–590, 2012. doi: 10.1007/s11434-011-4888-y.

R. De Kat and B.W. Van Oudheusden. Instantaneous planar pressure determination from PIV in turbulent flow. *Experiments in Fluids*, 52(5):1089–1106, 2012. ISSN 07234864. doi: 10.1007/s00348-011-1237-5.

S. Deck and P. Thorigny. Unsteadiness of an axisymmetric separating-reattaching flow: Numerical investigation. *Physics of Fluids*, 19(6), 2007. ISSN 10706631. doi: 10.1063/1.2734996.

D. Deprés, P. Reijasse, and J.P. Dussauge. Analysis of Unsteadiness in Afterbody Transonic Flows. *AIAA Journal*, 42(12), 2004. ISSN 0001-1452. doi: 10.2514/1.7000.

F.J. Donker Duyvis. Laser sheet probe design for PIV in high-speed wind tunnels. *PIVNET II International Workshop on the Application of PIV in Compressible Flows*, (June), 2005.

D.M. Driver, H.L. Seegmiller, and J.G. Marvin. Time-Dependent Behavior of a Reattaching Shear Layer. *AIAA Journal*, 25(7):914–919, 1987.

J.K. Eaton and J.P. Johnston. A Review of Research on Subsonic Turbulent Flow Reattachment. *AIAA Journal*, 19(9):1093–1100, 1981.

G.E. Elsinga, F. Scarano, B. Wieneke, and B.W. van Oudheusden. Tomographic particle image velocimetry. *Experiments in Fluids*, 41(6):933–947, 2006. ISSN 07234864. doi: 10.1007/s00348-006-0212-z.

G.E. Elsinga, J. Westerweel, F. Scarano, and M. Novara. On the velocity of ghost particles and the bias errors in Tomographic-PIV. *Experiments in Fluids*, 50(4):825–838, 2011. ISSN 07234864. doi: 10.1007/s00348-010-0930-0.

H.V. Fuchs, E. Mercker, and U. Michel. Large-scale coherent structures in the wake of axisymmetric bodies. *Journal of Fluid Mechanics*, 93(1):185–207, 1979. ISSN 0022-1120. doi: 10.1017/S0022112079001841.

V. Gentile, F.F.J. Schrijer, B.W. van Oudheusden, and F. Scarano. Time-dependent Behaviour of the Recirculation Region Behind an Axisymmetric Bluff Body. pages 1–7, 2016.

M. Grandemange, M. Gohlke, and O. Cadot. Statistical axisymmetry of the turbulent sphere wake. *Experiments in Fluids*, 55(11), 2014. ISSN 07234864. doi: 10.1007/s00348-014-1838-x.

R. Gurka, A. Liberzon, and D. Hefetz. Computation of pressure distribution using PIV velocity data. *Workshop on Particle ...*, 106(2):1–6, 1999. ISSN 16726820. doi: 10.1115/1.1631009.

R. Hain, C.J. Kähler, and C. Tropea. Comparison of {CCD}, {CMOS} and intensified cameras. *Experiments in Fluids*, 42(3):403–411, 2007.

R. Hain, S. Scharnowski, N. Reuther, C.J. Kähler, A. Schröder, R. Geisler, and J. Agocs. Coherent large scale structures in adverse pressure gradient turbulent boundary layers. In *18th International Symposium on the Application of Laser Imaging Techniques to Fluid Mechanics*, pages 474–496, Lisbon, 2016.

S.D. Hall, M. Behnia, C.A.J. Fletcher, and G.L. Morrison. Investigation of the secondary corner vortex in a benchmark turbulent backward-facing step using cross-correlation particle imaging velocimetry. *Experiments in Fluids*, 35(1):139–151, 2003. doi: 10.1007/s00348-003-0626-9.

J. Hong, M. Toloui, L.P. Chamorro, M. Guala, K. Howard, S. Riley, J. Tucker, and F. Sotiropoulos. Natural snowfall reveals large-scale flow structures in the wake of a 2.5-MW wind turbine. *Nature Communications*, 5(May):16, 2014. ISSN 2041-1723. doi: 10.1038/ncomms5216.

L.M. Hudy, A Naguib, and W.M. Humphreys. Stochastic estimation of a separated-flow field using wall-pressure-array measurements. *Physics of Fluids*, 19(1), 2007. doi: 10.1063/1.2472507.

R.A. Humble. *Unsteady Flow Organization of a Shock Wave/Boundary Layer Interaction.* Phd thesis, Delft University of Technology, 2009.

K. Isomoto and S. Honami. The Effect of Inlet Turbulence Intensity on the Reattachment Process Over a Backward-Facing Step. *ASME Journal of Fluids Engineering*, 111(1):87–92, 1989.

Y.J. Jeon, L. Chatellier, A. Beaudoin, and D. Laurent. Least-square reconstruction of instantaneous pressure field around a body based on a directly acquired material acceleration in time-resolved PIV. In *11th International Symposium on Particle Image Velocimetry - PIV15*, Santa Barbara, 2015.

C.J. Kähler and U. Scholz. Transonic jet analysis using long-distance micro-PIV. In *12th International symposium on flow visualization*, 2006.

J. Kostas, J. Soria, and M.S. Chong. Particle image velocimetry measurements of a backward-facing step flow. *Experiments in Fluids*, 33:838–853, 2002. doi: 10.1007/s00348-002-0521-9.

LaVision GmbH. LaVision DaVis 8.3 Product Manual, 2015.

K.P. Lynch and F. Scarano. Material acceleration estimation by four-pulse tomo-PIV. *Measurement Science and Technology*, 25, 2014. ISSN 0957-0233. doi: 10.1088/0957-0233/25/8/084005.

P. Meliga and P. Reijasse. Unsteady transonic flow behind an axisymmetric afterbody with two boosters. *AIAA*, 2007.

A. Melling. Tracer particles and seeding for particle image velocimetry. *Measurement Science and Technology*, 1406(8):1406–1416, 1997.

R. Pain, P.E. Weiss, and S. Deck. Zonal Detached Eddy Simulation of the flow around a simplified launcher afterbody. *AIAA Journal*, 52(9):1967–1979, 2014.

S. Pope. *Turbulent Flows.* Cambridge University Press, Ithica, 1st edition, 2000.

M. Raffel, C.E. Willert, S.T. Wereley, and J. Kompenhans. *Particle Image Velocimetry, a Practical Guide*, volume 2. Springer, Berlin, 2 edition, 2007. ISBN 9783540723073. doi: 10.1007/978-3-540-72308-0.

D. Ragni. *PIV-based load determination in aircraft propellers.* Phd thesis, Delft University of Technology, 2012.

D. Ragni, F.F.J. Schrijer, B.W. van Oudheusden, and F. Scarano. Particle tracer response across shocks measured by PIV. *Experiments in Fluids*, 50(1):53–64, 2011. ISSN 07234864. doi: 10.1007/s00348-010-0892-2.

G. Rigas, A.R. Oxlade, A.S. Morgans, and J.F. Morrison. Low-dimensional dynamics of a turbulent axisymmetric wake. *Journal of Fluid Mechanics*, 755(2014), 2014. ISSN 0022-1120. doi: 10.1017/jfm.2014.449.

S.K. Robinson. Coherent Motions in the Turbulent Boundary Layer. *Annual Review of Fluid Mechanics*, 23:601–639, 1991.

D. Saile, D. Kirchheck, G. Ali, and D. Banuti. Design of a Hot Plume Interaction Facility at DLR Cologne. *Proceedings of the 8th European Symposium on Aerothermodynamics for Space Vehicles*, 2015.

F. Scarano. Tomographic PIV: principles and practice. *Measurement Science and Technology*, 24, 2013a. ISSN 0957-0233. doi: 10.1088/0957-0233/24/1/012001.

F. Scarano. *AE 4180: Experimental Aerodynamics.* Number February. Delft, 2013b.

S. Scharnowski, I. Bolgar, and J.K. Christian. Characterization of Turbulent Structures in a Transonic Backward-Facing Step Flow. 2016a. doi: 10.1007/s10494-016-9792-8.

S. Scharnowski, I. Bolgar, and C.J. Kähler. Investigation of a generic space launcher wake in sub- , trans- and supersonic conditions. *International Workshop on Non-intrusive Optical Flow Diagnostics*, (October), 2016b.

M.M.J. Schoones and W.J. Bannink. *Base flow and exhaust plume interaction. Part 2: Computational study.* Delft, 1998. ISBN 9040717478.

F.F.J. Schrijer and F. Scarano. Effect of predictor-corrector filtering on the stability and spatial resolution of iterative PIV interrogation. *Experiments in Fluids*, 45(5):927–941, 2008. ISSN 07234864. doi: 10.1007/s00348-008-0511-7.

F.F.J. Schrijer, A. Sciacchitano, and F. Scarano. Spatio-temporal and modal analysis of unsteady fluctuations in a high-subsonic base flow. *Physics of Fluids*, 26(8):1–20, 2014. ISSN 10897666. doi: 10.1063/1.4891257.

F. Simon, S. Deck, P. Guillen, P. Sagaut, and A. Merlen. Numerical simulation of the compressible mixing layer past an axisymmetric trailing edge. *Journal of Fluid Mechanics*, 591:215–253, 2007. ISSN 0022-1120. doi: 10.1017/S0022112007008129.

L.J. Souverein, B.W. van Oudheusden, and F. Scarano. Particle Image Velocimetry Based Loads Determination in Supersonic Flows. In *45th AIAA Aerospace Sciences Meeting and Exhibit*, number January, Reno, 2007. ISBN 1563478900. doi: 10.2514/6.2007-50.

P.G. Spazzini, G. Iuso, M. Onorato, N. Zurlo, and G.M. Di Cicca. Unsteady behavior of back-facing step flow. *Experiments in Fluids*, 30:551–561, 2001. ISSN 07234864. doi: 10.1007/s003480000234.

A. Spencer and D. Hollis. Correcting for sub-grid filtering effects in particle image velocimetry data. *Measurement Science and Technology*, 16(11):2323–2335, 2005. ISSN 0957-0233. doi: 10.1088/0957-0233/16/11/026.

F. Stern, M. Muste, M.L. Beninanti, and W.E. Eichinger. Summary of Experimental Uncertainty Assessment Methodology with Example, 1999.

Z. Sun. *Micro Ramps in Supersonic Turbulent Boundary Layers: An experimental and numerical study*. 2014. ISBN urn:isbn:9789461919243. doi: 10.4233/uuid:6e1a39dd-1581-4d87-b623-97d1dc39fb78.

R. Theunissen. Theoretical analysis of direct and phase-filtered cross-correlation response to a sinusoidal displacement for PIV image processing. *Measurement Science and Technology*, 23(6), 2012. ISSN 0957-0233. doi: 10.1088/0957-0233/23/6/065302.

C. Tropea, A.L. Yarin, and J.F. Foss. *Springer Handbook of Experimental Fluid Mechanics*, volume 46. Springer, 1 edition, 2008. ISBN 9783540251415. doi: 10.2514/1.38773.

T.R. Troutt, B. Scheelke, and T.R. Norman. Organized structures in a reattaching separated flow field. *Journal of Fluid Mechanics*, 143(1):413–427, 1984.

B.W. van Oudheusden. Principles and application of velocimetry-based planar pressure imaging in compressible flows with shocks. *Experiments in Fluids*, 45(4):657–674, 2008. ISSN 07234864. doi: 10.1007/s00348-008-0546-9.

B.W. van Oudheusden. PIV-based pressure measurement. *Measurement Science and Technology*, 24(3):32001, 2013. ISSN 0957-0233. doi: 10.1088/0957-0233/24/3/032001.

B.W. van Oudheusden, F. Scarano, E.W.M. Roosenboom, E.W.F. Casimiri, and L.J. Souverein. Evaluation of integral forces and pressure fields from planar velocimetry data for incompressible and compressible flows. *Experiments in Fluids*, 43(2-3):153–162, 2007. ISSN 07234864. doi: 10.1007/s00348-007-0261-y.

P.E. Weiss and S. Deck. Control of the antisymmetric mode (m=1) for high Reynolds axisymmetric turbulent separating/reattaching flows. *Physics of Fluids*, 23, 2011. ISSN 10706631. doi: 10.1063/1.3614481.

P.E. Weiss, S. Deck, J.C. Robinet, and P. Sagaut. On the dynamics of axisymmetric turbulent separating / reattaching flows. *Physics of Fluids*, 21, 2009. doi: 10.1063/1.3177352.

J. Westerweel and F. Scarano. Universal outlier detection for PIV data. *Experiments in Fluids*, 39(6):1096–1100, 2005. ISSN 07234864. doi: 10.1007/s00348-005-0016-6.

F. White. *Viscous Fluid Flow*. McGraw-Hill International Edition, third edition, 2006.

B. Wieneke. Volume self-calibration for 3D particle image velocimetry. *Experiments in Fluids*, 45(4):549–556, 2008. ISSN 07234864. doi: 10.1007/s00348-008-0521-5.

C.D. Winant and F.K. Browand. Vortex pairing : the mechanism of turbulent mixing- layer growth at moderate Reynolds number. *Journal of Fluid Mechanics*, 63(2):237–255, 1974.

C.C. Wolf, C.E. Klei, R.M. Buffo, R. Hörnschemeyer, and E. Stumpf. Comparison of Rocket Near-Wakes with and without Nozzle Simulation in Subsonic Freestream Conditions. In *42nd AIAA Fluid Dynamics Conference and Exhibit*, 2012. doi: 10.2514/6.2012-3019.

Appendix A

Technical Drawings

A.1 Modified nozzle

A.2 Backplate

A.3 Spacer rings

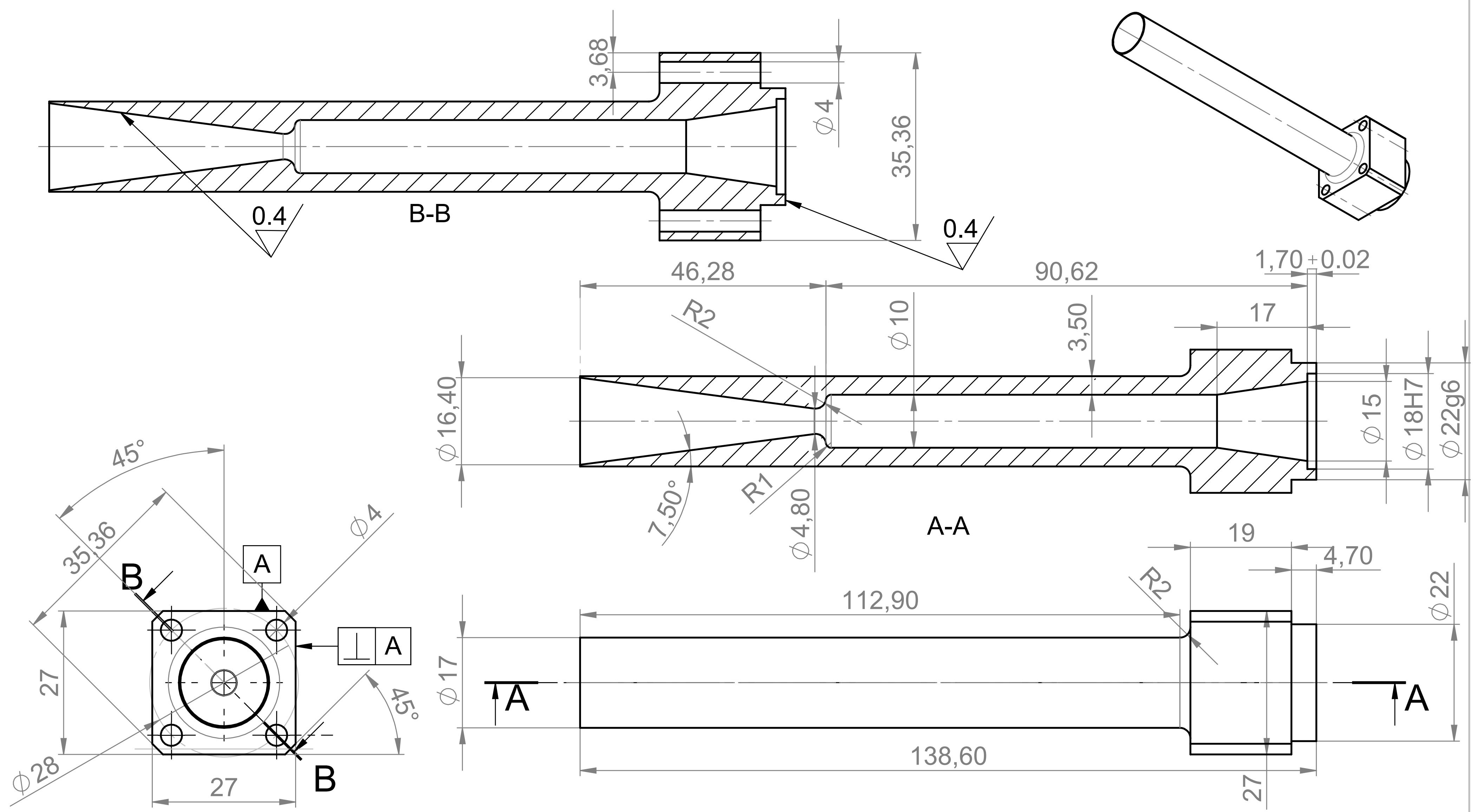

TU Delft Aerospace Engineering	benaming TST nozzle base flow	datum 20-4-2016		schaal 1:1	maateenheid mm
		getekend	groep Aerodynamics HSL	formaat A4	gewicht gram
		SG Brust, Aerospace Engineering +31 6 123 79 158			tekening nr. / opmerkingen

SOLIDWORKS Student Edition.
For Academic Use Only.

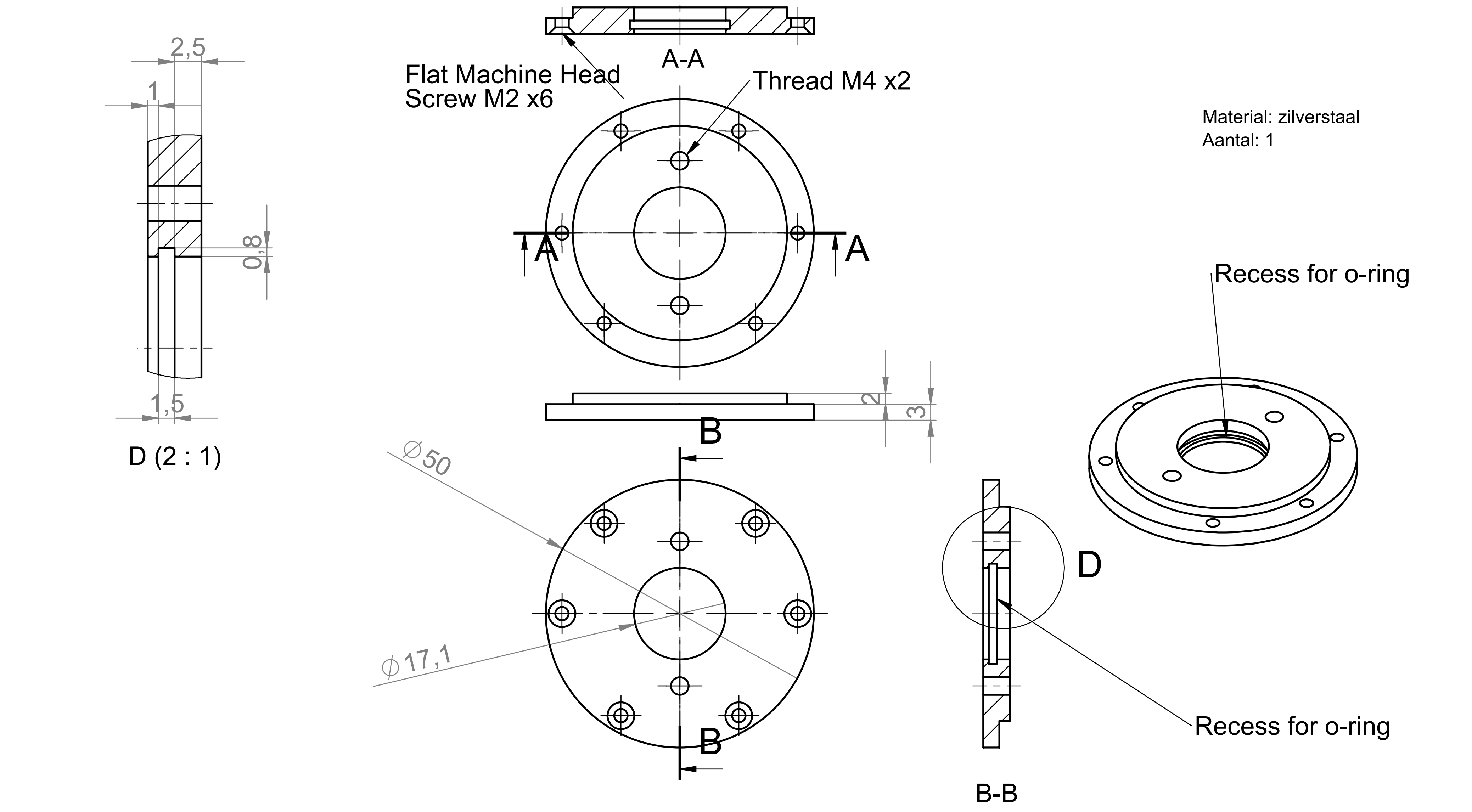

TU Delft Aerospace Engineering	benaming TST base flow base cover	datum 20-4-2016		schaal 1:1	maateenheid mm
		getekend	groep Aerodynamics,HSL	formaat A4	gewicht gram
		S.G. Brust, Aerospace Engineering +31 123 79 158			tekening nr. / opmerkingen

SOLIDWORKS Student Edition
For Academic Use Only.

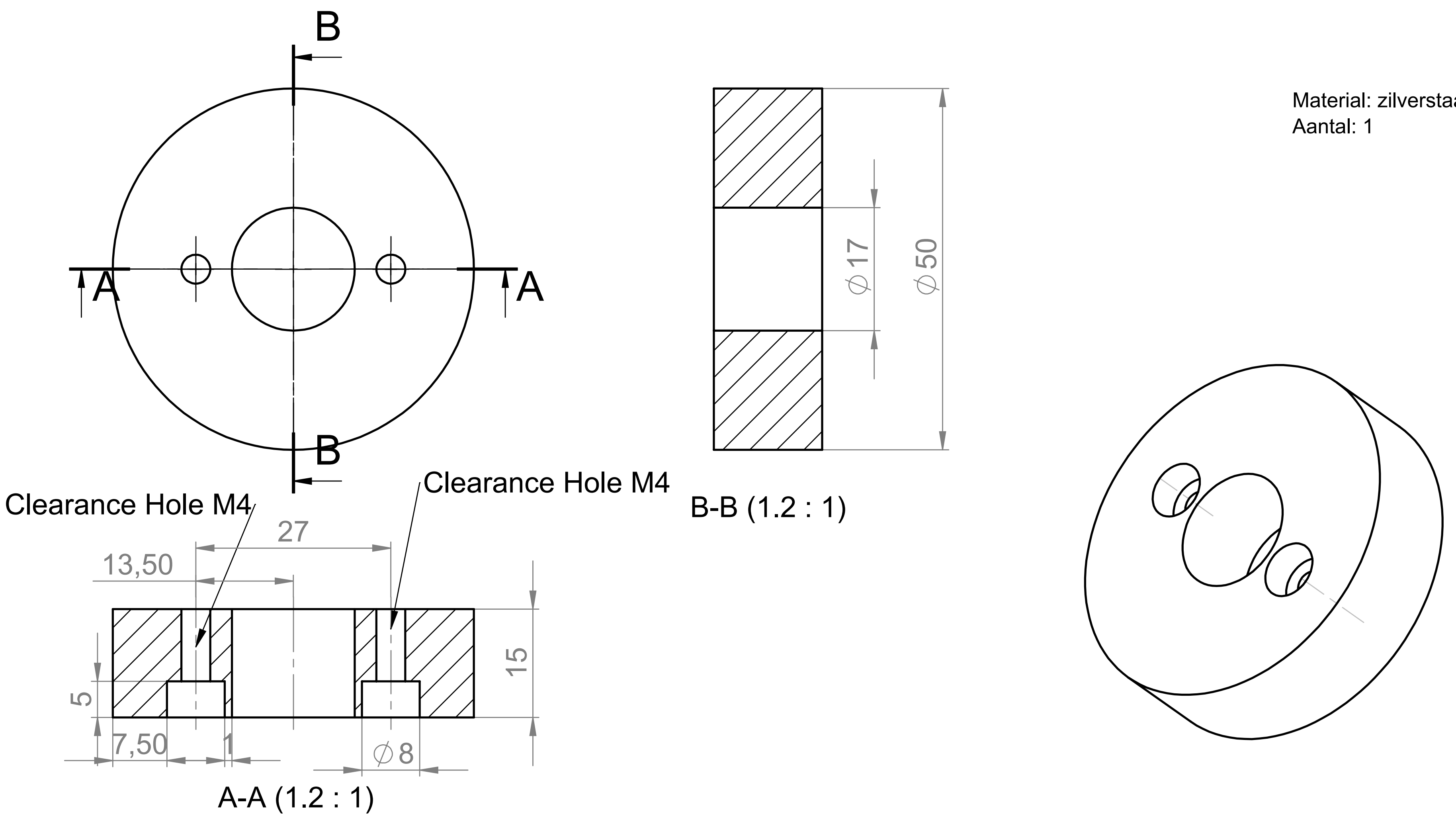

Material: zilverstaal
Aantal: 1

TU Delft Aerospace Engineering	benaming TST spacer 1 base flow	datum 20-4-2016		schaal 1.2:1	maateenheid mm
		getekend	groep Aerodynamics,HSL	formaat A4	gewicht gram
		SG Brust, Aerospace Engineering +31 6 123 79 158			tekening nr. / opmerkingen

SOLIDWORKS Student Edition.
For Academic Use Only.

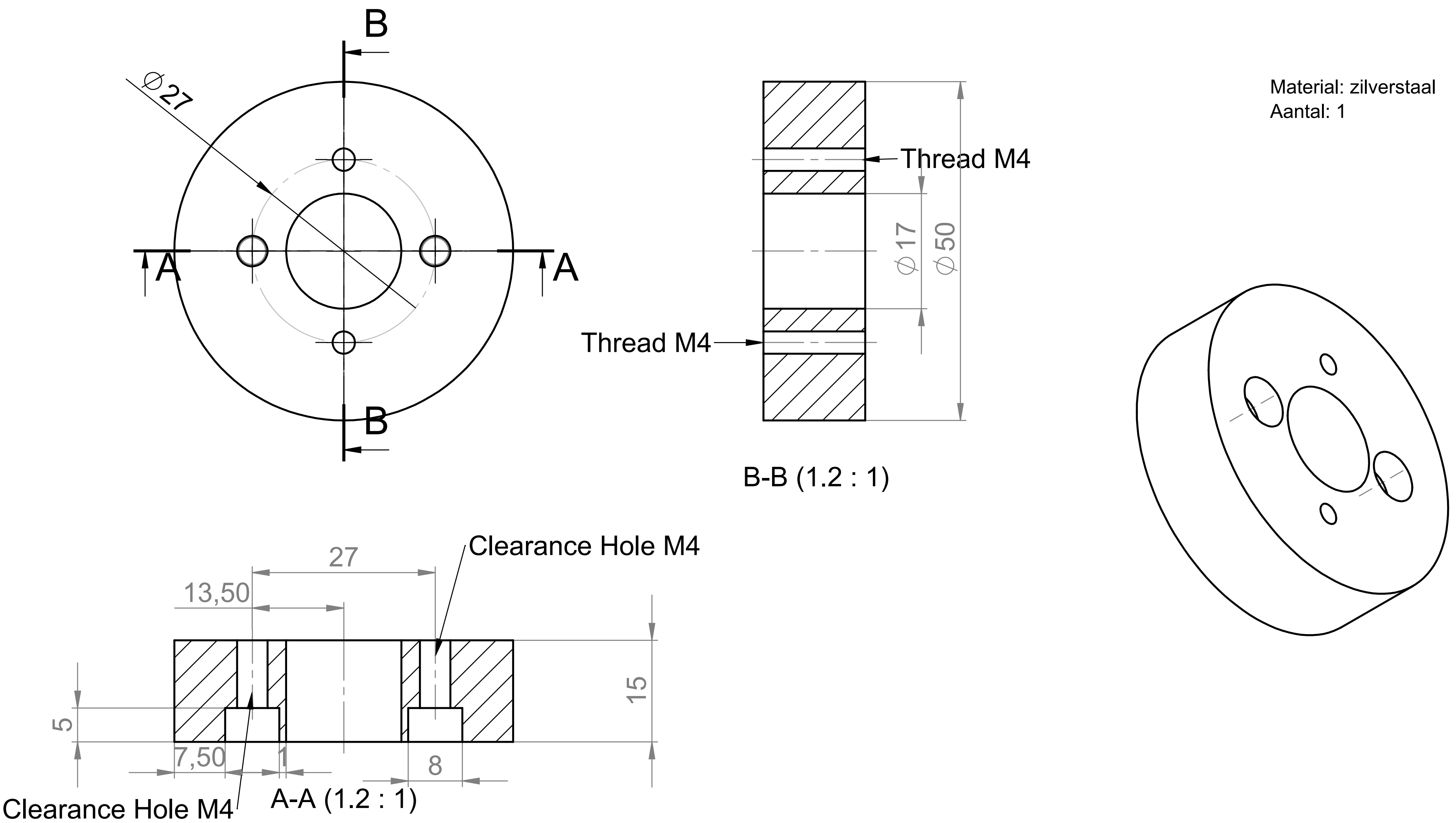

TU Delft Aerospace Engineering	benaming TST spacer 2 base flow	datum 20-4-2016	schaal 1.2:1	maateenheid mm
		getekend	groep <<dagdeel>>	formaat A4	gewicht gram
		SG Brust, Aerospace Engineering +31 6 123 79 158			tekening nr. / opmerkingen

SOLIDWORKS Student Edition.
For Academic Use Only.

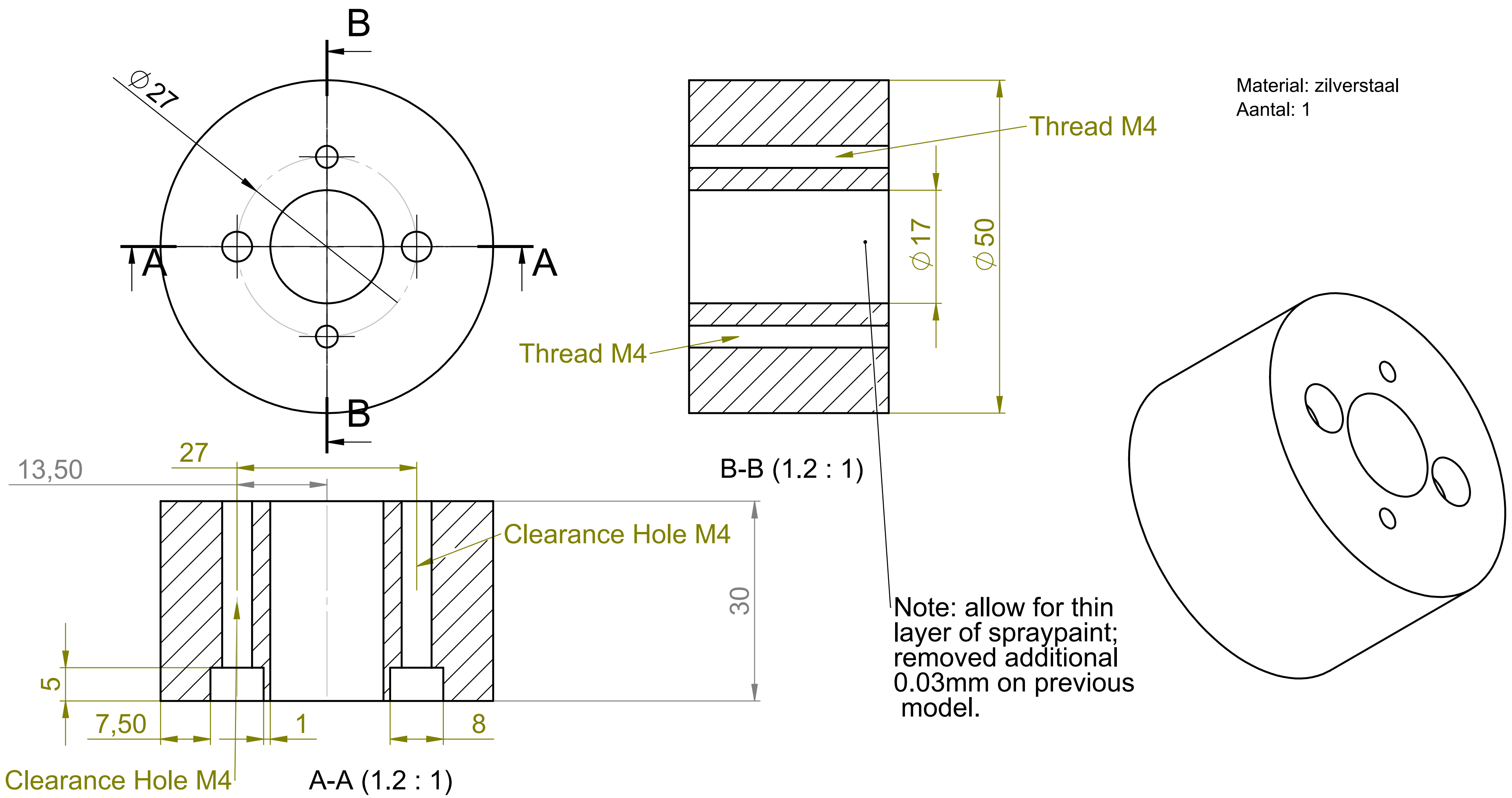

TU Delft Aerospace Engineering	benaming TST spacer 3 base flow	datum 20-6-2016		schaal 1.2:1	maateenheid mm
		getekend	groep <<dagdeel>>	formaat A4	gewicht gram
		SG Brust, Aerospace Engineering +31 6 123 79 158			tekening nr. / opmerkingen

SOLIDWORKS Student Edition.
For Academic Use Only.

Appendix B

FESTIP Setup

FESTIP Control Box (FCB)

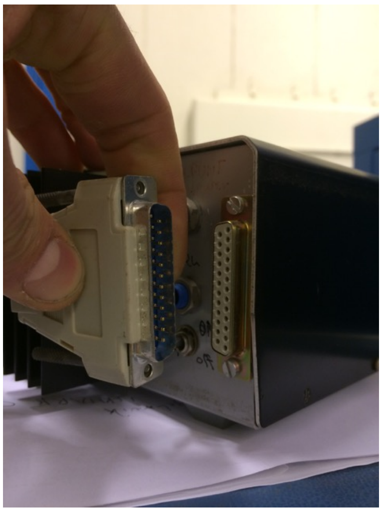

Figure B.1: 1: 25 Pole D-Connector into FCB

Figure B.2: 2: 3 Pole Amphenol into FCB

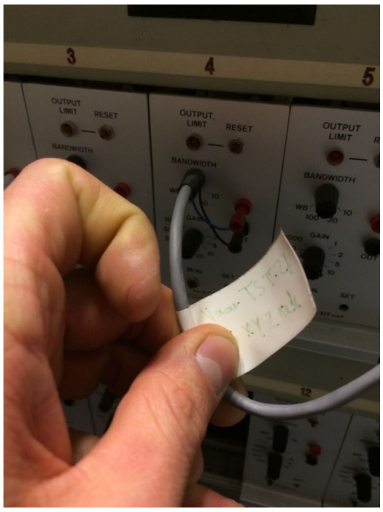

Figure B.3: 3: Output signal conditioner Ch.4

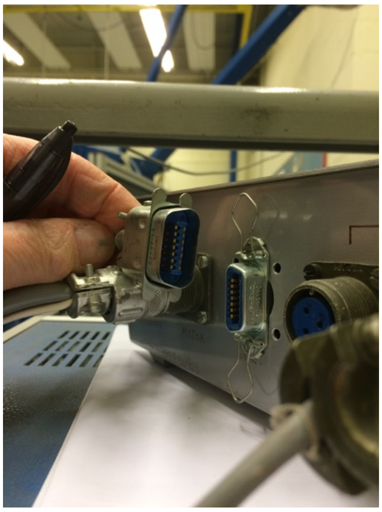

Figure B.4: 4: 14 Pole Amphenol into FCB

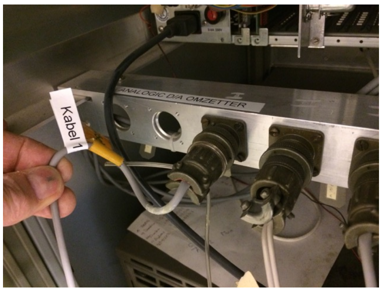

Figure B.5: 5: Output at rear of Analogic to FCB

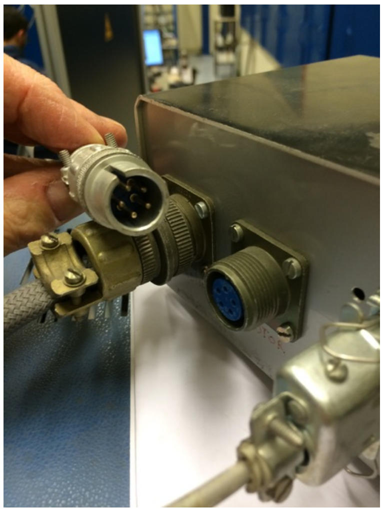

Figure B.6: 6: 5 Pole Amphenol into FCB

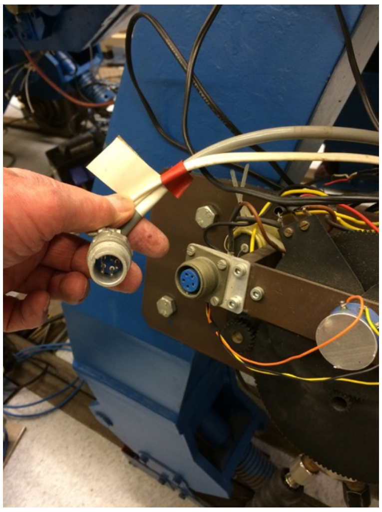

Figure B.7: 7: 5 Pole Amphenol feedback line from air supply regulating valve

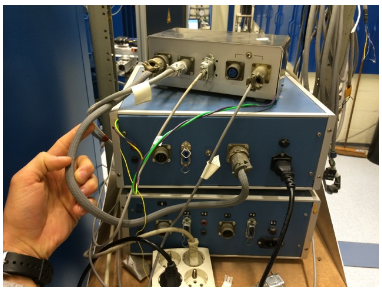

Figure B.8: 8: Rear of FESTIP Control Box (FCB)

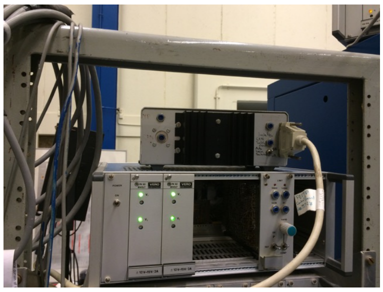

Figure B.9: 9: Front of FESTIP Control Box (FCB)

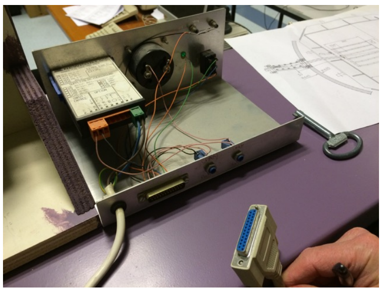

Figure B.10: 10: 25 Pole D-connector at jet pressure control unit

Figure B.11: 11: Front of jet pressure control unit

Figure B.12: 12: Front of Analogic converter

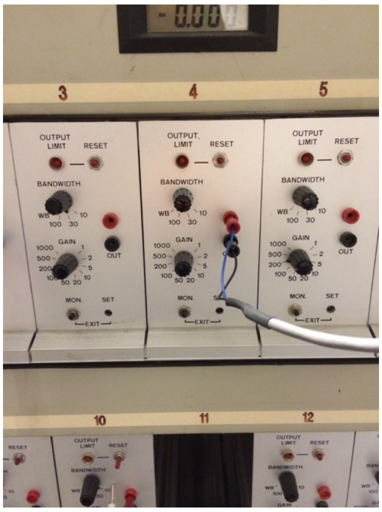

Figure B.13: 13: Signal Conditioner/Amplifier

Figure B.14: 14: Two schematic lines wrapped in single cable housing at rear of Ch. 4 signal conditioner

Figure B.15: 15: Overhead box guiding cables to TST

Figure B.16: 16: Tunnel input port

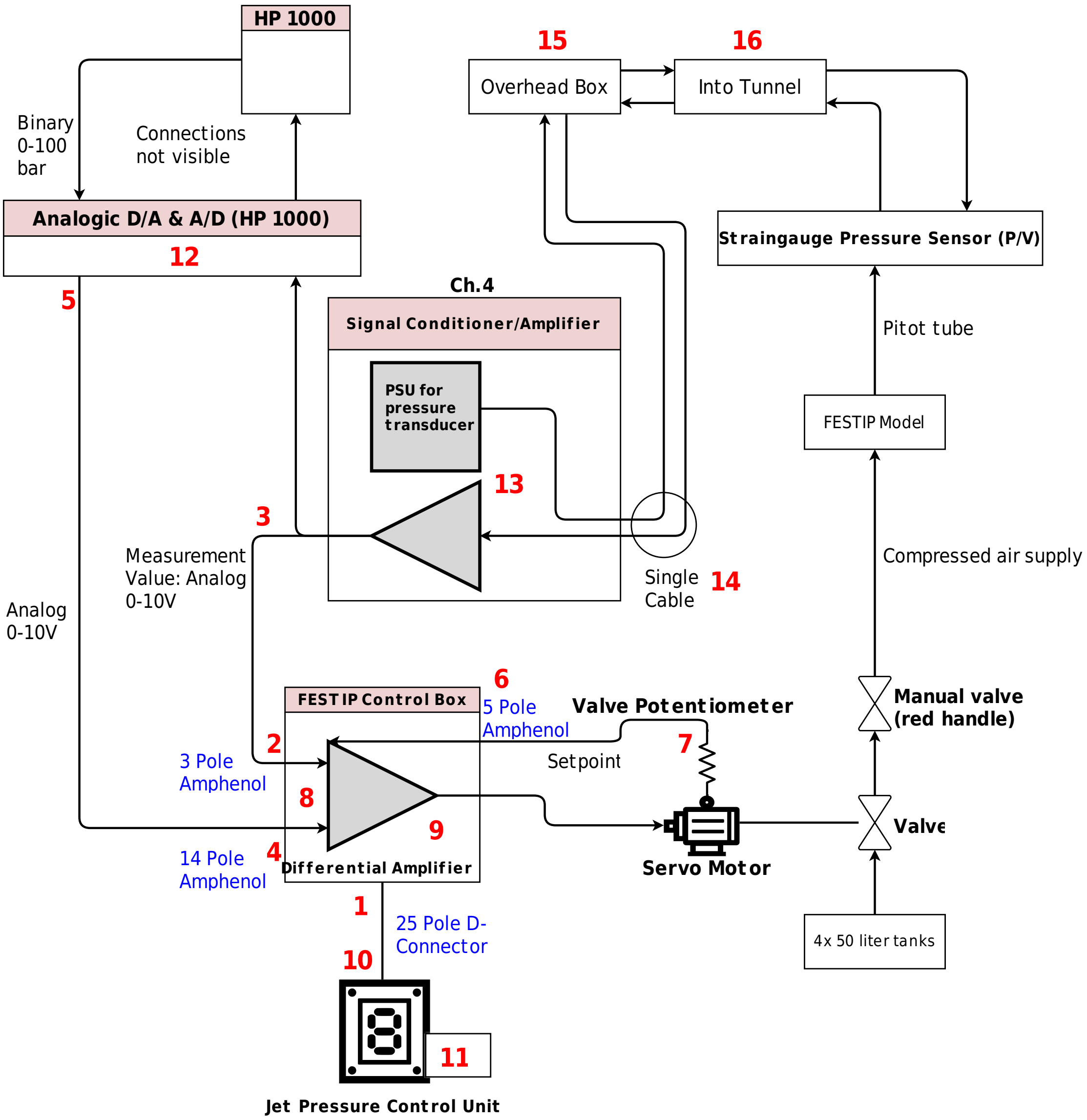
HP 1000
Binary 0-100 bar
Connections not visible
Analogic D/A & A/D (HP 1000)
12
5
15
16
Overhead Box
Into Tunnel
Straingauge Pressure Sensor (P/V)
Pitot tube
FESTIP Model
Ch.4
Signal Conditioner/Amplifier
PSU for pressure transducer
13
3
Measurement Value: Analog 0-10V
Single Cable
14
Compressed air supply
Analog 0-10V
FESTIP Control Box
6
5 Pole Amphenol
Valve Potentiometer
Manual valve (red handle)
7
Setpoint
3 Pole Amphenol
2
8
9
Valve
Servo Motor
14 Pole Amphenol
4
Differential Amplifier
1
25 Pole D-Connector
10
4x 50 liter tanks
11
Jet Pressure Control Unit

Appendix C

Reynolds Stress Terms for Subsonic Case from Experimental Campaign I

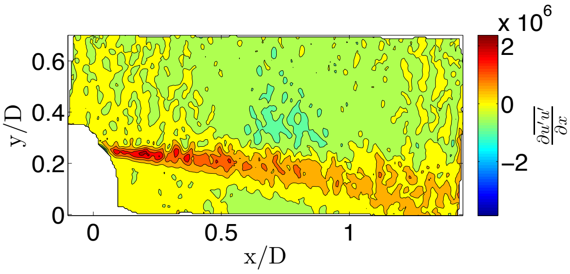

(a) $\frac{\partial \overline{u'u'}}{\partial x}$

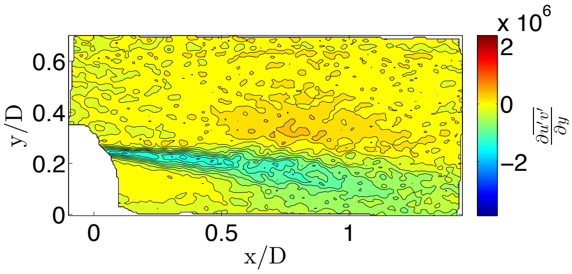

(b) $\frac{\partial \overline{u'v'}}{\partial y}$

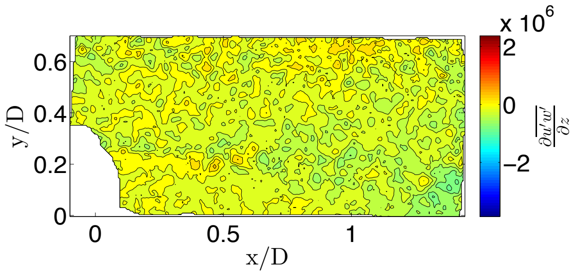

(c) $\frac{\partial \overline{u'w'}}{\partial z}$

Figure C.1: The Reynolds stresses which contribute to the streamwise pressure gradient, $\partial\overline{p}/\partial x$

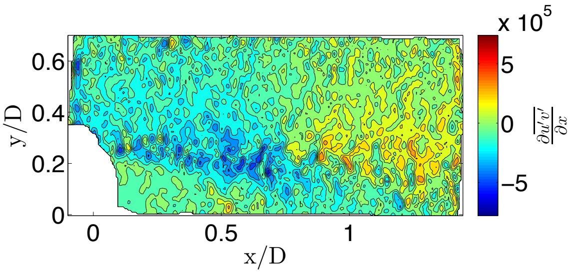

(a) $\frac{\partial \overline{u'v'}}{\partial x}$

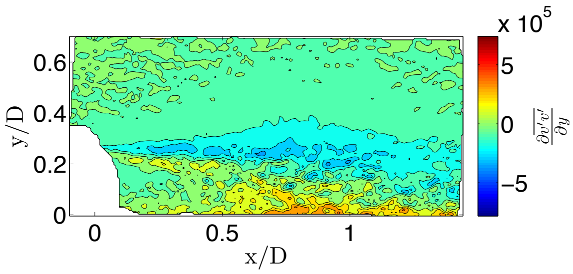

(b) $\frac{\partial \overline{v'v'}}{\partial y}$

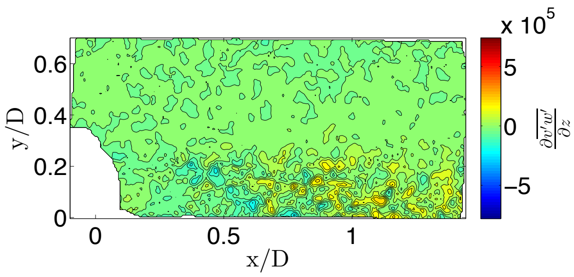

(c) $\frac{\partial \overline{v'w'}}{\partial z}$

Figure C.2: The Reynolds stresses which contribute to the radial pressure gradient, $\partial \overline{p}/\partial y$

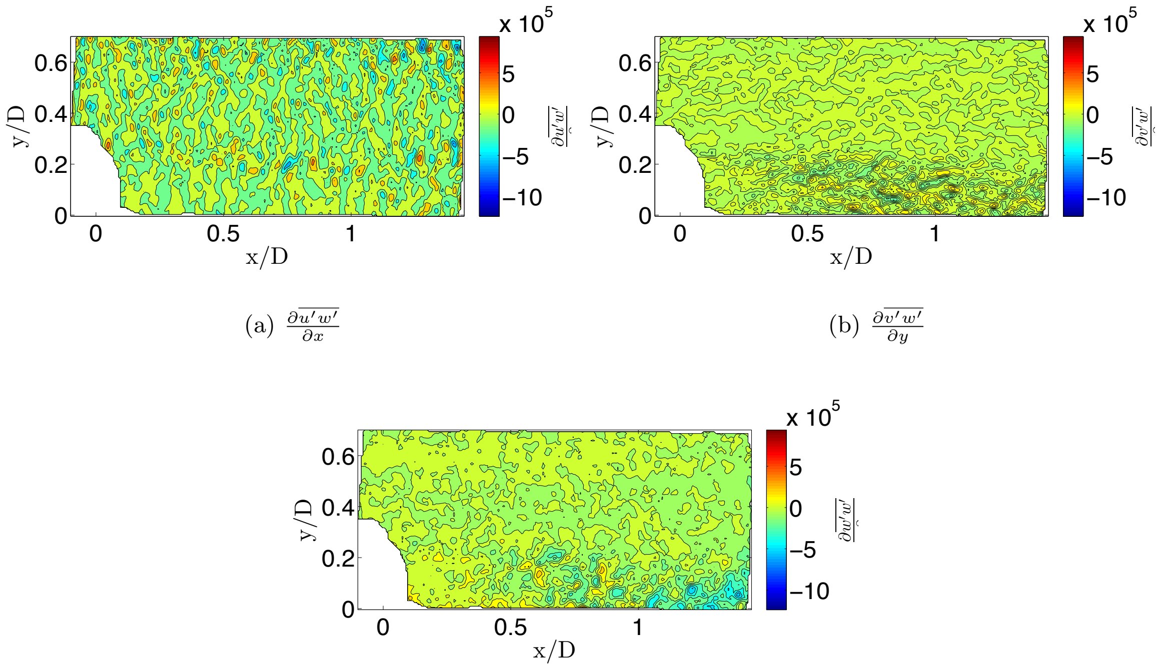

(a) $\frac{\partial \overline{u'w'}}{\partial x}$

(b) $\frac{\partial \overline{v'w'}}{\partial y}$

(c) $\frac{\partial \overline{w'w'}}{\partial z}$

Figure C.3: The Reynolds stresses which contribute to the out-of-plane pressure gradient, $\partial \overline{p}/\partial z$